Exploiting *RAD54B*-deficiency in Colorectal Cancer Cells Through Synthetic Lethal Targeting of *PARP1*

by

Erin N. McAndrew

A Thesis submitted to the Faculty of Graduate Studies of
The University of Manitoba
in partial fulfillment of the requirements of the degree of

MASTER OF SCIENCE

Department of Biochemistry and Medical Genetics
University of Manitoba
Winnipeg

TABLE OF CONTENTS

ABSTRACT

Colorectal cancer (CRC) is the second leading cause of cancer-related deaths in Canada each year. Currently, most therapeutic approaches target rapidly dividing cancer cells by inhibition of normal cellular processes, however these therapies are not selective for cancer cells and unwanted side effects occur. Accordingly, novel cancer-targeted therapeutic strategies and drug targets are urgently needed to diminish the morbidity and mortality rates associated with CRC. Synthetic lethality is a new therapeutic approach that is designed to better target and kill cancer cells by exploiting a cancer-associated mutation (i.e. *RAD54B*-deficiency) thereby minimizing adverse side effects. We hypothesize that *RAD54B*-deficient CRC cells will be selectively killed via a synthetic lethal (SL) interaction with *PARP1*. We have identified and validated a novel drug target, PARP1, within CRC cells harboring *RAD54B*-deficiencies through a SL paradigm. This study represents the first steps necessary to identify and develop precision medicine based therapeutic strategies to combat CRC.

ACKNOWLEDGEMENTS

I am most grateful to my project advisor and mentor, Dr. Kirk McManus, for his guidance and continuous support during my graduate studies. I am deeply appreciative for the time he has spent helping compile this thesis, and for all the additional guidance he has provided during my degree. The dedication Dr. McManus has provided to my graduate studies career development is inspiring. Someday I aspire to be as good as a mentor to an individual as Dr. McManus was to me.

I acknowledge and thank my committee members Dr. Tiina Kauppinen and Dr. Mark Nachtigal who have provided their time and expertise to help ensure my knowledge and research project was of high caliber.

This project would not have been possible without operational funding from Canadian Institutes of Health Research and CancerCare Manitoba Foundation. Furthermore, I acknowledge Research Manitoba, University of Manitoba Graduate Fellowship and CancerCare Manitoba Studentship for providing additional funding for graduate studies.

I would like to thank Zelda Lichtensztejn for being the best ‘lab mom’ anyone could ask for. Zelda provided me with not only foundational training for many techniques used in this study, but also unwavering support in all aspects of day-to-day life. I would like to specifically thank Brent Guppy, Laura Thompson, Amy Cisyk and Sajesh Babu for teaching me the numerous experimental protocols employed in this thesis. Furthermore, I would like to thank Chloe Lepage for her dedication and contributions to this project. Additionally, I would like to thank all other members of the McManus lab both past and present including Yasamin Asbaghi, Lucile Jeusset, Nicole Wilkinson, Tarik Leylek, Allison Baergen, Megan Neufeld and Signe Penner-Goeke.

I wish to extend a huge thank you to my father and my sister for providing unconditional love and support, in all aspects of my career and life. Thank you to Dean, for his patience, support and love. Finally, this is for my late mother, who was taken too soon by this devastating disease.

LIST OF TABLES

LIST OF FIGURES

LIST OF ABBREVIATIONS

~	Approximately
2D	Two dimensional
μg	Microgram (weight)
μL	Microliter (volume)
μm	Micron (size)
μM	Micromolar (concentration)
°C	Degrees Celsius
aa	Amino acid
ADP	Adenosine diphosphate
ATP	Adenosine triphosphate
BCA	Bicinchoninic acid
BER	Base excision repair
CIMP	CpG island methylator phenotype
CIN	Chromosome instability
cm	Centimeter
CO_2	Carbon dioxide
CPTS	Copper phthalocyanine 3, 4’, 4’’, 4’’’-tetrasulfonic acid tetrasodium salt
CRC	Colorectal Cancer
DAPI	4’,6-Diamidino-2-Phenylindole
DDR	DNA damage response
DMEM	Dulbecco’s modified Eagle’s medium
DMSO	Dimethyl sulfoxide
DSB	Double strand break
EC_{50}	Effective Concentration 50
EDTA	Ethylenediamine Tetraacetic Acid
FAP	Familial adenomatous polyposis coli
FBS	Fetal bovine serum
FEN1	Flap Endonuclease-1
fM	Femtomolar (concentration)
FOLFIRI	5-Fluorouracil, Folinic acid and Oxaliplatin
FOLFOX	5-Fluorouracil, Folinic acid and Irinotecan
FRET	Fluorescence resonance energy transfer
Gy	Gray
h	Hour(s)
hTERT	Human telomerase reverse transcriptase
HRR	Homologous recombination repair
IIF	Indirect immunofluorescence
IR	Ionizing radiation
kb	Kilobase
kDa	Kilodalton
LIG4	DNA Ligase IV
mCFA	Modified colony forming assay
min	Minute(s)
mL	Milliliter (volume)

MSI	Microsatellite instability
n	Number of technical replicates
N	Number of biological replicates
NA	Numerical aperture
NAD^+	Nicotinamide adenine dinucleotide
ng	Nanogram (weight)
NHEJ	Non-homologous end joining
nm	Nanometer
nM	Nanomolar (concentration)
PARG	Poly (ADP-Ribose) Glycohydrolase
PARP1	Poly (ADP-Ribose) Polymerase 1
PARylation	Poly-ADP-Ribosylation
PBS	Phosphate buffered saline
PD	Proliferation Defect
pg.	Page
pM	Picomolar
PVDF	Polyvinylidene difloride
RTCA	Real-time cellular analyses
rpm	Revolutions per minute
SD	Standard deviation
SDS/DTT	Sodium dodecyl sulfate/dithiothreitol
sec	Second(s)
siRNA	Short interfering RNA
SL	Synthetic Lethal
SMI	Small molecule inhibitor
SNP	Single nucleotide polymorphism
SOD1	Superoxide Dismutase 1
SSB	Single strand break
SSBR	Single strand break repair
ssDNA	Single strand DNA
TBST	Tris-buffered saline + Tween 20
V	Volts
v/v	Volume by volume
vs.	Versus
w/v	Weight by volume

CHAPTER 1: INTRODUCTION

1.1 INTRODUCTION

The Canadian Cancer Society estimated that in 2015, ~25,000 Canadians would be newly diagnosed with colorectal cancer (CRC) and ~9,300 individuals would succumb to the disease[1]. CRC affects both males and females, and collectively is the second leading cause of cancer-related deaths in North America[1,2]. Accordingly, novel therapeutic strategies and drug targets are urgently needed to diminish the morbidity and mortality rates associated with CRC. This thesis addresses this need by identifying and validating a novel drug target, Poly (ADP-Ribose) Polymerase 1 (PARP1) that will enhance the specificity and killing of CRC cells harboring a *RAD54B*-deficiency using a synthetic lethal (SL) paradigm. Conceptually, synthetic lethality (detailed in Section 1.3, pg. 18) functions by exploiting a specific aberrant genotype contained within a cancer cell, such as a *RAD54B*-deficiency, to enhance the targeting and killing of cancer cells. *RAD54B* is the principle target in this thesis as it is somatically mutated in at least twelve different cancer types[3] (including CRC) and the loss of its expression underlies increases in chromosome numbers[4]. Collectively, these observations suggest diminished *RAD54B* expression is a pathogenic event driving oncogenesis and therefore is an excellent candidate to exploit using a SL approach. Accordingly, the two major objectives of this thesis were to; 1) identify and validate a novel candidate drug target, namely PARP1, to preferentially exploit and target CRC cells harboring a *RAD54B*-deficiency, and 2) to evaluate the efficacy of two PARP1 small molecule inhibitors (SMIs), BMN673 and Olaparib, as lead compounds capable of selectively killing CRC with a *RAD54B*-deficiency. Accordingly, this thesis is designed to identify and develop precision medicine drug targets and strategies to combat CRC.

1.1.1 Colorectal Cancer Staging and Prognosis

CRC is a disease with five distinct stages (stages 0, I, II, III, IV) that describe the degree of local invasion, the amount of lymph node involvement and whether the cancer has metastasized[5]. In stage 0 CRC (i.e. carcinoma *in situ*), the cancer is restricted to the innermost lining of the colon or rectum, while stage I CRC has transcended into the inner wall of the colon or rectum (submucosa). Stage II CRC has extended further into or through the inner wall, and may involve proximal tissues (e.g. serosa), but there is no lymph node involvement[6]. Stage III CRC typically involves proximal lymph nodes, while stage IV CRCs have begun to metastasize to distal sites, such as the liver and lungs[6]. The 5-year survival rates for CRC patients ranges from ~90% for stage I to only ~13% for stage IV disease[5]. Unfortunately, greater than 50% of CRC diagnoses are late stages (III and IV)[7], which is typically considered incurable due to distant metastases[5].

1.1.2 Current Treatment Options for Colorectal Cancer

In general, treatment options depend on the stage at which the CRC was diagnosed. For early stage CRCs (i.e. stages 0-II), surgery is the preferred treatment option and often requires that the cancerous lesion(s) along with a large margin (~15cm) of normal tissue be excised from the patient[5]. For late stage CRCs (i.e. stages III and IV) when surgery is no longer an option due to metastasis, chemotherapy and/or radiation are the preferred treatment options.

The current standard of care for late stage CRC typically involves one of two combinatorial regimens, either FOLFOX (5-Fluorouracil, Folinic acid and Oxaliplatin) or FOLFIRI (5-Fluorouracil, Folinic acid and Irinotecan)[8]. Briefly, 5-Fluorouracil is a pyrimidine analog and a thymidylate synthase inhibitor that prevents accurate DNA replication[9], while Folinic acid is included to enhance the toxicity of 5-Fluorouracil[10]. Oxaliplatin is a platinumbased compound that forms DNA cross-links inducing both DNA single strand breaks (SSBs) and double strand breaks (DSBs)[11], and Irinotecan is a topoisomerase inhibitor that induces DNA damage and interferes with transcription[12].

Unfortunately, the therapeutic activities associated with each of these agents is not restricted to the cancer cells and normal cells often receive collateral damage that manifests in a myriad of side effects including nausea, hair loss, and diarrhea. Nevertheless, these agents predominantly affect cancer cells due to their more rapid proliferation rates and heavy reliance on DNA replication relative to normal cells. Consequently, a major goal of many research groups is to develop novel therapeutic strategies and drug targets that better restrict the therapeutic effect(s) to cancer cells, while minimizing side effects within the normal surrounding cells and tissues.

1.1.3 Molecular Pathogenesis of Colorectal Cancer

Identifying and characterizing the molecular pathogenesis of CRC is an important first step in the development of novel precision medicine based strategies. Hereditary forms of CRC account for only ~15% of all cases, and include hereditary non-polyposis colon cancer (Lynch syndrome) and familial adenomatous polyposis coli (FAP)[13]. In contrast, ~85% of CRCs arise *de novo* without any known inherited genetic predisposition, and are commonly referred to as sporadic CRCs[14]. Sporadic CRCs arise due to the accumulation of mutations within many genes including those that encode functions normally required for genome stability (i.e. within DNA repair genes), and whose loss of expression/function induces genome instability[15]. Genome instability accelerates the acquisition of subsequent DNA mutations and/or copy number changes and is a hallmark of virtually all cancer types, including CRC[6,16]. Consequently, genome instability accelerates alterations in additional oncogenes and/or tumour suppressor genes that result in hypermorphic and/or hypomorphic function of key molecular processes that ultimately impacts the development and progression of cancer.

Genome instability typically arises through one of three different pathways (Figure 1.1) that includes; 1) microsatellite instability (MSI), which is defined as an increase of the basal mutation rate and arises due to defects in members of the DNA mismatch repair pathway (e.g. *MLH1*, *MSH2*, *PMS*, *MSH6*)[17–22], 2) CpG island methylator phenotype (CIMP), which results in gene silencing through promoter DNA hypermethylation (e.g. tumour suppressor genes or DNA repair genes)[23–26], and 3) chromosomal instability (CIN), which is defined as an increase in the rate at which whole chromosomes or large chromosomal fragments are gained or lost[13,27–30].

CIN is of particular interest as it is observed in virtually all cancer types, including both solid (e.g. breast[31]) and liquid/blood (e.g. lymphoma[32]). CIN is arguably best studied in CRC where it occurs in up to 85% of all sporadic cases[33]. Conceptually, CIN promotes cancer heterogeneity by altering chromosome numbers (numerical CIN) and/or inducing structural rearrangements (structural CIN)[34]. CIN is associated with aggressive cancers, the acquisition of multi-drug resistance and consequently poor patient prognosis[35,36]. Despite all of these associations, the molecular origins of CIN are only poorly understood. Thus, identifying the mutated genes (i.e. CIN genes) and aberrant pathways that contribute to oncogenesis is critical to shed new insight into the cancer pathogenesis. Once these CIN genes have been identified, it may be possible to develop therapeutic approaches that specifically exploit defects in those genes to better target cancer cells and limit the occurrence of side effects in normal cells. In this regard, the loss of *RAD54B* expression induces CIN[4] (see Section 1.2.6, pg. 13), rendering it an excellent candidate to exploit via a SL approach (detailed in Section 1.3.2, pg. 19).

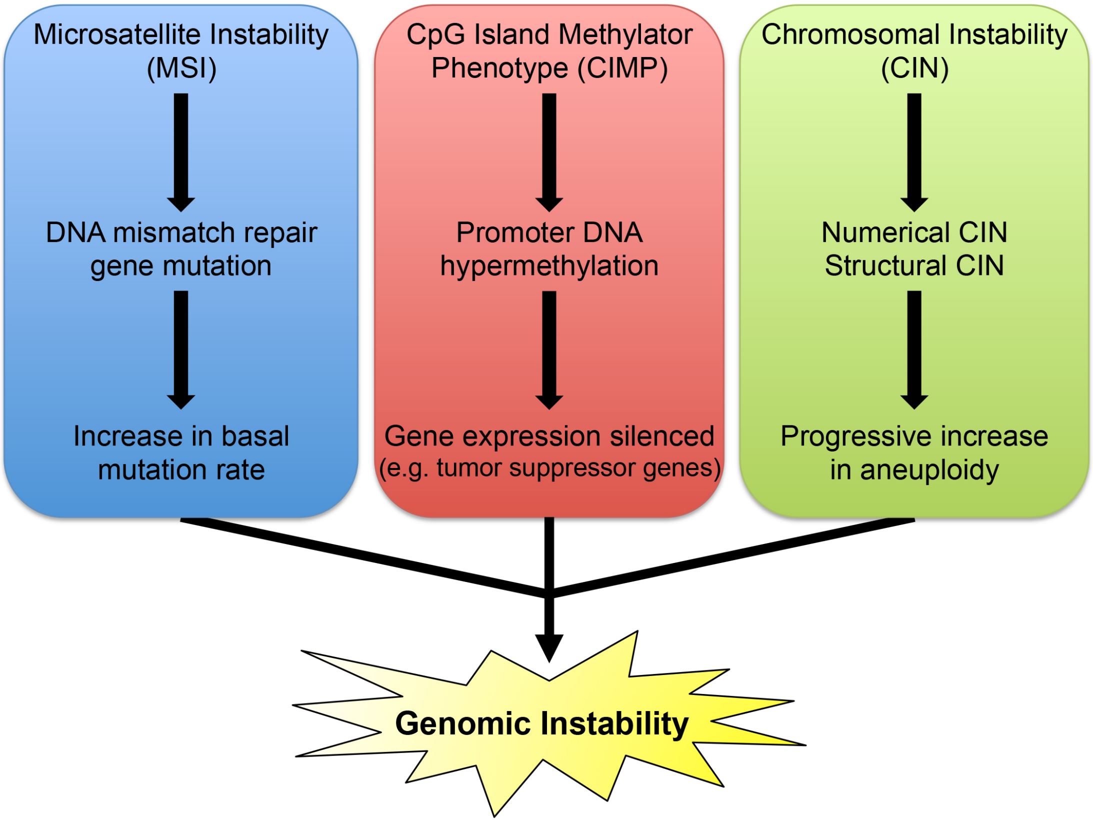

Figure 1.1: The Molecular Pathways Driving Genomic Instability
A schematic representation of the three molecular pathways contributing to genome instability in cancer. Microsatellite instability (MSI) leads to an increase of the basal mutation rate due to defects in the DNA mismatch repair pathway. The CpG island methylator phenotype (CIMP) underlies gene silencing by enhancing promoter DNA hypermethylation (e.g. tumour suppressor genes). Chromosome instability (CIN) is defined as an increase in the rate at which whole chromosomes or large chromosomal fragments are gained or lost. It should be noted that the three pathways are not mutually exclusive as the CIMP pathway can be envisioned to silence genes involved in either the MSI or CIN pathways.

1.2 *RAD54B* IS A HOMOLOGOUS RECOMBINATION REPAIR GENE ENCODING TUMOUR SUPPRESSOR-LIKE PROPERTIES

1.2.1 The Evolutionarily Conserved Nature of Human *RAD54B*

Human *RAD54B* is the evolutionarily conserved ortholog of *Saccharomyces cerevisiae Rad54* (Sc*Rad54*) and was originally identified based on cDNA sequence similarity with Sc*Rad54*. Orthologs have since been identified in wide range of eukaryotes including *Caenorhabditis elegans, Xenopus laevis*, and *Mus musculus* (Table 1.1). Interestingly, *S. cerevisiae* has two proteins with sequence and functional similarity to human RAD54B*,* namely ScRad54 and ScRdh54 (Tid1)[37]. Both ScRad54 and ScRdh54 are involved in sister chromatid recombination[38–40], which is partially conserved by RAD54B within the homologous recombination repair (HRR) pathway in humans (see Section 1.2.4, pg. 11).

1.2.2 Human *RAD54B* Encodes a Multi-domain Protein

Human *RAD54B* maps to 8q22.1 and contains 15 exons that span ~103 kb of genomic DNA[41]. *RAD54B* codes for a 3.074 kb mRNA (2.732 kb of which is coding) that when translated, yields a 910 amino acid (aa) protein with a mass of ~103 kDa[42]. RAD54B is a member of the SWI2/SNF2 helicase superfamily and is comprised of three major protein domains (Figure 1.2); 1) an N-terminal SWI2/SNF2 family domain (aa 299-598), which is a component of the ATPase domain that uses energy derived from ATP hydrolysis to disrupt protein-DNA interactions[43], 2) a DEAD-like helicase (DEXDc) domain (aa 321-462) that is involved in ATP-dependent DNA remodeling[42], and 3) a C-terminal helicase superfamily domain (HELICc) domain (aa 636-766) that utilizes energy from nucleotide triphosphate hydrolysis to fuel translocation along DNA[42]. Additionally, there are five ATP binding sites (aa 329-333, 728, 749, 753, 756) and three nucleotide binding sites (aa 668-671, 691-692, 720-722)

Table 1.1: RAD54B is an Evolutionarily Conserved Homologous Recombination Repair Protein

Protein	**Accession Number**	**Species**	**Protein Size**[A]	**% Identity**[B]	**% Similarity**[C]	**E-value**[D]
RAD54	AJR80403.1	*Saccharomyces cerevisiae*	898	42%	54%	4e-146
RDH54 (TID1)	AJP82439.1	*Saccharomyces cerevisiae*	924	37%	52%	1e-145
Y116A8C.13	NP_001255913.1	*Caenorhabditis elegans*	833	36%	53%	1e-122
RAD54B	XP_688979.4	*Danio rerio*	917	53%	68%	0.0
RAD54B	NP_001085120.1	*Xenopus laevis*	895	65%	77%	0.0
RAD54B	XP_008106606.1	*Anolis carolinensis*	932	64%	76%	0.0
RAD54B	NP_990041.1	*Gallus gallus*	918	69%	79%	0.0
RAD54B	NP_001034645.1	*Mus musculus*	886	78%	87%	0.0

[A] Overall amino acid length

[B] % Identity refers to the extent to which the amino acid sequence is identical relative to human RAD54B.

[C] % Similarity refers to the extent to which the amino acid sequence is similar to human RAD54B (i.e. contains an amino acid with similar biophysical properties).

[D] E-value as determined by BLASTp

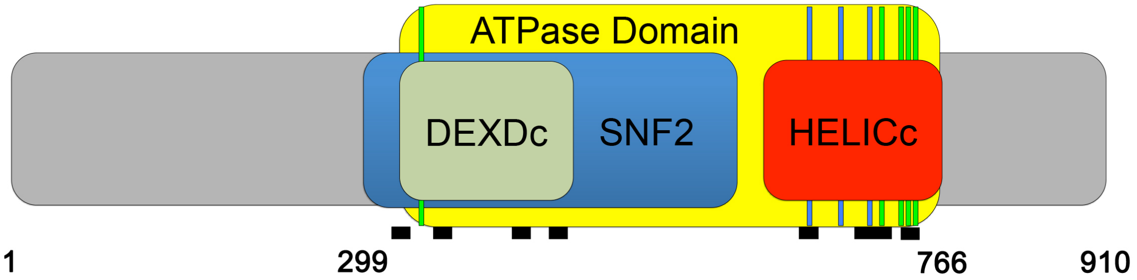

Figure 1.2: Domain and Structural Motifs of Human RAD54B
Schematic depiction of the RAD54B protein domains including a DEXDc domain (green box), a SNF2 domain (blue box) and a HELICc domain (red box). The ATPase domain (yellow box) encompasses the N-terminal DEXDc and C-terminal HELICc subdomains. The green and blue bars represent five distinct ATP binding sites and three nucleotide binding sites, respectively. The black blocks below the protein identify the positions of the seven consensus sequences characteristic of the SWI2/SNF2 protein superfamily. Numbers below the protein (1, 299, 766 and 910) identify aa positions and are included for reference purposes.

that are important for hydrolysis reactions allowing for energy derivation.

RAD54B is a member of the SWI2/SNF2 superfamily of helicases, however unlike classical helicases, the SWI2/SNF2 superfamily does not separate strands of duplex DNA. Rather, they are motor proteins that use energy from ATP hydrolysis to remodel protein-duplex DNA complexes to enhance access to chromatin[44,45]. In fact, the RAD54B-dependent chromatin remodeling activity is important in HRR (see Section 1.2.3), as the repair machinery requires access to the chromatin template to ensure accurate DNA DSB repair.

1.2.3 A Brief Overview of Homologous Recombination Repair

Arguably, one of the most detrimental lesions compromising genome integrity is DSBs, because the DNA strands must be held in close proximity to facilitate DNA repair and prevent translocations from occurring[46]. HRR is commonly referred to as the “error-free” repair pathway as it preserves genome integrity by facilitating the accurate repair of DSBs through the use of the complementary sister chromatid template to precisely copy and repair the break. Thus, HRR is generally restricted to late S- and G2-phases of the cell cycle when a sister chromatid template is available.

Decades of genetic and biochemical studies have identified many of the key proteins, processes and pathways required to effectively repair DSBs via HRR (reviewed in [47]). Collectively, these studies have defined a well-orchestrated series of events that recognize and repair the DSB (Figure 1.3). Briefly, HRR is initiated by the MRN complex (MRE11, RAD50, NBS1), which identifies the DSB. The MRN complex harbors DNA endonuclease activity and resects the 5’ strands of the break to generate 3’ single strand DNA (ssDNA) overhangs that are stabilized through binding of RPA, a ssDNA binding protein. RPA stabilizes the ssDNA by preventing the DNA from re-annealing or forming secondary structures. RPA is subsequently

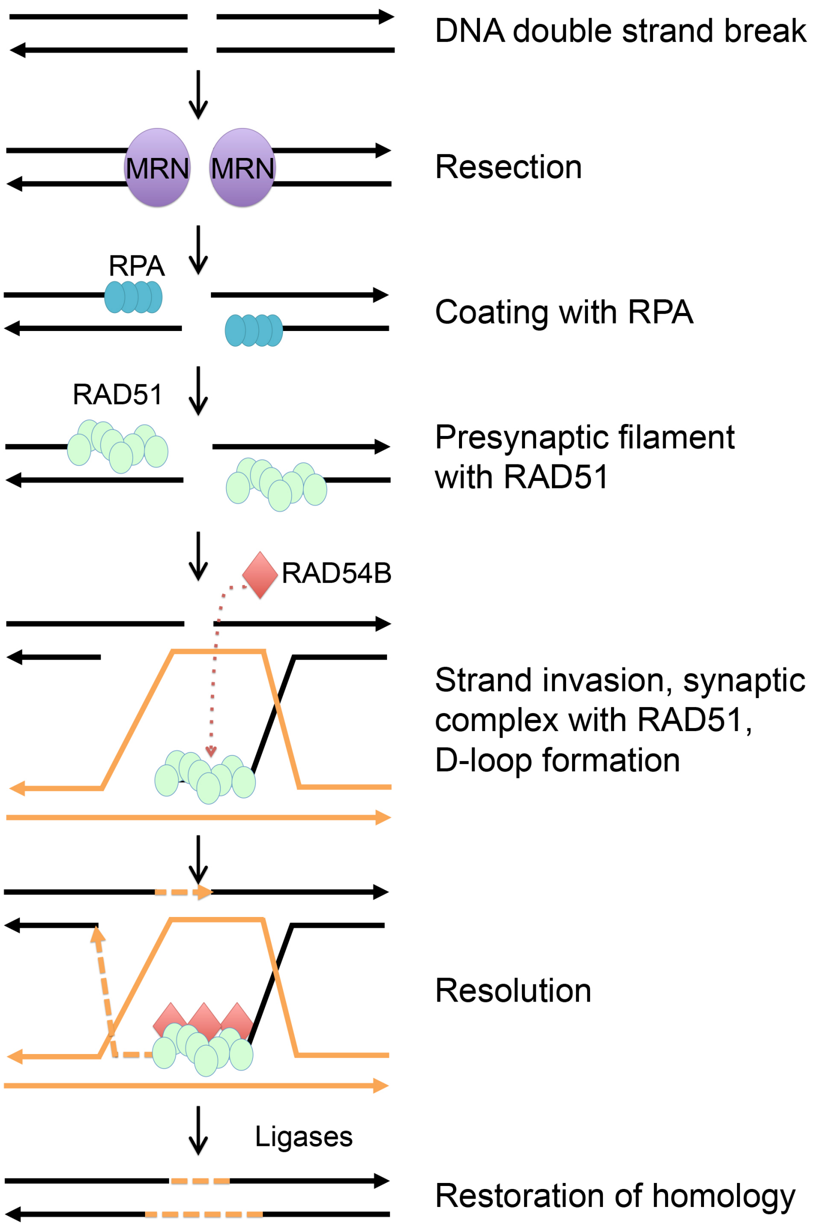

Figure 1.3: Repair of DNA Double-Strand Breaks by Homologous Recombination Repair Generalized schematic of various steps involved in HRR. Following a DSB the MRN complex recognizes the DSB and resects the ssDNA overhang that is subsequently stabilized by RPA. RPA is exchanged for RAD51 and the presynaptic filament is formed. The presynaptic filament initiates strand pairing and exchange with the homologous region of the double-stranded DNA to be copied. RAD54B is a secondary/accessory factor with RAD51 to help mediate strand invasion to form the synaptic complex. The D-loop is formed with the 3' overhang and the homologous sister chromatid, allowing for resolution of the synaptic complex. Finally, DNA polymerase extends the invading end, while DNA ligase I seals the newly synthesized DNA strand, to complete the HRR process.

exchanged with RAD51, which is required for homology recognition and strand exchange[45,48]. In brief, the nucleoprotein complex (comprised of the ssDNA tail along with RAD51) forms the presynaptic filament that initiates homologous pairing and strand exchange with the intact homologous region of the double-stranded DNA to be copied. RAD51 along with secondary/accessory factors, including RAD54B (see Section 1.2.4) mediate strand invasion of the 3' overhang into the undamaged sister chromatid allowing for a sequence homology search that ultimately forms the synaptic complex. Once sequence homology is identified, the displacement loop (D-loop) is formed with the 3' overhang and the homologous sister chromatid. Next, DNA polymerase resolves the synaptic complex by extending the invading end using the sister chromatid as a template. Finally, DNA ligase I seals the DNA strands, effectively eliminating the DSB and restoring the original DNA sequence.

1.2.4 RAD54B is an Accessory Factor in Homologous Recombination Repair of DNA Double-Strand Breaks

Initial insight into a potential role for RAD54B within HRR came from the observation that *RAD54B*-deficiencies led to a severe reduction in the number of targeted chromosomal integration events[49], suggesting RAD54B has a role in homologous recombination. Numerous studies implicate RAD54B in HRR[49,41,37,50], however its specific role in HRR still remains elusive. RAD54B is proposed to be an accessory factor for RAD51, and assist with strand invasion into the undamaged sister chromatid (Figure 1.3, pg. 10)[51]. Thus, a primary focus of early studies was to elucidate the nature of the RAD54B and RAD51 interaction. Several studies have employed indirect immunofluorescence (IIF) to investigate the *in situ* interaction between RAD54B and RAD51, and show that RAD54B co-localizes with RAD51 in interphase nuclei within various cell types[52,53]. In addition, fluorescence resonance energy transfer (FRET) microscopy suggests RAD54B and RAD51 exist in a complex following treatment with mitomycin C, a compound that induces DNA crosslinks that are frequently repaired by HRR[53]. The RAD51/RAD54B interaction is further substantiated by *in vitro* pull-down assays showing they interact within mouse embryonic stem cells[51]. Collectively, the association between RAD54B and RAD51 support RAD54B as a secondary/accessory protein involved in HRR.

1.2.5 *RAD54B* and its Paralog *RAD54L* Exhibit Both Overlapping and Distinct Functions

RAD54B is a human paralog of *RAD54L* exhibiting 48% identity and 63% similarity at the protein level, with a poorly conserved N-terminal domain (Table 1.1, pg. 7). Although paralogs suggest a common ancestral evolutionary origin, numerous biochemical and genetic studies have identified both functional similarities and differences between RAD54B and RAD54L. For example, mouse studies show partially redundant roles for RAD54B and RAD54L in response to genotoxic stress. In 2006, Wesoly and colleagues[51] demonstrated that *RAD54B*-deficient mouse embryonic stem cells were 1.5-fold more sensitive to ionizing radiation (IR) than controls, while corresponding *RAD54L*-deficient cells were 3.0-fold more sensitive. Interestingly, dual *RAD54B*-/*RAD54L*-deficient cells exhibited a similar level of sensitivity to IR compared to the *RAD54L*-deficient cells, suggesting *RAD54B* and *RAD54L* are epistatic, or function within the same biological pathway. Furthermore, adult mice in which *RAD54B* or *RAD54L* were knocked out were hypersensitive to mitomycin C (induces DSB repaired by HRR), as only ~60% of mice survived treatment. Interestingly, the simultaneous knockout of *RAD54B* and *RAD54L* produced fertile mice, however no adult mice survived mitomycin C treatment suggesting partial redundancy and compensatory functions between RAD54B and RAD54L[51].

Although RAD54B and RAD54L exhibit partial overlapping functionality, unique functions have also been identified for each. First, *RAD54B* and *RAD54L* have similar mRNA expression profiles in many human tissues[54,55], indicating the expression of each is important and likely to be non-overlapping. In this regard, biochemical studies have shown that the ATP hydrolysis rate is lower with RAD54B than RAD54L[37], suggesting RAD54B may have less activity in remodeling protein-duplex DNA complexes. Furthermore, pull-down assays have shown that RAD54B interacts with RAD51 independent of DNA damage, while RAD54L only appears to interact with RAD51 following DSB induction[52]. Although currently unclear, some of the functional differences observed between RAD54B and RAD54L may be attributed to the divergent protein sequences that occur predominantly within the N-terminal domains.

1.2.6 *RAD54B* is a Chromosome Instability Gene

RAD54B is a *bona fide* human CIN gene, as loss of expression induces CIN[4], which suggests it may be a pathogenic event contributing to the development and progression of cancer[34] (Section 1.1.3, pg. 3). *RAD54B* was initially identified as a candidate human CIN gene through a cross-species candidate gene approach as both Sc*Rad54* and Sc*Rdh54* are yeast CIN genes[56]. In human cells, *RAD54B* silencing or genomic knockout induced an increase in DNA content that correlated with an increase in chromosome numbers[4]. Furthermore, when RAD54B was reintroduced back into *RAD54B*-deficient cells, CIN (aneuploidy) was reduced and thus *RAD54B* was confirmed as a novel human CIN gene[4]. These important findings suggest that RAD54B harbors tumour suppressor-like characteristics and *RAD54B* expression must be adequately regulated as loss in expression or function causes CIN, a known driver in oncogenesis[34]. Importantly, because mutations and/or deletions of *RAD54B* genetically distinguish cancer cells from normal cells we believe these defects can be therapeutically exploited through a SL approach (Section 1.3.2, pg. 19).

1.2.7 Aberrant *RAD54B* Expression is Associated with Cancer

In 1999, Hiramoto and colleagues[41] identified somatic *RAD54B* mutations in both primary lymphoma and colon cancer. Since this original description, DNA re-sequencing efforts[57–72] have identified a large number of somatic *RAD54B* alterations including gene amplification, homozygous deletions, and non-synonymous SNPs in at least twelve different human cancers, including colorectal, breast, and lung (Figure 1.4). Furthermore, *RAD54B* is both amplified and deleted in various cancer types (e.g. liver, prostate, sarcoma) supporting the possibility that altered expression may be pathogenic events that contribute to oncogenesis. Beyond somatic alterations, gene expression analyses from Oncomine database[73] reveal decreases in mRNA transcripts within certain cancer types (e.g. breast, pancreatic, brain) relative to normal control tissues, further supporting *RAD54B* as a tumor suppressor-like gene.

As detailed above, studies in cancer cell lines show that loss of *RAD54B* expression results in CIN[4]. While the functional impact homozygous deletions have on cancer formation are being evaluated, the functional implications specific cancer-associated missense mutations have yet to be evaluated, but can be predicted through *in silico* approaches including Mutation Assessor[74], PolyPhen2[75] and SIFT[76]. In general, these online resources predict whether certain aa substitutions are most likely benign/tolerated or damaging/not tolerated. These *in silico* algorithms typically evaluate the impact of specific aa substitutions based on the evolutionary conserved nature of the residue involved, or the position of the substitution within the three-dimensional structure of the protein itself, or a closely related protein. As shown in Figure 1.5 (and detailed in Table S1, pg. 111) some aa substitutions identified in cancer are predicted to be "probably damaging" or "not tolerated" suggesting they may adversely impact RAD54B function. It is noteworthy that many of the aa substitutions identified as potentially damaging localize within the SNF2, DEXDc, HELICc or ATPase domains of RAD54B (Figure 1.5), highlighting the important nature of these domains. However, since the three-dimensional structure of RAD54B has yet to be solved, the importance of many key structural residues may not be adequately assessed. Based on the abundance of mutations predicted to encode aa substitutions impacting function, *RAD54B* can be classified as a putative tumor suppressor gene under the 20:20 rule[77], which stipulates that at least 20% of the mutations identified in a gene must be predicted to be inactivating[78].

Beyond the single aa substitutions discussed above, several nonsense mutations in *RAD54B* have also been identified in human cancers[58,62,65–67,69,72]. Nonsense mutations are predicted to more readily induce loss-of-function relative to single aa substitutions as they induce either the complete loss or premature truncation of RAD54B. The functional implications for a given nonsense mutation will depend on the position of the premature stop codon within the encoded mRNA. For example, if the nonsense mutation localizes within the 5' portion of the mRNA transcript, then the nonsense mediated decay surveillance pathway will degrade the mRNA and prevent protein translation[79]. Alternatively, if the nonsense mutation localizes to the 3' portion of the transcript, a partial protein may be translated lacking critical C-terminal domains (e.g. ATPase, SNF2, etc.) and may function in a dominant-negative manner[79]. A dominant-negative phenotype may adversely affect RAD54B binding partners, such as RAD51, and is predicted to induce CIN. Collectively, the above data indicate that *RAD54B* is somatically altered in a wide range of cancer types, and suggest that loss of expression and function may be a pathogenic event contributing to cancer formation.

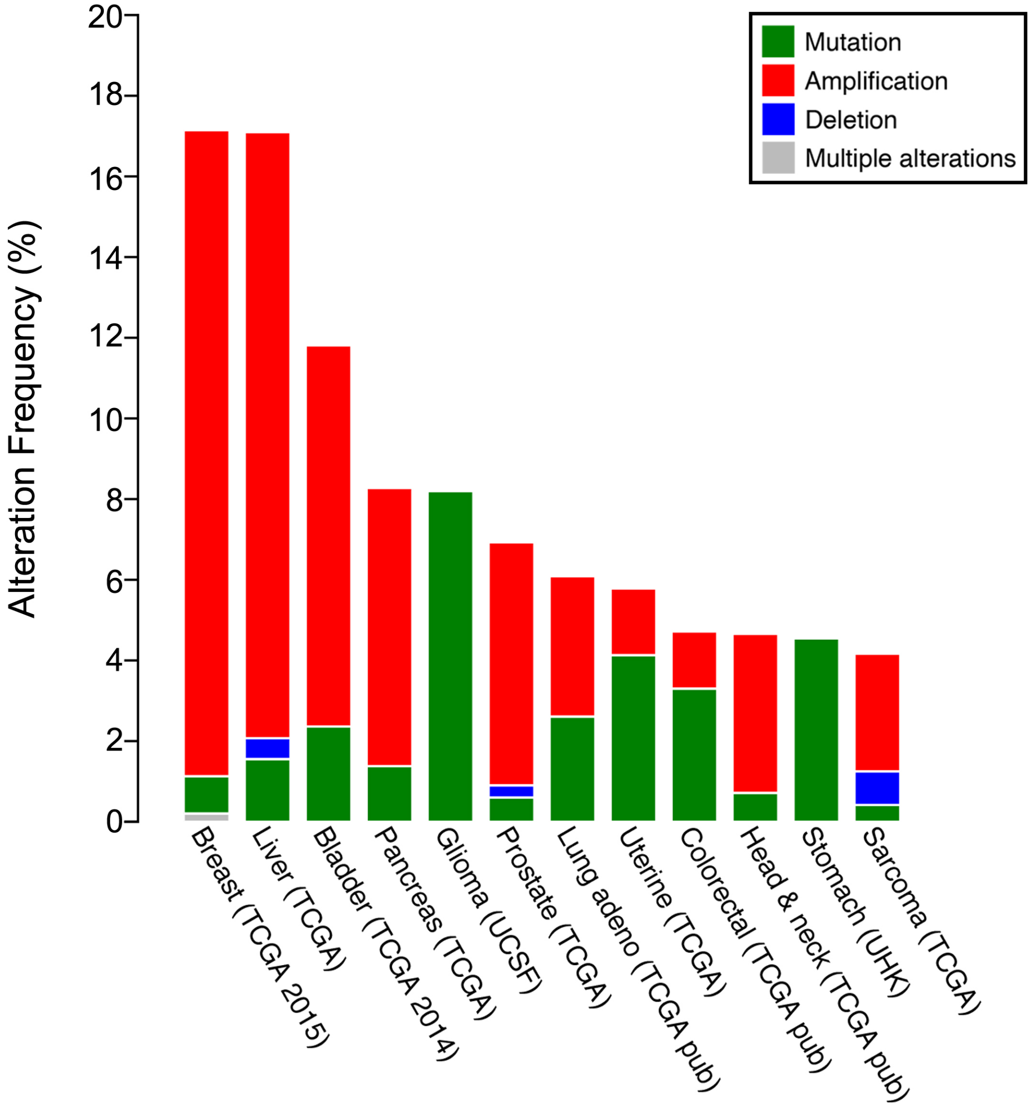

Figure 1.4: Frequency and Types of *RAD54B* Alterations in Human Cancers
Histogram displaying the frequency of *RAD54B* alterations (i.e. mutation, deletion, or amplification) for each of the cancer type displayed on the x-axis. Data and graph obtained from the cBioPortal for Cancer Genomics database[3].

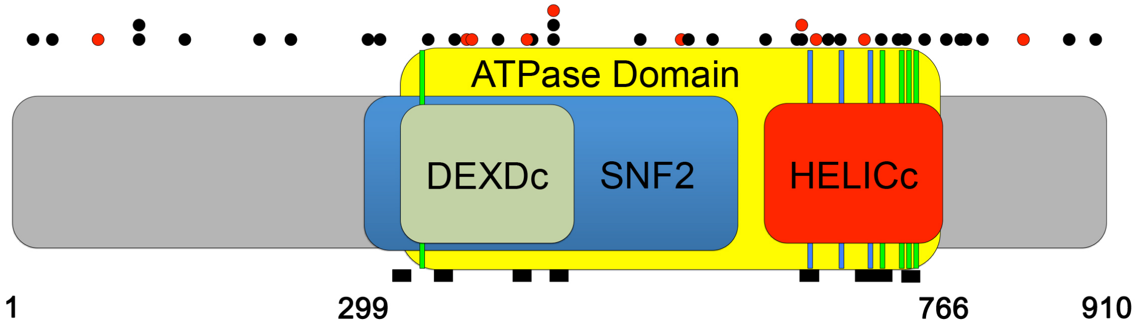

Figure 1.5: Position of Cancer-Encoded Amino Acid Substitutions in RAD54B
A schematic presenting the location of aa substitutions found in human cancer that are predicted by PolyPhen2, Mutation Assessor or SIFT to be "potentially damaging" or "not tolerated". Black circles above the protein identify encoded positions of missense mutations, while red circles identify positions of nonsense mutations (see Table S1, pg. 111 for further details). Numbers below the protein (1, 299, 766 and 910) identify aa positions and are included for reference purposes.

1.3 SYNTHETIC GENETIC TARGETING AS AN EMERGING ANTI-CANCER THERAPY

Many current chemotherapeutic strategies involve the systemic administration of a drug (e.g. 5-Fluorouracil, Oxaliplatin, and Irinotecan), whose cytotoxic effect is frequently incapable of distinguishing cancerous cells from normal cells and often leads to many unwanted side effects[80]. Accordingly, novel therapeutic strategies are urgently needed to better target and restrict killing to cancer cells to better manage the disease. Synthetic genetic approaches aim to exploit the aberrant genetics (e.g. mutation, deletion or amplification) associated with cancer development, and are predicted to induce highly specific killing in cancer cells while minimizing side effects within normal cells. Synthetic genetic interactions (reviewed in [81,82]) have been studied extensively in model organisms such as budding yeast and are now being explored for their therapeutic potential in various cancer contexts. *RAD54B* is an excellent candidate to exploit through synthetic genetic approaches as alterations in expression and function occur in a wide variety of cancers that by definition, served to genetically distinguishes the cancer cells from normal surrounding cells.

In general, there are two categories of synthetic genetic interactions; 1) synthetic dosage lethal approaches that exploit hypermorphic expression and/or function within oncogenes, and 2) synthetic lethal (SL) approaches that exploit hypomorphic expression and/or function of a tumour suppressor genes. Although synthetic dosage lethality is an important concept, the work presented within this thesis focuses exclusively on SL approaches and thus only synthetic lethality is described below.

1.3.1 Synthetic Lethality

The term synthetic lethality was first coined by Theodore Dobzhansky in 1946, and described the lethal genetic interaction observed when two independently viable homologous chromosomes were allowed to recombine in *Drosophila pseudoobscura*[83]. Since the original description, the definition has been refined and is now used to describe a rare and lethal combination of two independently viable mutations[81,82] (Figure 1.6A). Simply put, synthetic lethality describes a genetic interaction in which the outcome of a specific mutation or deletion is influenced by the presence of a pre-existing genetic alteration, such as those occurring in cancer (Figure 1.6B). In general, SL interactions are envisioned to occur in three distinct ways (Figure 1.7); 1) the partial loss of two independent proteins contained within the same essential biological pathway (i.e. epistasis group), such that the pathway is no longer functional, 2) the loss of two independent proteins contained within two distinct parallel pathways both of which are required for viability, and 3) the loss of two independent proteins within parallel pathways that together impinge on an essential biological pathway or process[81,82].

In 1997, Hartwell *et al*[84] proposed that cancer cells represent sensitized cells that may be vulnerable to drug therapies selectively targeting a second unlinked gene product. More specifically, they suggested that targeting a gene product that is a SL interactor of a gene that is somatically mutated in cancer could induce death within the cancer cells and leave the normal surrounding cells unaffected. Accordingly, a major goal of this thesis was to expand the number of known SL interactors (e.g. drug targets) that could exploit a deficiency in *RAD54B*.

1.3.2 *RAD54B* is a Candidate for Synthetic Lethal Therapeutic Approaches

RAD54B represents an excellent candidate to exploit using a SL approach as it is somatically mutated/deleted in numerous cancer types, including CRC (Figure 1.4, pg. 16) and it

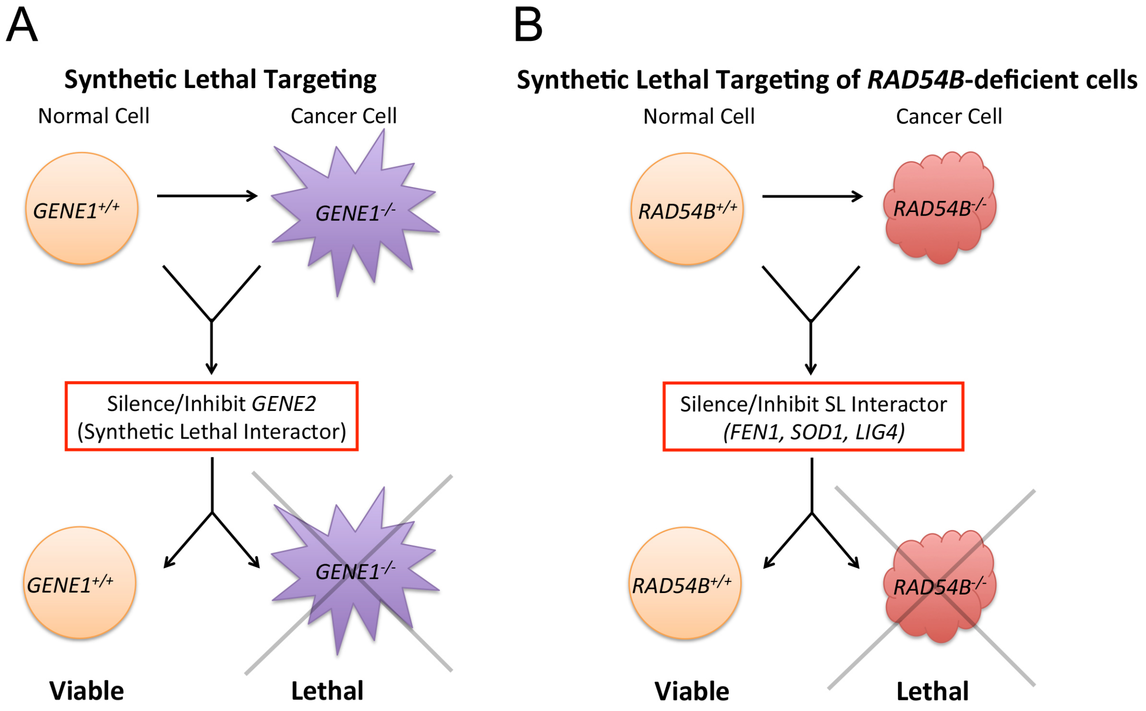

Figure 1.6: Synthetic Lethal Targeting of Cancer Cells
Schematic representations of the SL targeting paradigms to be employed within a human CRC context. ***(A)*** A cancer-associated hypomorphic mutation or deletion in a gene (e.g. *GENE1* a tumor suppressor gene) is selectively killed by silencing or inhibiting a SL interactor (i.e. *GENE2*). ***(B)*** In cancer, a *RAD54B*-deficiency (*RAD54B*$^{-/-}$) is selectively targeted and killed by silencing or inhibiting the activity of a SL interactor (e.g. *FEN1, SOD1, LIG4*).

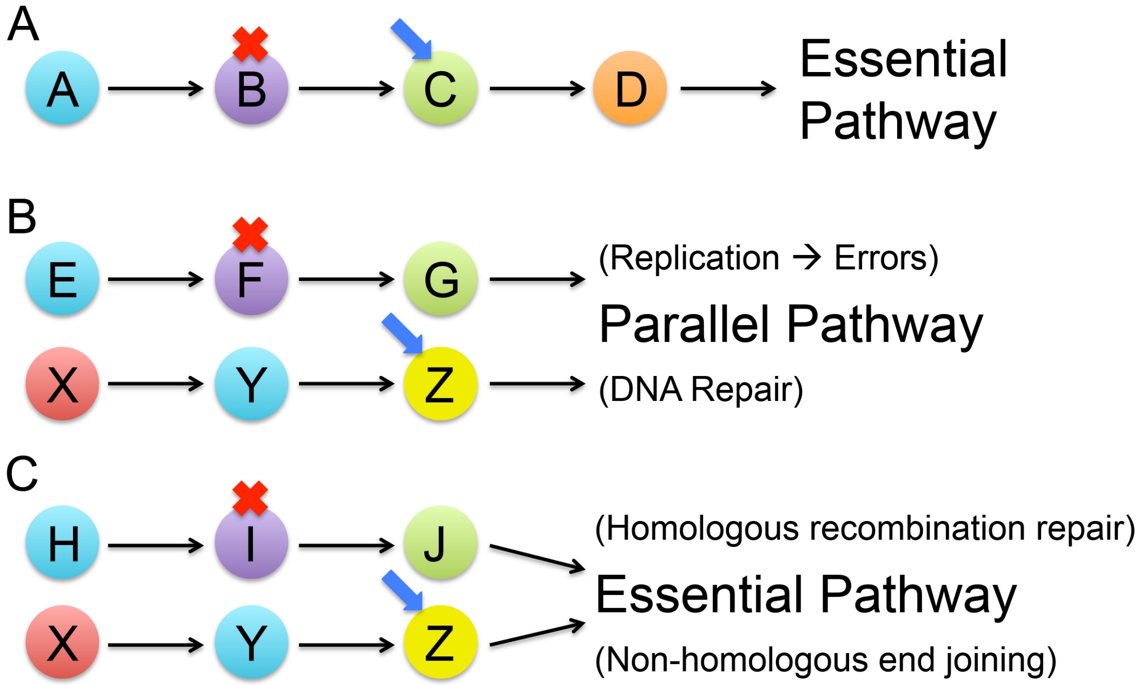

Figure 1.7: Conceptual Models of Pathways Underlying Synthetic Lethal Interactions
Conceptual models depicting the three mechanism(s) underlying SL interactions: circles represent genes, red "X" are cancer-associated mutations/deletions and SL interactors (i.e. drug targets) are identified by blue arrows. ***(A)*** Partial loss of two independent proteins contained within the same essential biological pathway (i.e. epistasis group), such that the pathway is no longer functional. ***(B)*** Loss of two independent proteins contained within two distinct parallel pathways, both of which are required for viability. ***(C)*** Loss of two independent proteins within parallel pathways that together impinge on an essential biological pathway or process.

encodes a protein with tumor suppressor-like properties (see Section 1.2.7, pg. 14). Indeed, several genetic studies have already identified three unique SL interactors for *RAD54B* including; 1) Flap Endonuclease-1 (*FEN1*)[4], 2) Superoxide Dismutase 1 (*SOD1*)[85], and 3) DNA Ligase IV (*LIG4*)[86] (Figure 1.6B, pg. 20).

In 2009, McManus *et al* coupled siRNA-based silencing and high-content imaging to show that diminished FEN1 expression induced cytotoxicity preferentially within *RAD54B*-deficient CRC cells but not within an isogenic control cell line thereby identifying *RAD54B* and *FEN1* as SL interactors[4]. Later, Sajesh *et al* expanded the number of SL interactors to include *SOD1*. They showed that *RAD54B*-deficient CRC cells are hypersensitive to SOD1 silencing and inhibition[85]. Finally, *LIG4* was serendipitously identified as a SL interactor during unsuccessful efforts to generate a dual *RAD54B*-/*LIG4*-deficient cell line[86]. Oh *et al* identified the SL interaction between *RAD54B* and *LIG4* because the dual knockout of these genes resulted in no viable clones.

Overall, the underlying mechanism accounting for all three SL interactions relies on the synergistic killing of *RAD54B*-deficient CRC cells following the silencing or inhibition of a second unlinked gene with relevance to the DNA Damage Response (DDR) (e.g. *FEN1, SOD1, LIG4*). Briefly, FEN1 is a flap endonuclease whose activity is required for DNA synthesis and repair[87], while SOD1 normally limits DNA damage induced by reactive oxygen species (i.e. superoxide radicals) by reducing them to oxygen and water in a two-step reaction[88,89]. LIG4 on the other hand, functions within the “error-prone” non-homologous end joining pathway (NHEJ), which effectively ‘glues’ DSB ends together following processing and results in microdeletions[86]. Based on these observations, we hypothesize that additional members of the DDR, such as *PARP1* (described below) will be SL with *RAD54B*. Accordingly, the major goal of this thesis was to expand the number of SL interactors (drug targets) of *RAD54B* to maximize the number of drug targets pursued in pre-clinical studies.

1.4 PARP1 AND CANCER

1.4.1 PARP1 – A Brief Introduction of the Gene and Protein

In the early 1960s, Pierre Chambon and colleagues were the first to discover poly-adenosine-diphosphate-ribose (ADP-Ribose) synthesis within the nuclei of cells[90,91]. The protein responsible for poly (ADP-Ribose) synthesis was soon identified as Poly (ADP-Ribose) Polymerase 1 (PARP1), and was ultimately purified in 1977[92]. *PARP1* maps to chromosome 1q41.1 and contains 23 exons that span ~47 kb of genomic DNA[42]. *PARP1* codes for a 4.001 kb mRNA (3.044 kb of which is coding sequence) that when translated, yields a protein of 1014 aa residues in humans[93]. PARP1 is an abundant, ~113 kDa nuclear protein and is the founding member of the PARP superfamily[94]. PARP1 consists of three domains; 1) an N-terminal DNA binding domain that contains three zinc fingers, 2) a central auto-modification domain, and 3) a C-terminal catalytic domain responsible for the transfer of ADP-Ribose subunits from nicotinamide adenine dinucleotide (NAD^+) to protein acceptors[95]. The PARP superfamily is comprised of at least 18 members, all of which contain the "PARP signature" motif within the C-terminal catalytic domain of PARP1[94,96,97]. Overall, PARP1 is responsible for ~85-90% of PARP activity within a cell, while the remaining activity is predominated by PARP2[98].

1.4.2 A Brief Summary of PARP1 Function in DNA Repair

PARP1 has traditionally been reported to play a role in the base excision repair (BER)/single strand break repair (SSBR)[99,100] pathway. However, more recent evidence implicates PARP1 in many additional DDR pathways including HRR, NHEJ and nucleotide excision repair (reviewed in [101]; summarized in Table 1.2). In general, PARP1 initiates and

Table 1.2: Summary of PARP1 Involvement in DNA Repair Pathways

DNA Repair Pathway	**PARP1 Function**
BER/SSBR	PARylation recruits BER complex[100,102,103]
HRR	PARylation recruits MRE11[104] PARylation activates ATM signalling[105]
Classical NHEJ	PARylates and activates DNA-PKcs[106]
Alternative NHEJ	In the absence of Ku, PARP1 binds to DNA ends[107]
Nucleotide excision repair	Cooperates with DDB2 to improve function of DDB2 and XPC during lesion recognition[108]

Abbreviations: ATM, Ataxia Telangiectasia Mutated; DNA-PKcs, DNA-dependent protein kinase; Ku, heterodimer of Ku70 and Ku80; DDB2, Damage-specific DNA binding protein 2; XPC, Xeroderma pigmentosum.

modulates the BER/SSBR pathway by acting as a sensor of DNA damage and binding to DNA through its N-terminal zinc finger domains[109]. Once activated, PARP1 catalyzes the cleavage of NAD^+ to generate nicotinamide and ADP-Ribose. This process is repeated and PARP1 assembles a polymer of negatively charged ADP-Ribose moieties to generate long and branched poly (ADP-Ribose) chains (referred to as PARylation) on various acceptor proteins including histones, DNA repair enzymes and PARP1 itself, in a processes referred to as auto-PARylation (Figure 1.8)[110]. Concurrent with PARP1 activation, Poly (ADP-Ribose) Glycohydrolase (PARG) catabolizes poly (ADP-Ribose) moieties back into ADP-Ribose[111]. The DNA damage-dependent PARylation of histones and subsequent recruitment of chromatin remodeling enzymes alters chromatin structure such that it becomes more accessible to DNA repair enzymes to enable DNA repair[101]. Interestingly, auto-PARylated PARP1 has diminished affinity for DNA, thereby rendering the site of DNA damage more accessible to the recruitment of additional DNA repair proteins. In general, PARylation recruits a large number of DNA repair proteins including XRCC1[102], MRE11[104], ATM[105].

Overall, the level of PARP1 activation and the amount of PARylation reflect the level of DNA damage present within a cell. If low to moderate DNA damage is present, PARP1 will stimulate DNA repair and cell survival[112]. However, if extensive DNA damage occurs, prolonged PARP1 activation will lead to NAD^+ and ATP depletion, and ultimately induce cellular cytotoxicity through a Caspase-independent type of death more commonly referred to as parthanatos[112]. Due to the role PARP1 plays as a primary DNA damage sensor, it has been an attractive therapeutic target to sensitize cancer cells to DNA damaging agents and more recently for cancers with HRR defects (detailed below).

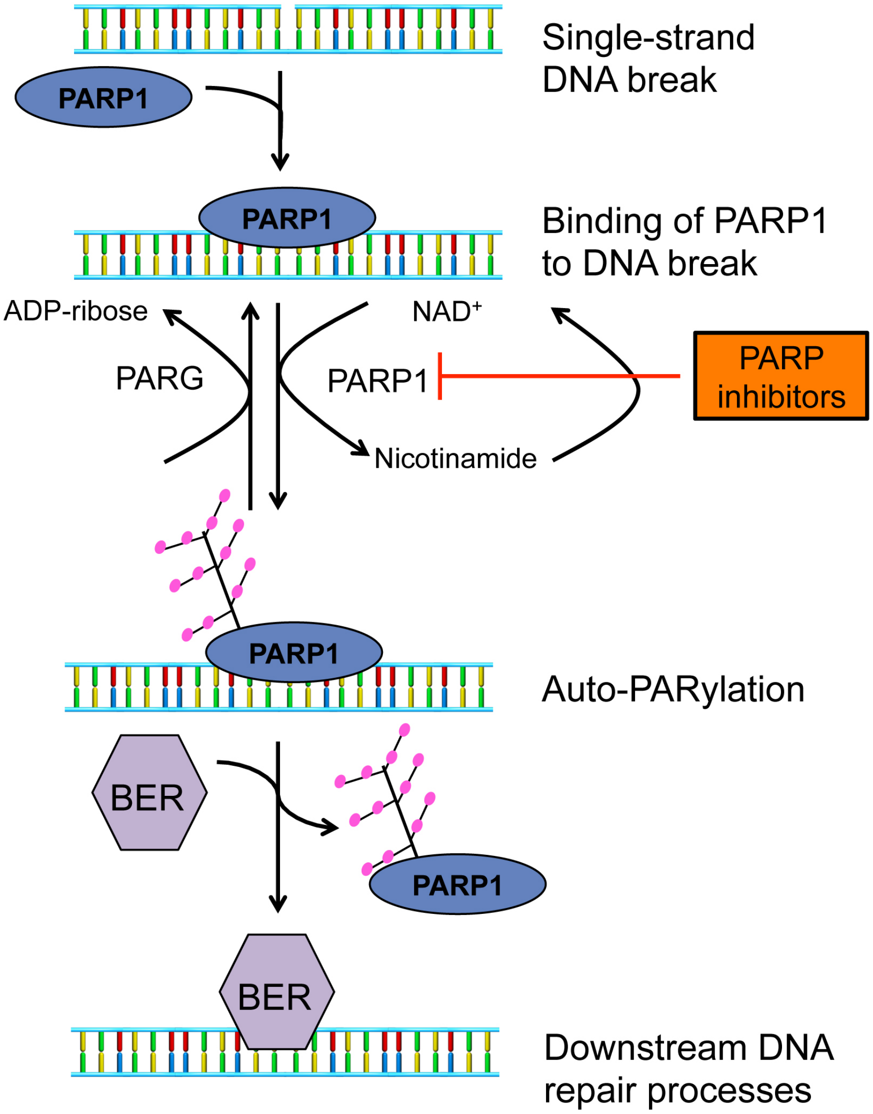

Figure 1.8: PARP1 is a Primary DNA Damage Sensor and Recruits DNA Damage Response Proteins

A general schematic of PARP1 activation in response to DNA damage. PARP1 binds to DNA SSBs and catalyzes the synthesis of poly-ADP-Ribose (pink circles) using NAD^+, onto itself (auto-PARylation) and other acceptor proteins, while PARG catabolizes the poly-ADP-Ribose into ADP-Ribose moieties. Auto-PARylated PARP1 dissociates from the DNA facilitating access for the BER complex to site of damage to facilitate DNA repair. PARP inhibitors prevent the catalytic activity of PARP1 and prevent PARylation, including auto-PARylation.

1.4.3 *PARP1* and *BRCA1/2*: The Prototypic Human Synthetic Lethal Interactors

The *BRCA1/2* and *PARP1* SL interaction is the prototypic and best-studied example of a SL therapeutic approach in human cancer and the first SL approach to be applied within the clinic. In 2005, two seminal studies identified a SL interaction between *BRCA1/BRCA2* and *PARP1*[113,114]. *BRCA1/2* are classical heritable breast cancer susceptibility genes, however somatic mutations or deletions also occur in many sporadic cancers[115]. BRCA1/2 both function in HRR and loss of BRCA1/2 renders HRR dysfunctional, and is associated with genome instability[116,117]. On the other hand, diminished expression or inhibition of PARP1 results in persistent, unrepaired SSBs that as cells enter S-phase and begin to replicate their DNA, induce replication fork collapse and the generation of DSBs[118]. Armed with this knowledge, the two independent research teams hypothesized[113,114] that cells with HRR defects imparted by *BRCA1/2* deficiencies would be sensitive to PARP1 inhibition. As predicted, preferential killing of *BRCA1/2*-deficient cells was observed following PARP1 silencing/inhibition relative to controls, indicating *BRCA1/2* and *PARP1* are SL. The *BRCA1/2* and *PARP1* SL interaction was further validated in pre-clinical mouse models[113,114], and identified PARP1 as a novel candidate drug target in *BRCA1/2*-deficient cancers.

1.4.4 PARP1 Inhibitors and Clinical Trials for *BRCA1/2* Defective Cancers

Although the clinical applicability of SL approaches is still within its infancy, the *BRCA1/2 PARP1* SL interaction is the most clinically advanced example. In fact, the preferential killing observed in *BRCA1/2* cells following PARP1 inhibition[113,114] spawned numerous additional research efforts aimed at identifying novel PARP1 inhibitors including Olaparib[119], Veliparib[120] and BMN673[121]. As a result, many clinical trials have been initiated within various cancer types that focus on evaluating the efficacies of these inhibitors as either single or combinatorial agents (see [122]).

Nearly all PARP1 inhibitors identified to date are designed to catalytically inhibit PARP1 by inserting within the nicotinamide binding pocket of the protein[123]. As a result, this strategy has produced mainly broad-range PARP inhibitors that have effects on many PARP family members[124]. In fact, the two PARP1 inhibitors employed in this thesis, BMN673 and Olaparib, in addition to catalytic inhibition of PARP1, also catalytically inhibit PARP2[124,125]. Furthermore, BMN673 and Olaparib, also trap PARP1/2 onto DNA complexes[126,127]. The PARP1/2-DNA complexes are cytotoxic as they sterically impede the progress and function of the replication machinery and lead to replication fork collapse, and the formation of DSBs[128]. Interestingly, BMN673 is ~100-fold more potent at trapping PARP1/2 onto DNA relative to Olaparib[127]. Thus, many PARP1 inhibitors likely function through both PARP1 inhibition (i.e. prevent SSBR) and the induction of DSBs resulting from replication fork collapse during S-phase.

Although the clinical utility of PARP1 inhibitors is not yet established, early clinical trials are beginning to show promise for PARP1 inhibitors in *BRCA1/2* defective cancers. In 2010 for example, two Phase II clinical trials showed that Olaparib exhibited antitumor responses in familial *BRCA1* or *BRCA2* mutant breast[129] and ovarian[130] cancers with overall responses rates of 41% and 33%, respectively. Furthermore, a Phase II clinical trial also demonstrate that Olaparib as a maintenance treatment, significantly improved progression free survival in patients with platinum-sensitive, high-grade serous ovarian cancer[131]. Based on these exciting findings, the FDA approved Olaparib in December 2014 as a mono-therapy for maintenance treatment in women with *BRCA1/2* mutant, platinum-responsive, high-grade serous ovarian cancer[132].

Collectively, PARP1 inhibition represents the first clinically approved application of a SL targeting approach and serves as a prototypic example of how a novel precision medicine strategy can be identified and translated from a fundamental research perspective. Furthermore, these findings support the identification of further SL interactors of *PARP1* to uncover additional genetic susceptibilities in cancers that can be clinically exploited using a similar precision medicine approach. Accordingly, to expand beyond the *BRCA1/2 PARP1* SL interactions and identify precision medicine therapeutic strategies for other cancer-associated mutations, investigating putative *PARP1* SL interactions with other HRR genes would be valuable. This is particularly plausible as numerous studies have shown that proteins functioning within the same biological pathway (e.g. HRR) often share SL interactors[4,85,133]. Accordingly, since numerous cancer-associated loss-of-function *RAD54B* mutations have been identified in cancer (Section 1.2.7, pg. 14), and RAD54B functions within HRR (similar to BRCA1/2), the fundamental goal of this thesis was to determine whether *RAD54B* and *PARP1* are SL within a CRC context.

CHAPTER 2: RATIONALE, HYPOTHESES AND RESEARCH AIMS

2.1 RATIONALE

Understanding the aberrant genetics of cancer is a critical first step to identify novel anti-cancer therapies with enhanced specificity and fewer side effects. *RAD54B* is a human CIN gene[4] and is somatically mutated in at least 12 different cancer types[58,134–139], including CRC, indicating diminished *RAD54B* expression may contribute to oncogenesis (Section 1.2.7, pg. 14). Thus, identifying a therapeutic strategy and drug target that can specifically exploit *RAD54B* defects found in cancer has the potential to benefit a wide variety of cancer types (Table 2.1, pg. 32).

Synthetic lethality is an emerging anti-cancer therapy that is predicted to enhance the targeting and killing of cancer cells, while at the same time limiting side effects within normal cells[81,82]. Previous studies have shown that proteins functioning within the same biological pathway (e.g. DDR or HRR) often share SL interactors[4,85,133]. Since several genes (*FEN1*[4], *SOD1*[85], *LIG4*[86]) encoding functions within the DDR are SL with *RAD54B*, we reasoned that additional genes encoding functions within the DDR pathway would also be SL with *RAD54B*. Furthermore, since *BRCA1/2* encode functions within the HRR pathway[116,117] and are SL with *PARP1*[113,114], we hypothesized that *RAD54B* which also functions in HRR[37,41,49,50], would be SL with *PARP1*. Thus, to expand the number of known SL interactors (i.e. drug targets) of *RAD54B*, this thesis examined the potential SL interaction predicted to exist between *RAD54B* and *PARP1*.

2.2 HYPOTHESES AND RESEARCH AIMS

We hypothesize that *RAD54B*-deficient CRC cells will be selectively killed via a SL interaction with *PARP1*. We further posit that this SL interaction will occur by down-regulation of PARP1 activity by siRNAs and with SMIs for PARP1, BMN673 and Olaparib. We have two specific experimental aims to evaluate *RAD54B* and *PARP1* as SL interactors in human cells.

Aim 1: To identify and validate *PARP1* as a SL interactor of human *RAD54B* in CRC cells.

Aim 2: To evaluate the efficacy of SMIs for PARP1, BMN673 and Olaparib, as therapeutic agents in CRC cells.

Table 2.1: Frequency of Somatic *RAD54B* Mutations in Four Cancer Types[A]

Cancer Type	Mutation Frequency	Canadian New Cases[B]	USA New Cases[B]	Potential Canadians[C]	Potential Americans[C]
Colorectal	~3.2%	25,055	132,700	801	4,246
Breast	~0.8%	25,168	235,030	201	1,873
Lung	~2.6%	26,100	224,210	691	5,751
Uterine	~4.2%	6,000	52,630	263	2,305

[A] Only The Cancer Genome Atlas (TCGA) data[33] has been included as they are the most recent and comprehensive genome-wide, gene re-sequencing datasets available.

[B] The 2015 estimated incidence of newly diagnosed individuals in Canada[1] and the United States[2].

[C] The potential number of Canadians and Americans with somatic *RAD54B* alterations are calculated by multiplying the frequency within a given caner type by the number of newly diagnosed patients in 2015. The number of patients diagnosed with any given cancer type was retrieved from the Canadian Cancer Statistics[1] and the American Cancer Society[2].

CHAPTER 3: MATERIALS AND METHODS

3.1 REAGENTS

Appendix A contains a list of the solutions and the reagents used throughout this study (pg. 106). In general, all reagents were purchased through Corning, Thermo Scientific, Fisherbrand, Gibco, Invitrogen, Sarstedt, Sigma-Aldrich and VWR.

3.2 CELL CULTURE

Adherent human cancer and immortalized cell lines were utilized in the experiments of this study. The three cells lines employed in this thesis are HCT116, hTERT and HT1080 (Table 3.1). HCT116 cells were cultured in McCoy's 5A (HyClone) medium supplemented with 10% fetal bovine serum (FBS; Sigma-Aldrich). hTERT and HT1080 cells were cultured in Dulbecco's modified Eagle's medium (DMEM; Thermo Scientific) supplemented with 10% FBS. All cells were grown on 20 cm tissue culture dishes (Sarstedt) and initially seeded at ~30-50% confluency. Cells were maintained in a humidified Sanyo CO_2 incubator, at 37°C and 5% CO_2, until confluency reached ~80%. Generally, cells were detached and reseeded every 2-3 days (see below).

3.2.1 Cell Passaging Protocol

All cell culture passaging and manipulations were performed in a biological safety cabinet. For passaging, media was aspirated and cells were washed with 1× phosphate buffered saline (PBS), followed by the addition of 3 mL of 0.05% trypsin (Fisher Scientific) containing Ethylenediamine Tetraacetic Acid (EDTA; Fisher Scientific) for 5 minutes (min). Cells were monitored with an inverted ID03 microscope (Zeiss) using a 10× objective to ensure detachment from the culture dish. After trypsin treatment, 6 mL of media supplemented with 10% FBS was added to inactive the trypsin. Cells were transferred into a 15 mL conical tube (Sarstedt), and

Table 3.1: Common Properties of the Three Cell Lines Employed in this Study

	HCT116	**hTERT**	**HT1080**
Organism	Human	Human	Human
Tissue	Colon	Foreskin	Connective Tissue
Cell Type/Disease	Epithelial, CRC, transformed	Fibroblast, immortalized with hTERT	Connective Tissue, Fibrosarcoma, transformed
Culture Properties	Adherent	Adherent	Adherent
Gender	Male	Male	Male
Culture Medium	McCoy's 5A + 10% FBS	DMEM + 10% FBS	DMEM + 10% FBS
Approximate Doubling Time	22 h	36 h	22 h
Karyotype	Near Diploid 45, XY Stable	Diploid 46, XY Stable	Diploid 46, XY Stable
Source	American Type Culture Collection	C. P. Case (University of Bristol, Bristol, UK)[140]	Dr. J. Chubb (University College London, UK)[141]

washed with 4 mL of 1×PBS. A total volume of ~13 mL was centrifuged at 800 revolutions per minute (rpm) for 5 min in a Thermo Scientific Legend XFR centrifuge. Supernatant was aspirated, and the cell pellet was resuspended with ~3-8 mL of 1×PBS, and subsequently dispensed into a 20 cm culture dish containing 20 mL of the appropriate growth medium.

3.2.2 Cell Counting Protocol

Cells were passaged as described above, however following centrifugation the cell pellet was resuspended in ~4-10 mL of 1×PBS and transferred to a 50 mL conical tube (Sarstedt) through a 40 μm cell strainer (Falcon). A 40 μL aliquot of resuspended, strained cells was mixed in a 1:1 ratio with 0.2% trypan blue stain (Gibco) in a 0.5 mL microcentrifuge tube. A volume of 10 μL of this mixture was dispensed into a cell counter slide (Cedex Smart Slide, Roche) in duplicate. Cell counts (i.e. the number of viable cells/mL) were determined using the Cedex XS cell counter. Live cells were distinguished from the dead cells through standard dye exclusion and were automatically performed by the image analysis software. The average live cell count was used to determine an appropriate dilution of cells needed for experiments.

3.3 SMALL INTERFERING RNA (siRNA) AND TRANSFECTION

Four individual ON-TARGET plus siRNA duplexes (2 nmol) were purchased from (Dharmacon, GE). To resuspend siRNAs and generate 20 μM stock solutions, each tube was centrifuged and the pellet was resuspended in 100 μL of 1×siRNA buffer (Dharmacon, GE). To fully resuspend the siRNA duplexes the tubes were vortexed for 30 min (Vortex Genie 2, VWR) at room temperature. Working concentrations of siRNA duplexes (10 μM) were prepared by diluting the stock solutions 1:2 with 1×siRNA buffer. For each gene target, a pooled siRNA duplex (all 4 individual siRNA duplexes combined) was prepared from the 10 μM aliquots by mixing equivalent volumes of each individual duplex together. The siRNA suspensions were dispensed in small volumes (e.g. 20 μL) to minimize freeze-thaw cycles, and stored at -80°C.

For siRNA transfection, appropriate numbers of cells/well (Table 3.2) were seeded and transfected 24 h later with siRNAs. Table 3.2 provides volumes of siRNA, RNAiMAX and serum free media required for the two plate formats employed in these experiments. siRNAs were complexed with RNAiMAX as detail by the manufacturer before delivery to wells. 24 h post transfection appropriate growth media was supplemented into each well. Following 3.5-4.5 days of growth, protein was harvested from experiments in 6-well plates (detailed in Section 3.4, pg. 38) and 96-well plates were fixed with 4% (w/v) paraformaldehyde in 1×PBS (Appendix A).

Table 3.2: Cell Seeding Density, siRNA and RNAiMAX Dilutions Required for siRNA Transfection in 6-well or 96-well Plates

		Tube 1: Diluted siRNA (µL/well)		**Tube 2: Diluted RNAiMAX (µL/well)**			
Plate format	Cells / well	Volume of 10 µM siRNA (µL)	Serum-free medium (µL)	Volume of RNAiMAX (µL)	Serum-free medium (µL)	Complete medium (µL/well)	Total transfection volume (µL/well)
6 well	64000	1	250	3	250	2000	2500
96 well	4000	0.1	10	0.3	10	200	220

3.4 WESTERN BLOT ANALYSIS

Cells were cultured as above, however 6-well culture dishes were employed for protein extraction experiments. Asynchronous cells in 6-well culture dishes were washed with cold 1×PBS three times. In a cold room (4°C), 200 µL of lysis buffer (Appendix A) was added to each well and incubated for 5 min. Cells were collected using a cell scraper (VWR) and the samples were transferred to a 1.5 mL centrifuge tube. Samples were sonicated using the Sonifer Cell Disrupter (Branson Sonic Power Co.) in two rounds for ~2 seconds (sec) each. Samples were centrifuged (Biofuge Fresco, Heraeus) at 13,000 rpm at 4°C for 2 min. The supernatant was removed by micropipette and transferred to a sterile 1.5 mL plastic tube. Samples were stored at -20°C for short periods (~2 weeks), or -80°C for long periods (>2 weeks).

Protein extracts were quantified using the Pierce BCA (bicinchoninic acid) Protein Assay Kit (Thermo Scientific) as described by the manufacturer. Briefly, the concentration of each sample was determined by comparing its absorbance to that of a standard curve generated from a series of nine protein standards. To generate the standard curve, absorbance measurements (562 nm) were determined using the Cytation 3 (BioTek). This standard curve was employed to determine the unknown sample(s) protein concentration.

Western blotting was performed using denaturing polyacrylamide gel electrophoresis. Briefly, samples containing 10-30 µg of protein were prepared in 5× sodium dodecyl sulfate/dithiothreitol (SDS/DTT) Sample Buffer (Appendix A) and incubated in a Thermomixer R (Eppendorf) at 95°C for 10 min. Protein samples were loaded into wells of the gel (BioRad, Mini-Protean TGX) and electrophoresed in a gel apparatus containing running buffer (Appendix A) at 4°C for 60 min under constant voltage (140 V) by PowerPac HC (BioRad). Proteins from the gel were transferred to a polyvinylidene difloride (PVDF) membrane (Millipore) of 0.45 µm pore size. Prior to transfer, the PVDF membrane was activated with a flash rinse of ~5 mL of methanol (VWR), followed by 3 rinses in MilliQ water. Protein transfer to the PVDF membrane was performed using a semi-dry transfer apparatus (BioRad) in transfer buffer (Appendix A) at 14 V for 45 min.

To confirm protein transfer the membrane was stained with copper phthalocyanine 3, 4', 4'', 4'''-tetrasulfonic acid tetrasodium salt (CPTS; Appendix A). The membrane was destained in TBS-Tween20 (TBST; Appendix A) for 5 min with gentle agitation. The membrane was blocked with 5% non-fat milk in TBST (Appendix A) for 1 hour (h) with gentle agitation. Following blocking, the membrane was sealed in a plastic bag containing 5-8 mL of the appropriate primary antibody (Table 3.3) diluted in 5% non-fat milk, and incubated overnight at 4°C with gentle agitation. The following day, the membrane was washed three times in TBST for 10 min each with gentle rocking. The membrane was incubated with the appropriate secondary antibody (Table 3.3) diluted in 5% non-fat milk for 1 h at room temperature with gentle rocking, followed by three additional TBST washes as above. Finally, 750 µL of SuperSignal West Dura Extended Duration Substrate (Thermo Scientific) was prepared as described by the manufacturer and was placed on Saran wrap. The membrane was placed onto the substrate for 5 min at room temperature and protected from the light. Excess substrate was removed by dabbing on a Kimwipe, and the membrane was placed in a plastic page protector. Protein bands were visualized using the My ECL imager (ThermoFisher Scientific) equipped with a 16-bit, 4.2 megapixel, thermoelectrically regulated (-25°C) charge-coupled device camera (Thermo Scientific). Membranes were imaged with various exposure times to identify the optimal signal intensity. Images were exported as TIFF files and compiled in Photoshop CS6 (Adobe).

Table 3.3: Antibody Dilutions Employed in this Study

Primary Antibodies	**Catalogue Number**	**Dilution**	**Species**[a]	**Source**
RAD54B	N/A	1:1000	R	K. Miyagawa
PARP1	ab6079	1:7500	R	Abcam
α-Tubulin	ab7291	1:20000	M	Abcam
γ-H2AX	ab26350	1:200	M	Abcam
Cleaved Caspase-3	ab13847	1:200	R	Abcam
Secondary Antibodies				
Goat α Rabbit HRP[b]	111-035-144	1:15000	G	Jackson Immunoresearch Labs
Goat α Mouse HRP[b]	115-035-146	1:10000	G	Jackson Immunoresearch Labs
Goat α Rabbit AlexaFluor 488	ab150081	1:200	G	Abcam
Goat α Mouse AlexaFluor 488	ab150117	1:200	G	Abcam

[a] species; rabbit (R), mouse (M), goat (G)
[b] Horesradish peroxidase (HRP)

To assess equivalent protein loading, membranes were stripped and reblotted with anti-αTubulin as a loading control. Membranes were washed in 1×Re-Blot Strong Solution (Millipore) for 30 min, and incubated with the appropriate primary and secondary antibodies as detailed above beginning with blocking in 5% non-fat milk.

To determine the relative protein expression levels following silencing, raw TIFF images were quantified using ImageJ software (v2.00). The band intensity of each lane was quantified for both the protein of interest and the loading control (α-Tubulin), and each band was normalized to the corresponding loading control. All data are presented relative to the negative control (si*GAPDH*), which is set to 1.0 (100%).

3.5 SMALL MOLECULE INHIBITOR (SMI) DOSE RESPONSE CURVES

Standard dose response curves were generated using a 10-fold serial dilution of BMN673 (20 μM to 200 fM) or Olaparib (200 μM to 2 pM). Briefly, 4000 cells in 200 μL of media were dispensed into each well of a 96-well plate. The following day, 100 μL of media supplemented with appropriate concentrations of BMN673, Olaparib or vehicle control (Dimethyl sulfoxide; DMSO) were added to each well in sextuplet. Following 3.5 days of growth, cells were fixed with 4% (w/v) paraformaldehyde (Appendix A) and nuclei were counterstained with Hoechst 33342 (300 ng/mL; Thermo Scientific) diluted in 1×PBS. Plates were stored at 4°C overnight and imaged the following day (detailed in Section 3.9.2, pg. 46). Imaging data (i.e. nuclear counts) were imported into Prism v5.0 (GraphPad) and normalized to DMSO control. All data was transformed to a log scale and dose response curves were fit using a sigmoidal nonlinear regression model. An Effective Concentration 50 (EC_{50}) value was determined from the dose response curve, which is the concentration of the SMI that results in 50% of cell survival compared to the DMSO control. The EC_{50} values calculated for the *RAD54B*-deficient line were employed in all subsequent experiments.

3.6 REAL-TIME CELLULAR ANALYSES

Real-time cellular analyses (RTCA) (i.e. growth curves) were performed in quadruplicate using an RTCA-dual plate (RTCA-DP; Acea Biosciences) instrument housed within a 37°C incubator. The RTCA-DP system employs microelectrodes at the bottom of each well to measure increases or decreases in electrical impedance (termed cell index) that reflect increases or decreases in cells numbers, respectively. Briefly, 4000 cells/well were seeded into an E-plate and growth was monitored every 15 min at 37°C. 24 h post-seeding, media containing BMN673, Olaparib or DMSO was supplemented in appropriate wells and growth was monitored for ~4 additional days. All data were imported into Prism and growth curves were plotted for each condition. A Proliferation Defect (PD) was calculated for each cell line at the time point where the *RAD54B*-deficient DMSO treated growth curves reached their apex, immediately prior to the stationary phase. Below is the formula employed to calculated the PD:

$$\mathrm{PD} = \left\{ 1- \left(\frac{\text{Cell Index}_{\text{Drug}}}{\text{Cell Index}_{\text{DMSO}}} \right) \right\} \times 100$$

3.7 MODIFIED TWO DIMENSIONAL (2D) COLONY FORMING ASSAYS

To identify the optimal cell seeding density for the modified 2D colony forming assays (mCFAs), cells were seeded in a 2-fold serial dilution (8000 to 250 cells/well) into 24-well plates (Corning). One day post seeding, BMN673, Olaparib or DMSO was added to growth media and cells were permitted to grow for an additional 7 days. Cells were fixed with 4% (v/w) paraformaldehyde for 10 min and stained with crystal violet (0.005% solution; Sigma) for 15 minutes. Images of the 24-well plates stained with crystal violet were acquired using a flat bed scanner (HP Officejet 4620), and saved as 8-bit greyscale TIFFs. Based on image analysis, an optimal seeding density of 1000 cells/well was identified. Next, mCFAs were performed utilizing the optimal cell seeding density (1000 cells/well) with cells treated with BMN673, Olaparib or DMSO as above, but in sextuplet. Images were collected as above and image intensity thresholding was performed on the scanned images from which a binary mask was generated to reflect cell confluency. Next, a circle of a fixed diameter was applied to each individual well and the average pixel intensity within the circle was determined. Finally, the mean signal intensities for each condition were calculated by averaging the six replicates, and presented relative to the appropriate control.

3.8 INDIRECT IMMUNOFLUORESCENCE (IIF) LABELING

Cells were seeded onto ethanol-sterilized glass coverslips (18 × 18 mm) in a 6-well culture plate so that they were ~80% confluent prior to fixation. After the appropriate amount of time, cells were fixed with freshly prepared 4% (w/v) paraformaldehyde (Appendix A) in 1×PBS for 10 min at room temperature. Once fixed, the paraformaldehyde was removed and the cells were washed three times with 1×PBS. Cell membranes were permeabilized with 1×PBS containing 0.5% (v/v) Triton X-100 (Appendix A) for 10 min at room temperature. Following three additional 1×PBS washes, coverslips were inverted onto parafilm containing a 30 μL aliquot of primary antibody (diluted in 1×PBS; Table 3.3, pg. 40). A plastic lid was placed over the coverslips to prevent desiccation and the cells were incubated overnight at room temperature. Coverslips were returned to the 6-well culture plate and rinsed once with 1×PBS and incubated with 1×PBS containing 0.1% (v/v) Triton X-100 (Appendix A) for 5 min. Coverslips were rinsed three additional times with 1×PBS and placed onto a 30 μL aliquot of secondary antibody (diluted in 1×PBS; Table 3.3, pg. 40). Cells were covered as before and incubated at room temperature for at least 1 h in the dark. The coverslips were returned to the 6-well plate and rinsed with 1×PBS containing 0.1% (v/v) Triton X-100, followed by three additional washes of 1×PBS. Coverslips were mounted onto glass slides containing ~10 μL of DAPI in mounting media (Appendix A). Slides were rinsed once with Milli-Q water to remove any residual PBS crystals that could negatively influence image quality. Slides were maintained in the dark at 4°C to prolong their photostability. Images were typically acquired the following day.

For IIF labeling following SMI treatments, medium containing BMN673, Olaparib or DMSO was added to appropriate wells 24 h post cell seeding and grown for an additional 48 h. IR and Staurosporine were used as positive controls for DNA DSBs (γ-H2AX labeling) and apoptosis (cleaved Caspase-3 labeling), respectively. To induce DNA DSBs, cells were treated with 2 Gy of IR using the RS 2000 X-ray Irradiator (RAD Source Technologies) and paraformaldehyde fixed 20 min post treatment. To induce apoptosis, cells were treated with 1 μM of Staurosporine (Abcam, ab120056) and fixed 5 h post treatment. All cells were labeled using the labeling protocol described above.

3.9 MICROSCOPY

Three distinct types microscopy were utilized throughout this thesis: 1) high resolution IIF microscopy to validate antibodies, 2) high content, quantitative imaging microscopy to enumerate nuclei, and 3) high content, semi-quantitative IIF imaging with antibodies to reveal abundance and localization of proteins after SMI treatment. Each of these approaches is detailed below.

3.9.1 High Resolution Indirect Immunofluorescence Microscopy

High resolution IIF microscopy was performed to validate the RAD54B, γ-H2AX and cleaved Caspase-3 antibodies for future studies. Imaging was performed using an AxioImager Z1 Microscope (Zeiss) equipped with a 16-bit gray scale AxioCam HR charge-coupled device (CCD) camera (Zeiss). All images were collected with a 63× oil-immersion plan apochromat objective (Numerical aperture; NA = 1.4). The exposure times for the DAPI and AlexaFluor488 channels were first optimized for the positive control. All images were collected with identical exposure times and thus semi-quantitative imaging analyses were used to reveal changes in the abundance of a particular fluorescently labeled epitope. Images were assembled in Imaris v7.7.2 (Bitplane) image analyses and presentation software. Briefly, all channels (e.g. DAPI and AlexaFluor 488) were imported into Imaris and the pixel dimensions were adjusted to reflect the pixel dimensions of the camera and 63× objective (x × y dimensions; 0.102 µm × 0.102 µm). Individual channels were false coloured white, while the merged images were pseudo-coloured red or green for the DAPI and AlexaFluor 488 channels, respectively. All images were exported as TIFFs and montages were assembled in Adobe Photoshop CS6.

3.9.2 High Content Imaging to Enumerate Nuclei

High content imaging microscopy was performed using the Cytation 3 (BioTek) equipped with a 16-bit gray scale 1.25 megapixel Sony charge-coupled device camera and a motorized stage. All images were collected with an Olympus 10× objective (NA = 0.3) using the autofocus feature contained within the Gen5 software (BioTek). Exposure times were optimized for Hoechst and maintained constant through the entire image acquisition. Nine central and non-overlapping images were acquired per well, and the total number of nuclei was determined using an automated nuclear counting algorithm contained within Gen5. All data were imported into Prism v6.0 (GraphPad), normalized to negative control, and basic statistical analyses (e.g., mean, standard deviation, Student's *t*-test) were performed.

3.9.3 High Content Semi-Quantitative Indirect Immunofluorescence Imaging

High content semi-quantitative IIF imaging was performed using the Cytation 3 equipped with an Olympus 20× objective (NA = 0.45) and Gen5 software. Exposure times for the positive control were optimized for DAPI and GFP, and maintained constant throughout the image acquisition process. In general, a 2×2 image montage was acquired from each well with overlapping edges so that image stitching could be automatically performed within Gen5. Next, the total number of nuclei within each stitched image was determined as detailed above. A nuclear boundary (i.e. nuclear mask) was defined in Gen5 and the total signal intensity for the GFP channel was determined at the single cell level.

3.10 STUDENT'S *t*-TESTS

Student's *t*-tests were employed throughout this thesis to identify statistically significant differences between two means that are assumed to follow a normal distribution and exhibit equal variance within each group. Unpaired Student's *t*-tests were calculated using Prism v5.0

(GraphPad) to determine if significant differences exist between control (*RAD54B*-proficient cells) and experimental (*RAD54B*-deficient cells) following various experimental conditions. A *p*-value of <0.05 is considered to be statistically significant and is strongly suggestive of different means.

3.11 MULTIPLICATIVE MODEL

A multiplicative model was employed to determine if the combined effects of two individual treatment conditions were greater than that predicted by the product of the individual treatments. The formula employed in this model was:

$$\mathrm{A} \times \mathrm{B} = \mathrm{E}$$

where A is the relative percentage of cells remaining following *RAD54B* silencing, B is the relative percentage of cells remaining following *PARP1* silencing and E is the expected product of the combined treatments. If the observed relative percentage of cells remaining is beyond that predicted by the multiplicative model (i.e. fewer cells remaining within the combined condition than predicted by the model), the response of the combined treatment conditions is said to be synergistic.

CHAPTER 4: RESULTS

4.1 AIM 1: TO IDENTIFY AND VALIDATE *PARP1* AS A SYNTHETIC LETHAL INTERACTOR OF HUMAN *RAD54B* IN COLORECTAL CANCER CELLS

To determine whether *PARP1* is SL with *RAD54B*, we employed an established siRNA-based approach using isogenic *RAD54B*-proficient (control) and *RAD54B*-deficient (experimental) cells[4,85]. This model was developed in HCT116 cells[49], which is a karyotypically stable, CRC cell line of epithelial origin (Table 3.1; pg. 34) that has been previously utilized in similar SL studies[4,85].

4.1.1 Validation of the *RAD54B* HCT116 Isogenic Model

Prior to evaluating a putative SL interaction between *RAD54B* and *PARP1* it was first necessary to confirm the cellular models employed in this study. Accordingly, *RAD54B* expression was evaluated by Western blots and IIF and confirmed to be present within the control cells and absent from the *RAD54B*-deficient cells (Figure 4.1). Furthermore, IIF revealed the expected nuclear-enriched RAD54B localization pattern within the *RAD54B*-proficient cells that was notably absent from the *RAD54B*-deficient cells, and is in agreement with its nuclear role in DNA damage repair. Thus, these data confirm the expected *RAD54B* expression and localization patterns within the isogenic model and identify it as a suitable model to be employed throughout the remaining studies.

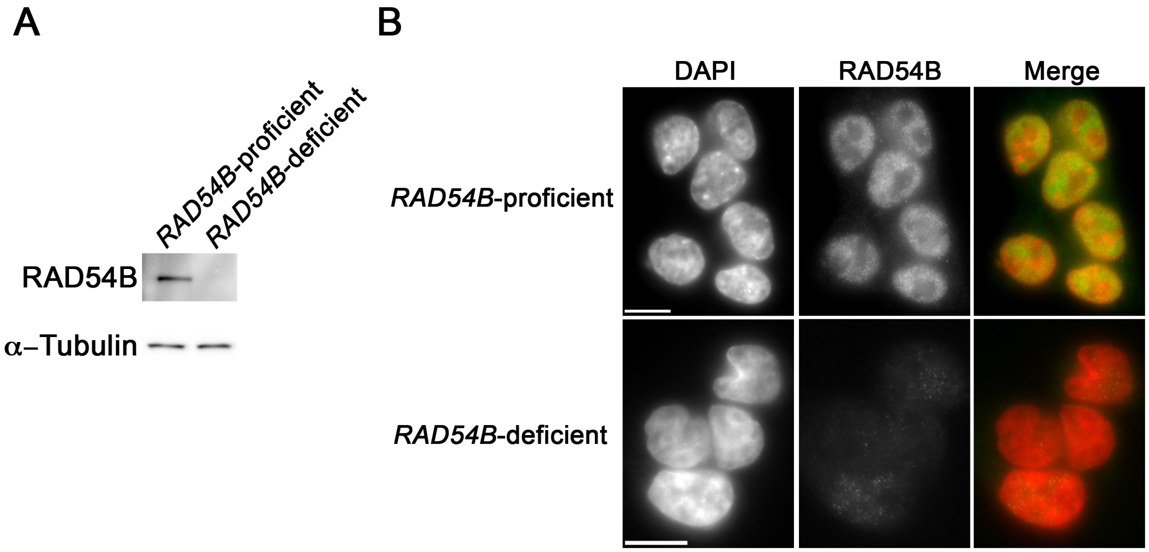

Figure 4.1: Evaluating RAD54B Expression within the *RAD54B*-proficient and *RAD54B*-deficient HCT116 Cells
(A) Western blot confirming RAD54B expression within the *RAD54B*-proficient cells and absence within the *RAD54B*-deficient cells; α-Tubulin serves as the loading control. ***(B)*** Indirect immunofluorescence images presenting RAD54B expression and localization within *RAD54B*-proficient cells and lack of expression within the *RAD54B*-deficient cells. Note that identical exposure times were employed for both cell lines. DAPI and RAD54B are pseudo-colored red and green, respectively, within the Merge. (Scale bar = 10μm).

4.1.2 Evaluating the Silencing Efficiency of *PARP1* siRNA Duplexes in HCT116

Before examining a potential SL interaction between *RAD54B* and *PARP1*, the silencing efficiency of a pooled siRNA (si*PARP1*-Pool) and four independent siRNA duplexes (si*PARP1*-1, si*PARP1*-2, si*PARP1*-3, si*PARP1*-4) targeting unique regions of *PARP1* were evaluated using semi-quantitative Western blots and compared with controls (Untransfected and si*GAPDH*) (Figure 4.2). Briefly, semi-quantitative Western blot analysis was performed by normalizing the signal intensities of a specific band of interest (e.g. PARP1) to that of the corresponding loading control (e.g. α-Tubulin). All data are presented relative to the negative control (e.g. si*GAPDH*), which is set to 100%. Based on this approach, the relative PARP1 expression levels following PARP1 silencing ranged from 17-43% of endogenous levels expressed within the si*GAPDH* control (Figure 4.2B). While si*PARP1*-Pool decreased PARP1 expression to ~18% of the control, the two most efficient individual duplexes were identified, si*PARP1*-2 and si*PARP1*-1 that decreased expression to ~17% and 21%, respectively, demonstrating our ability to efficiently silence *PARP1* expression. To minimize potential off-target effects associated with siRNA-based silencing, si*PARP1*-Pool and the two most efficient duplexes (si*PARP1*-1, -2) were used in all subsequent experiments.

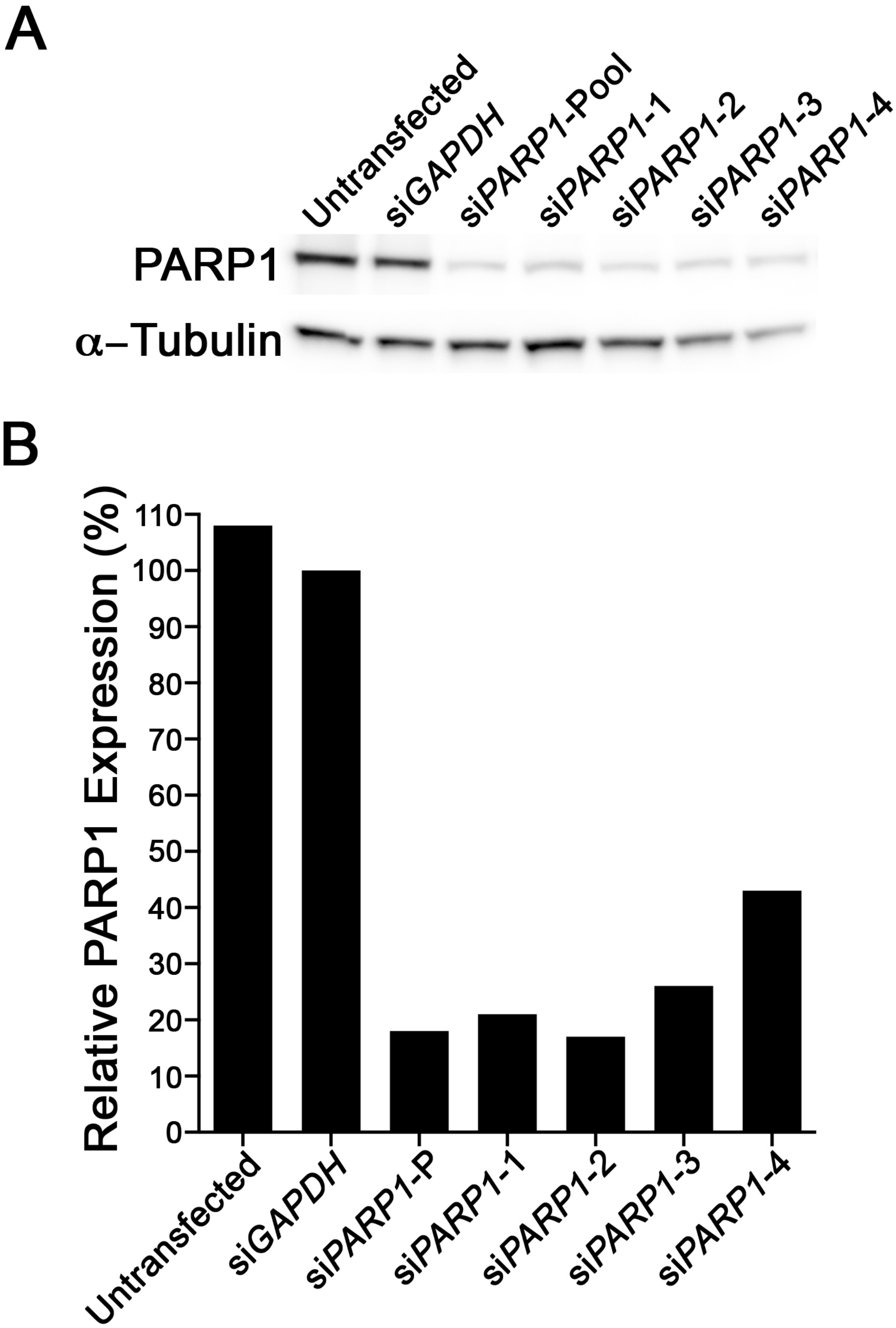

Figure 4.2: siRNA-based Silencing of PARP1 in HCT116
(A) Western blot depicting diminished PARP1 expression within *RAD54B*-proficient cells following si*PARP1* relative to controls (Untransfected and si*GAPDH*); α-Tubulin serves as the loading control. Presented is a single representative example of an experiment repeated a total of three times with similar results. ***(B)*** Bar graph depicting the normalized abundance of PARP1 relative to the negative control (si*GAPDH*), as determined by semi-quantitative analysis of the Western blot presented in ***(A)***.

4.1.3 *RAD54B* and *PARP1* are Putative Synthetic Lethal Interactors in HCT116 Cells

Having validated RAD54B expression within the isogenic HCT116 model (Section 4.1.1, pg. 48) and identified the most efficient *PARP1* silencing duplexes (Section 4.1.2, pg. 50), direct SL tests were performed to determine whether *PARP1* is SL with *RAD54B*. Briefly, control (*RAD54B*-proficient) or *RAD54B*-deficient cells were seeded into 96-well plates, and transfected in sextuplet with si*PARP1*-Pool, si*PARP1*-1, si*PARP1*-2 or control siRNAs (si*GAPDH* or si*PLK1*). *GAPDH* is as an established negative control that does not induce a SL interaction with *RAD54B*[4,85], while *PLK1* is an essential mitotic kinase whose silencing normally induces death independent of any SL interaction[142,143] and therefore serves as an indicator of transfection efficiency. Following siRNA transfection and 3.5 days of growth, cells were fixed, counterstained, imaged and the numbers of cells remaining were determined (Section 3.9.2, pg. 46). Conceptually, a SL interaction will result in fewer *RAD54B*-deficient cells remaining relative to controls following *PARP1* silencing. As predicted, there was a visual decrease in the number of *RAD54B*-deficient cells following PARP1 silencing relative to controls. More specifically, the *RAD54B*-deficient cells had a small, albeit statistically significant decrease in the relative percentage of cells remaining following *PARP1* silencing (Figure 4.3). More specifically, the relative percentage of *RAD54B*-deficient cells remaining decreased to 87.5-91.8% following *PARP1* silencing relative to si*GAPDH* (Table S2, pg. 113), which was ~3.6-6.2% beyond that observed within the *RAD54B*-proficient cells, representing a 1.04-1.07-fold change, respectively. It is interesting to note that the difference in the relative percentage of cells remaining in the *RAD54B*-deficient cells appears to correlate with the silencing efficiency of PARP1. For example, si*PARP1*-2 was the most efficient silencing duplex, and exhibited the greatest difference between the *RAD54B*- deficient cells and controls (1.07-fold change).

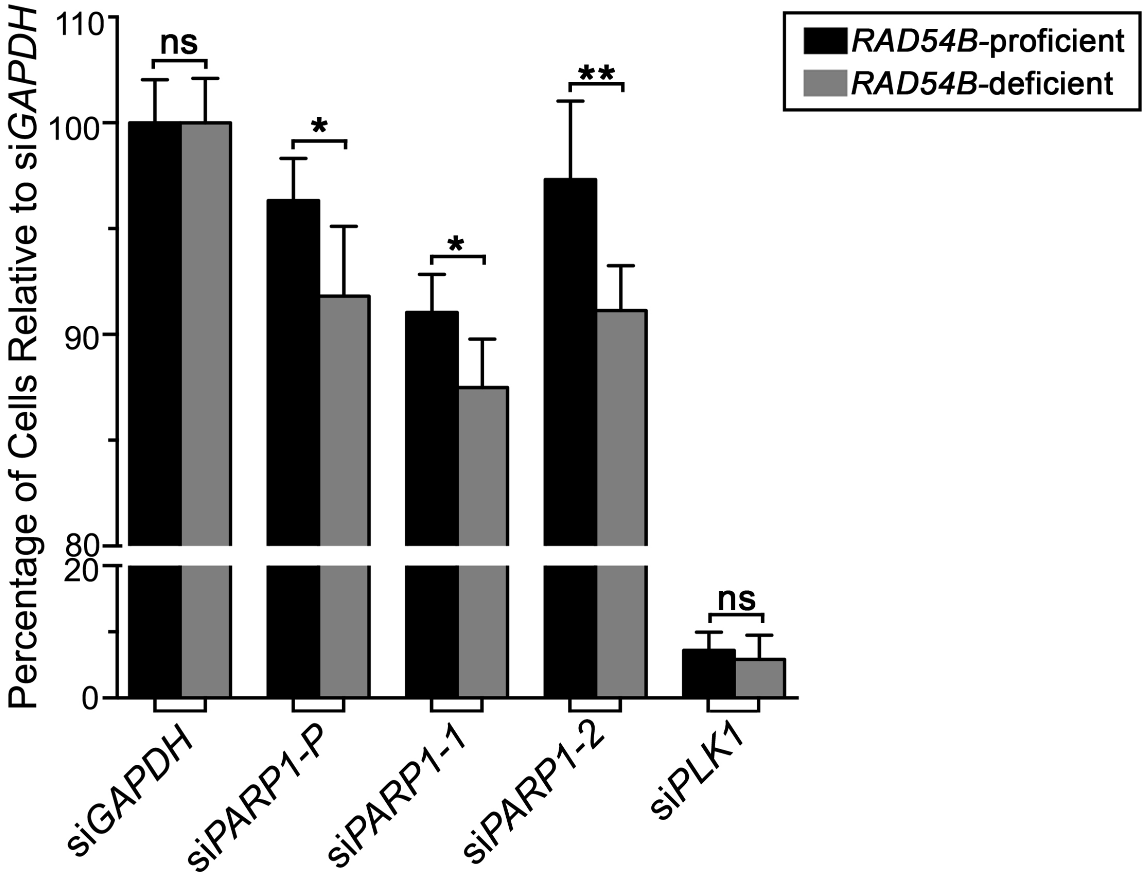

Figure 4.3: *RAD54B* and *PARP1* are Putative Synthetic Lethal Interactors in HCT116 Cells Bar graph depicting the mean normalized percentage of cells relative to si*GAPDH* (± Standard Deviation [SD]) for *RAD54B*-proficient (black) and *RAD54B*-deficient cells (grey) following transfection with the indicated (x-axis) *PARP1* or control siRNA duplexes. Student's *t*-tests reveal statistically significant decrease in the mean normalized cell numbers within the *RAD54B*-deficient cells relative controls. (***P*-value <0.01; **P*-value <0.05; ns, not significant, n=6). Presented is a single representative example of an experiment performed in sextuplet, with each experiment repeated two additional times with similar results.

Collectively, these data suggest that *PARP1* silencing selectively decreases the relative percentage of cells remaining within *RAD54B*-deficient cells, and is supportive of a putative *RAD54B PARP1* SL interaction in HCT116 cells.

4.1.4 Simultaneous *RAD54B* and *PARP1* Silencing Results in Decreased HCT116 Cell Numbers

Although the above data supports a SL interaction between *RAD54B* and *PARP1*, there remains the possibility that the SL interaction occurs due to a *de novo* background mutation that arose during the generation of the *RAD54B*-deficient cells. Since HCT116 cells are *MLH1*-deficient (DNA mismatch repair gene) and can accrue background mutations, there remains a possibility that a second mutation, unrelated to *RAD54B* became clonally fixed within the *RAD54B*-deficient cells that is actually responsible for the SL interaction. To assuage this possibility, dual silencing experiments were performed in which both *RAD54B* and *PARP1* were either individually or simultaneously silenced within the parental/control *RAD54B*-proficient cells. However, we first evaluated the silencing efficiency of both the pooled siRNAs (si*RAD54B*-Pool) and four individual *RAD54B* siRNA duplexes along with controls. As shown in Figure 4.4A, all conditions were highly effective at silencing RAD54B expression with relative expression levels typically ranging from 3-13% of control levels (Figure 4.4B). Accordingly, si*RAD54B*-Pool was selected for all subsequent experiments as it typically reduced RAD54B expression to ~7% of control levels.

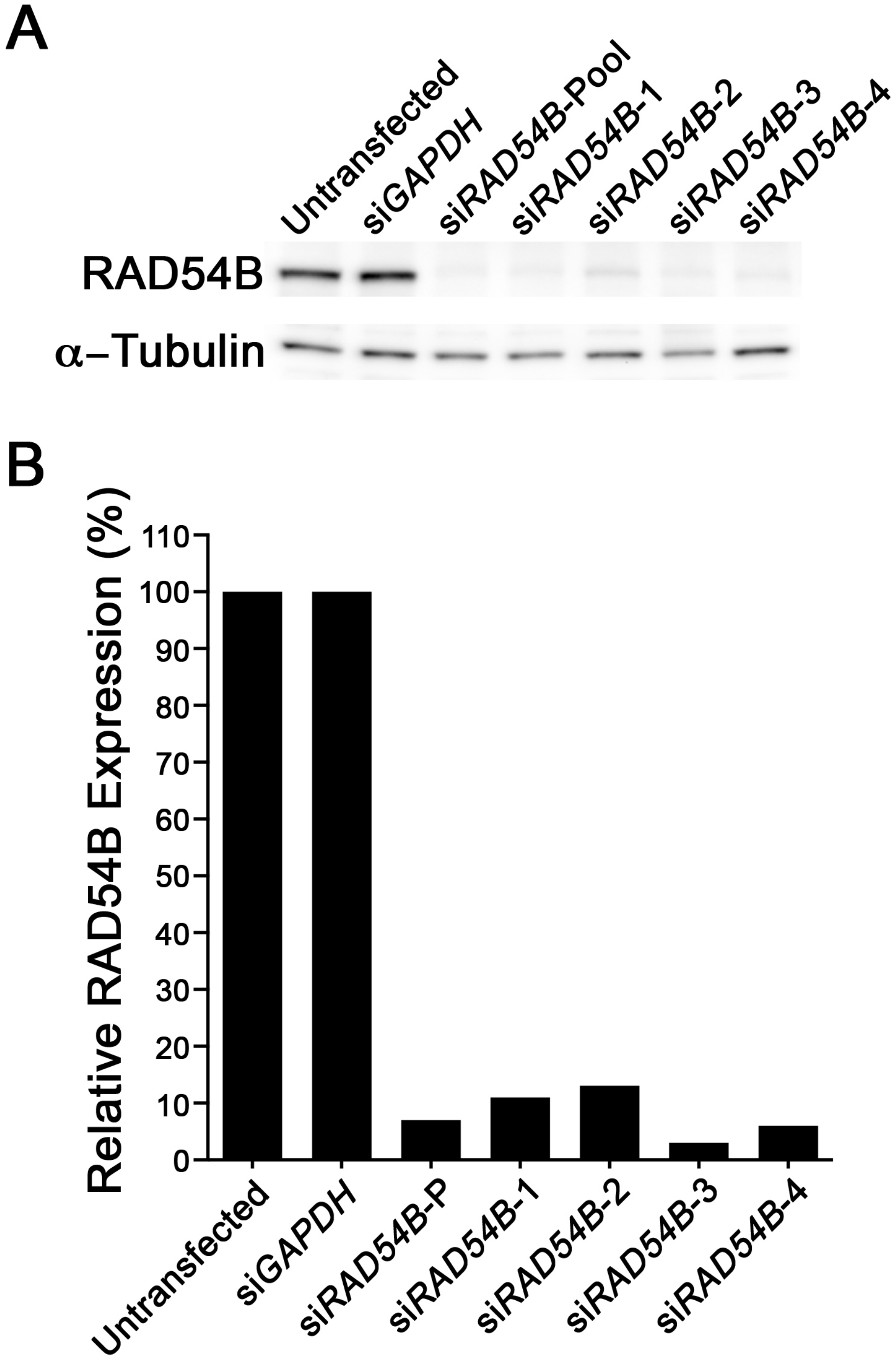

Figure 4.4: siRNA-based Silencing of RAD54B in HCT116
(A) Western blot depicting diminished RAD54B expression following si*RAD54B* relative to controls (Untransfected and si*GAPDH*); α-Tubulin serves as the loading control. Presented is a single representative example of an experiment repeated a total of three times. ***(B)*** Bar graph depicting the normalized abundance of RAD54B relative to the negative control (si*GAPDH*), as determined by semi-quantitative analysis for the Western blot in ***(A)***.

As anticipated, the simultaneous silencing of both *RAD54B* and *PARP1* resulted in a larger decrease in the mean percentage of cells than when either *RAD54B* or *PARP1* are silenced alone (Figure 4.5), or what is expected/predicted as calculated by a multiplicative model (detailed in Section 3.11, pg. 47). More specifically, the observed relative percentage of cells remaining after the dual silencing of *RAD54B* and *PARP1* was 18-26% smaller compared to the expected value as calculated using a multiplicative model (Table S3, pg. 114). Thus, these results show that the *RAD54B PARP1* SL interaction is independent of an unknown background mutation within the *RAD54B*-deficient cells. In addition, these data support those of the previous section and validate *PARP1* as a SL interactor of *RAD54B* in HCT116 cells. These data also identify PARP1 as a novel candidate drug target in *RAD54B*-deficient CRC cells.

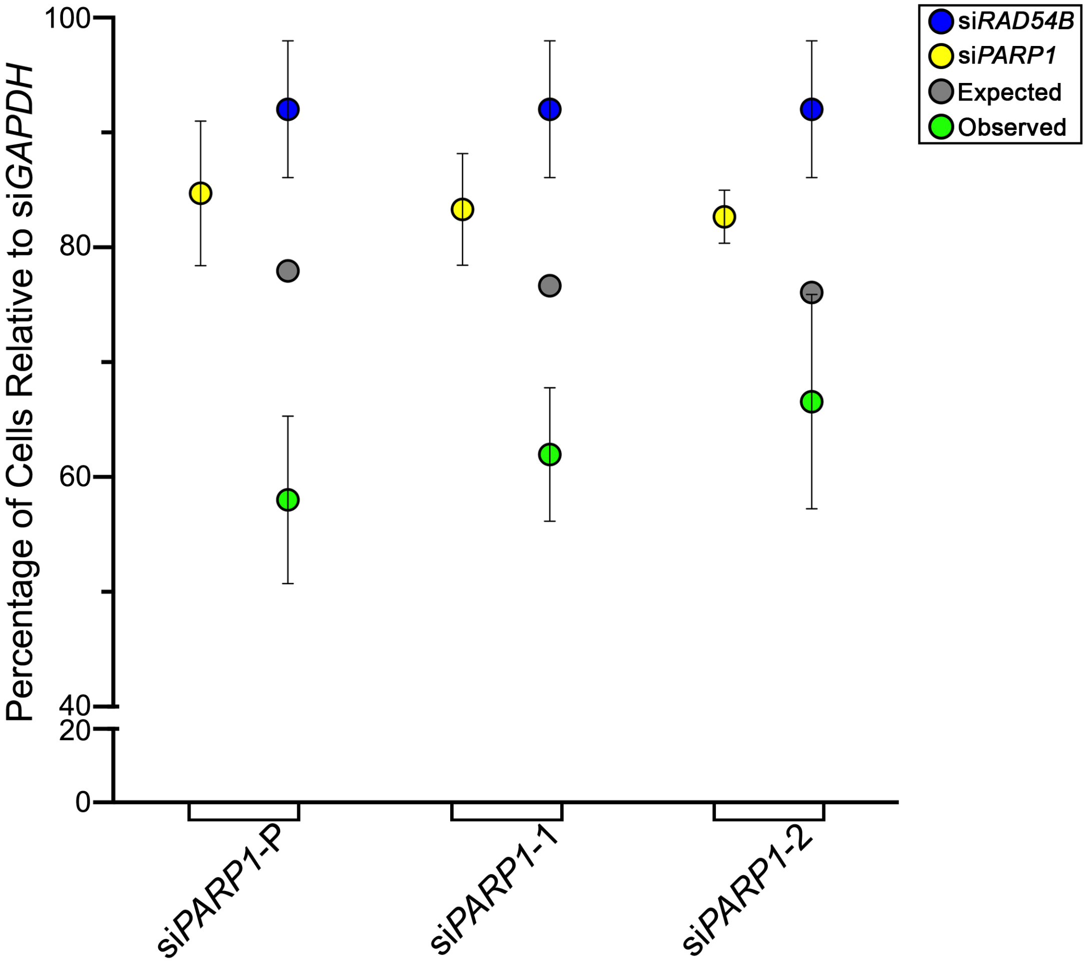

Figure 4.5: Simultaneous Silencing Validates Synthetic Lethal Interaction Between *RAD54B* and *PARP1*

Graphical depiction of the mean normalized percentage of cells relative to si*GAPDH* (± SD) for the individual silencing of either *RAD54B* (blue circles) or *PARP1* (yellow circles), and the expected combined value (grey circles) calculated using a multiplicative model. Green circles identify the observed values following the simultaneous silencing of *RAD54B* and *PARP1*, demonstrating a synergistic effect (n=6). Presented is a single representative example of an experiment performed in sextuplet, with each experiment repeated two additional times.

4.2 AIM 2: TO EVALUATE THE EFFICACY OF SMALL MOLECULE INHIBITORS, BMN673 AND OLAPARIB, AS THERAPEUTIC AGENTS IN COLORECTAL CANCER CELLS

The results from Aim 1 identify *RAD54B* and *PARP1* as SL interactors in HCT116 cells and further identify PARP1 as a novel candidate drug target in *RAD54B*-deficient CRC cells. To further explore this possibility and progress to more therapeutically relevant conditions (i.e. small molecule inhibitors [SMIs]), we wished to determine whether PARP1 inhibition could functionally substitute for PARP1 silencing and induce preferential killing within *RAD54B*-deficient cells. Specifically, we sought to determine the efficacy of two PARP1 SMIs, namely BMN673 and Olaparib, as lead candidate compounds for *RAD54B*-deficient CRC cells in a series of pre-clinical assays.

4.2.1 *RAD54B*-deficient HCT116 Cells are Hypersensitive to BMN673 and Olaparib

To determine whether BMN673 and Olaparib can substitute for *PARP1* siRNAs and induce SL killing, dose responses curves were first generated for each SMI within the isogenic cell lines. The experimental setup for the dose response curves is similar to that employed in Section 4.1.3 (pg. 52), but with SMIs or vehicle control (DMSO) substituting for siRNAs. The mean normalized percentage of cells remaining relative to DMSO were determined at each SMI concentration employed (Tables S4 & S5, pgs. 118 & 119) and are presented in Figures 4.6 & 4.7. From these curves the Effective Concentration 50 (EC_{50}) values were determined, and are the concentrations at which 50% of the cells remain relative to DMSO-treated controls. Standard dose response curves (Figures 4.6A & 4.7A) show that the *RAD54B*-deficient cells are hypersensitive to BMN673 and Olaparib treatments relative to controls. More specifically, the EC_{50} for BMN673 was 9.02 nM within the *RAD54B*-deficient cells relative to 17.48 nM within

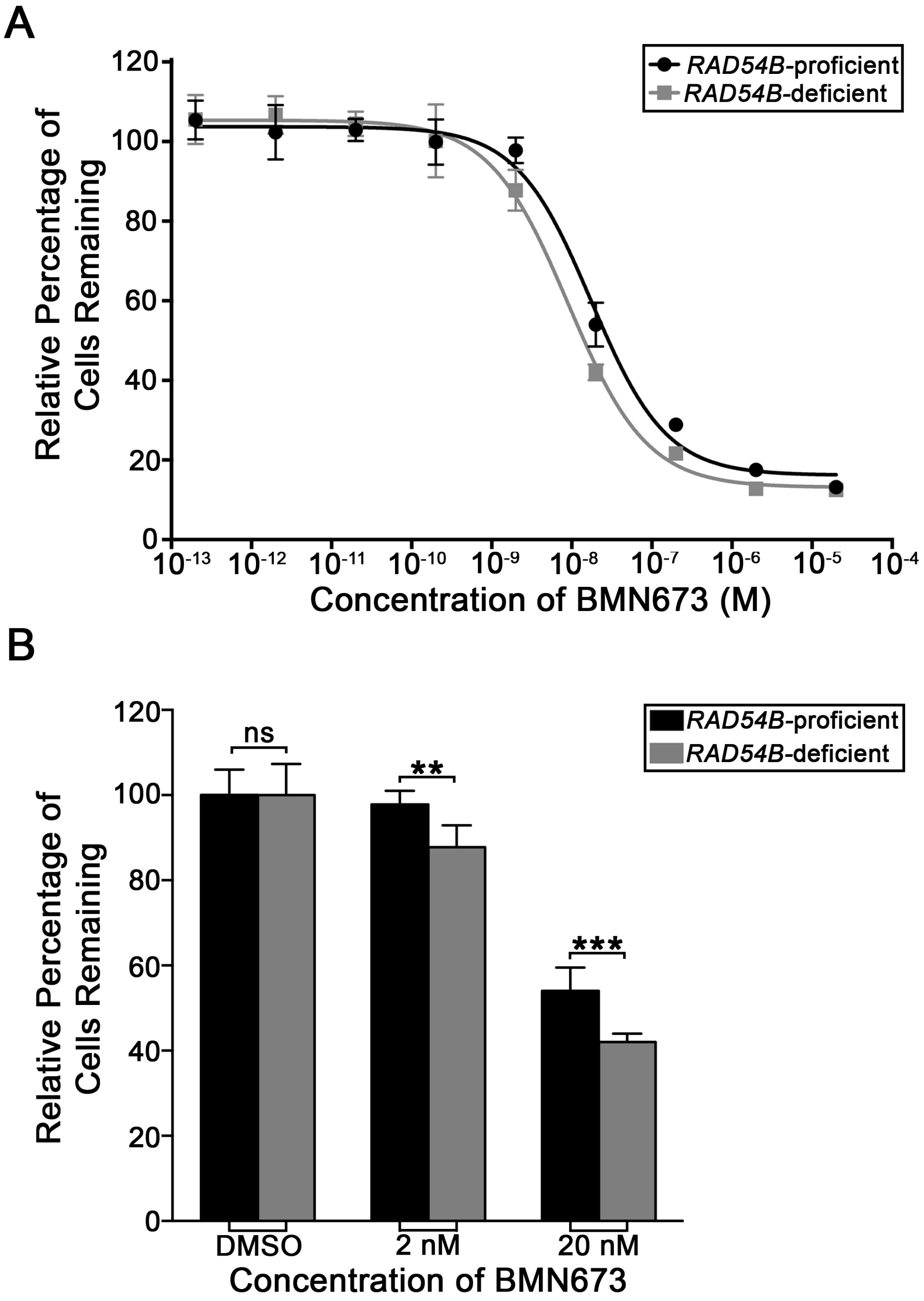

Figure 4.6: *RAD54B*-deficient Cells are Hypersensitive to BMN673
(A) Dose response curves for *RAD54B*-proficient and *RAD54B*-deficient cells treated with varying concentrations of BMN673. Data are presented normalized to the respective DMSO-treated controls (± SD, n=6). ***(B)*** Bar graph depicting the mean (± SD) percentage of *RAD54B*-proficient and *RAD54B*-deficient cells following DMSO or BMN673 treatment. Student's *t*-test reveal statistically significant decreases of *RAD54B*-deficient cells as compared to *RAD54B*-proficient cells. (****P*-value <0.001; ***P*-value <0.01; ns, not significant, n=6). Presented are the results of a single representative experiment. All experiments were performed in sextuplet and repeated two additional times with similar findings.

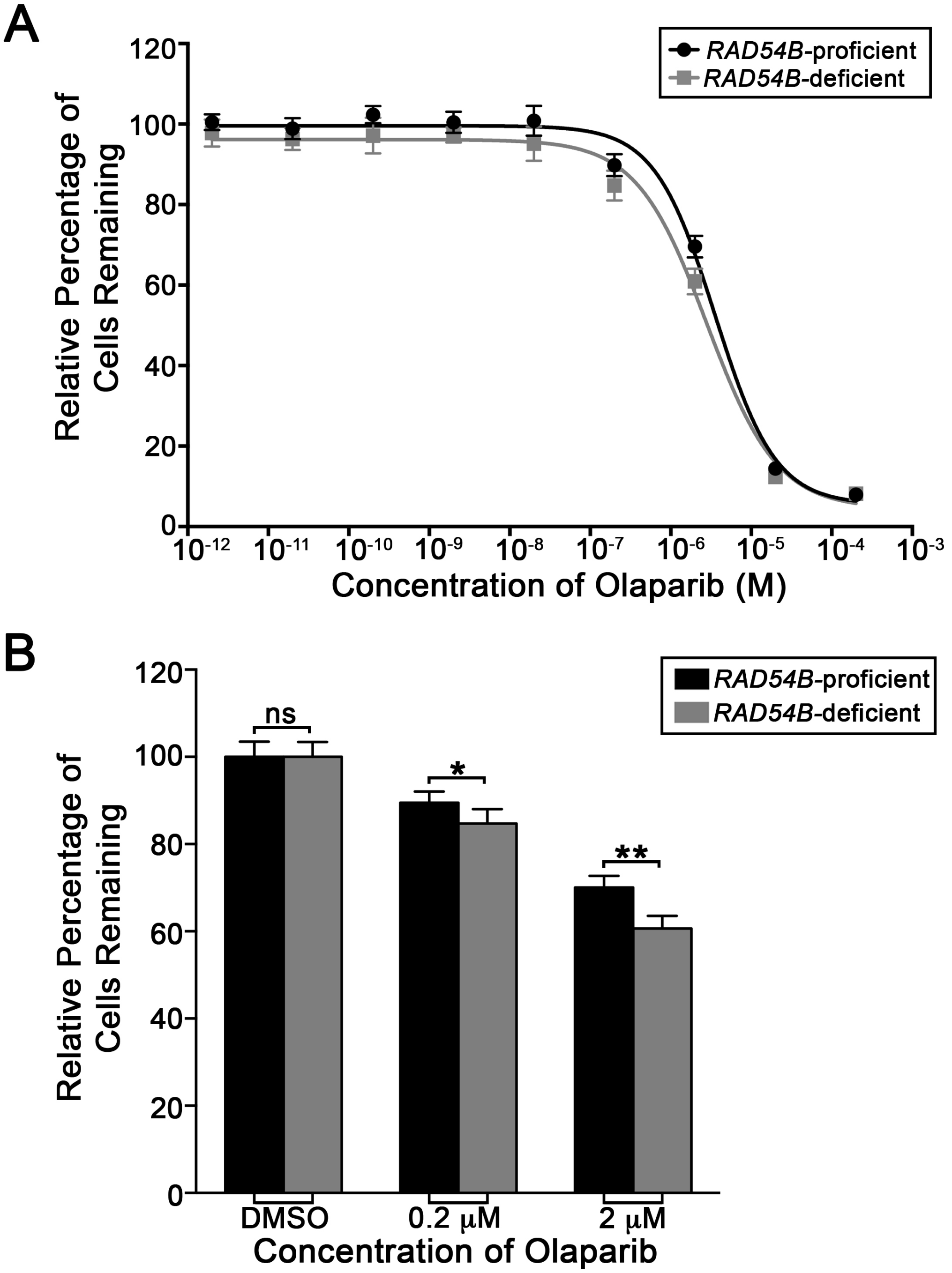

Figure 4.7: *RAD54B*-deficient Cells are Hypersensitive to Olaparib
(A) Dose response curves for *RAD54B*-proficient and *RAD54B*-deficient cells treated with varying concentrations of Olaparib. Data are presented normalized to the respective DMSO-treated controls (± SD, n=6). ***(B)*** Bar graph depicting the mean (± SD) percentage of *RAD54B*-proficient and *RAD54B*-deficient cells following DMSO or Olaparib treatment. Student's *t*-test reveal statistically significant decreases of *RAD54B*-deficient cells as compared to *RAD54B*-proficient cells. (**P*-value <0.05; ***P*-value <0.01; ns, not significant, n=6). Presented are the results from a single representative experiment. All experiments were performed in sextuplet and repeated two additional times with similar results.

the controls, and represents a 1.94-fold decrease. Subsequent Student's *t*-tests revealed a significant decrease in the percentage of cells remaining of *RAD54B*-deficient cells following BMN673 treatment at 2 nM and 20 nM compared to controls (Figure 4.6B, Table S4, pg. 115). Although not as large of a difference between the two cells lines, the EC_{50} value calculated for Olaparib was 2.82 μM for the *RAD54B*-deficient cells and 3.53 μM for the controls, representing a 1.25-fold decrease. As above, Student's *t*-tests revealed a significant decrease in the percentage of cells remaining of *RAD54B*-deficient cells following Olaparib treatment at 0.2 μM and 2 μM compared to controls (Figure 4.7B, Table S5, pg. 116). Collectively, these data indicate that *RAD54B*-deficient cells are hypersensitive to BMN673 and Olaparib treatments and further support a *RAD54B* and *PARP1* SL interaction. Importantly, and to best restrict killing to the *RAD54B*-deficient cells, the EC_{50} values calculated for BMN673 and Olaparib within the *RAD54B*-deficient cells were employed in all subsequent experiments.

4.2.2 BMN673 and Olaparib Treatments Inhibit Auto-PARylation

To confirm BMN673 and Olaparib were inhibiting PARP1 activity and not overtly impacting PARP1 expression levels, Western blots were performed on BMN673 and Olaparib treated samples. As presented in Figure 4.8, the DMSO treated control samples harbored a single band at ~113 kDa that corresponds to the established molecular mass of PARP1. In addition, a slower migrating "smear" was observed that is suggestive of the higher molecular mass of the auto-PARylated form(s) of PARP1. As expected, BMN673 and Olaparib treatments induced a visual decrease in the auto-PARylated form(s) of PARP1 (i.e. smear) and a corresponding increase the unmodified, ~113 kDa form of PARP1. These data suggest that BMN673 and Olaparib inhibit PARP1 auto-PARylation and further show that they do not dramatically impact the overall abundance of PARP1.

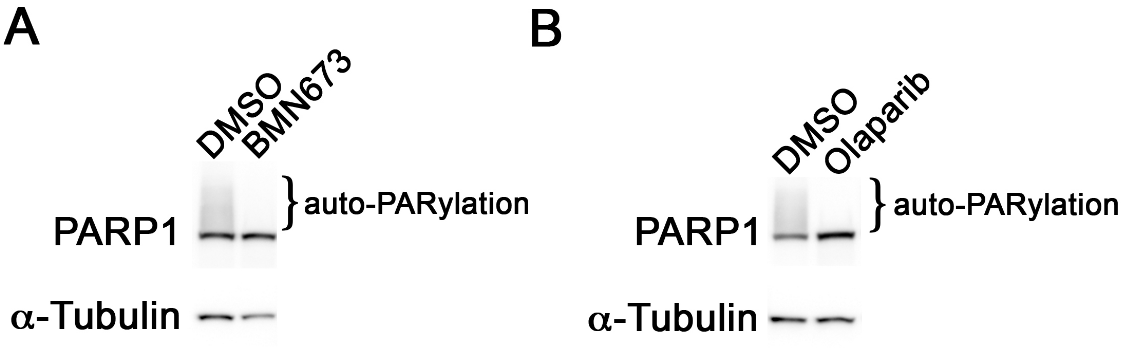

Figure 4.8: BMN673 and Olaparib Treatments Decrease Auto-PARylation
(A) Western blot presenting inhibition of auto-PARylation following BMN673 treatment compared to DMSO control for 48 hours; α-Tubulin is a loading control. The "smear" above the PARP1 band within the DMSO-treated lane is due to PARP1 auto-PARylation, which is dramatically reduced upon BMN673 treatment. ***(B)*** Western blot showing inhibition of auto-PARylation following Olaparib treatment compared to DMSO control treatment for 48 hours; α-Tubulin is a loading control. The "smear" above the PARP1 band within the DMSO-treated lane is due to PARP1 auto-PARylation and is dramatically reduced upon Olaparib treatment.

4.2.3 BMN673 and Olaparib Treatments Induce Proliferation Defects in *RAD54B*-deficient Cells

Having established *RAD54B*-deficient cells are hypersensitive to BMN673 and Olaparib treatments, we next sought to determine the underlying mechanism accounting for the hypersensitivity. Accordingly, cells were treated with BMN673, Olaparib or DMSO and RTCA (i.e. growth curves) were performed to determine whether the SMIs induce either a cell cycle arrest or cellular cytotoxicity. RTCA employs electrical impedance as a measure of cellular proliferation and can easily discern altered growth patterns stemming from cell cycle arrests (i.e. stationary Cell Index [plateau]) or cytotoxicity (i.e. rapid decrease in Cell Index). Figures 4.9A (BMN673) and 4.10A (Olaparib) show that the growth curves generated from the control cells were virtually indistinguishable irrespective of treatment (e.g. BMN673, Olaparib or DMSO), while the proliferation rates as discerned by the slopes during exponential growth (i.e., logarithmic phase) were also very similar. In contrast however, the growth curves generated for the *RAD54B*-deficient cells showed considerable variation following BMN673 and Olaparib treatments compared to controls. For example, BMN673 treatment (Figure 4.9A) induced a rapid decline in cell index ~40 h post-treatment within the *RAD54B*-deficient cells that does not occur following DMSO-treatment, and is indicative of cellular cytotoxicity. In an analogous fashion, Olaparib treatment (Figure 4.10A) reduced proliferation (i.e. decreased the angle of the slope) within the *RAD54B*-deficient cells compared to controls and is suggestive of a proliferation defect. A proliferation defect was calculated for both SMIs at the time point where the *RAD54B*-deficient DMSO-treated growth curves reached their apex, and was ~84 and ~88 h post-seeding for *RAD54B*-deficient cells treated with BMN673 or Olaparib, respectively. BMN673 and Olaparib treatments produced a large proliferation defect within the *RAD54B*-deficient cells that

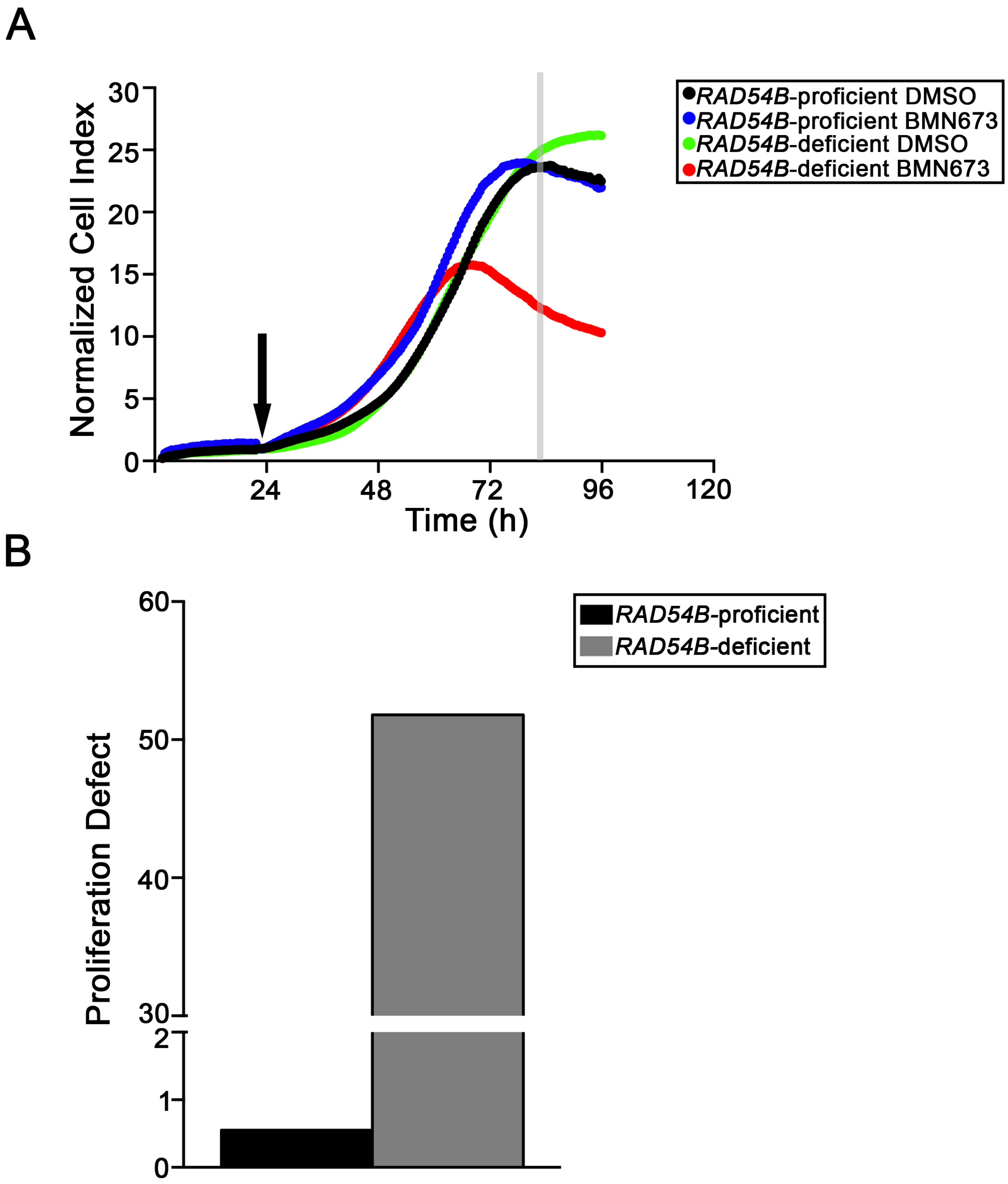

Figure 4.9: BMN673 Treatment Induce Proliferation Defects in *RAD54B*-deficient Cells
(A) RTCA proliferation curves for control and *RAD54B*-deficient cells treated with either BMN673 or DMSO (vehicle control). Arrow identifies the time-point of BMN673 or DMSO addition, while the grey vertical line identifies the time-point employed for calculating the proliferation defect (~84 h post-seeding). ***(B)*** Bar graph depicting the large proliferation defect occurring within the *RAD54B*-deficient cells treated with BMN673 relative to controls. Presented are the results of a single representative experiment. All experiments were performed in quadruplet and repeated one additional time with similar results.

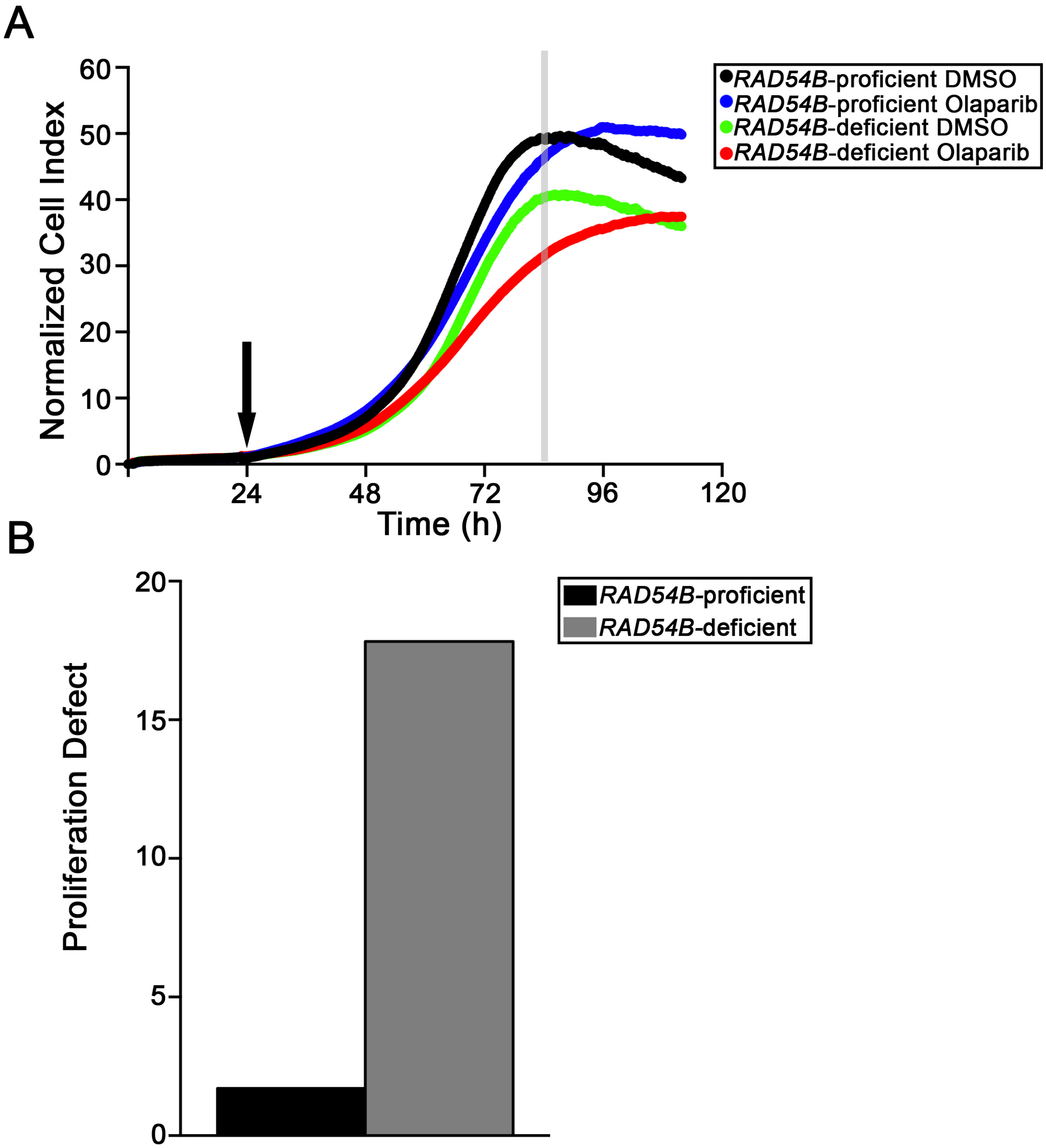

Figure 4.10: Olaparib Treatment Cause Proliferation Defects in *RAD54B*-deficient Cells
(A) RTCA proliferation curves for control and *RAD54B*-deficient cells treated with either Olaparib or DMSO (vehicle control). Arrow identifies the time-point of Olaparib or DMSO addition, while the grey vertical line identifies the time-point employed for calculating the proliferation defect (~88 h post-seeding). ***(B)*** Bar graph depicting the large proliferation defect occurring within the *RAD54B*-deficient cells treated with Olaparib relative to controls. Presented are the results of a single representative experiment. All experiments were performed in quadruplet and repeated one additional time with similar results.

was 94.18- and 10.43-fold greater than their respective controls (Figure 4.9B & 4.10B, Table S6, pg. 117). These data confirm that *RAD54B*-deficient cells are hypersensitive to BMN673 and Olaparib treatments and further suggest that the hypersensitivity is due to an increase in proliferation defects stemming from increased cellular cytotoxicity.

4.2.4 BMN673 and Olaparib Treatments Reduce Cell Confluency of *RAD54B*-deficient Cells in Modified 2D Colony Forming Assays

Prior to evaluating the impact BMN673 and Olaparib treatments have on modified 2D colony formation and growth, it was first necessary to optimize the cell-seeding densities employed in these analyses. The optimal cell seeding density is defined as the density at which clear differences in confluency are observed between the BMN673 or Olaparib treated cells relative to the ~100% confluency observed with the controls (DMSO treated). Briefly, cells were seeded in a 2-fold serial dilution, and treated the following day with BMN673, Olaparib or DMSO control. Following 7 additional days of growth, plates were analyzed and the optimal seeding density was determined to be 1000 cells/well (Figure 4.11).

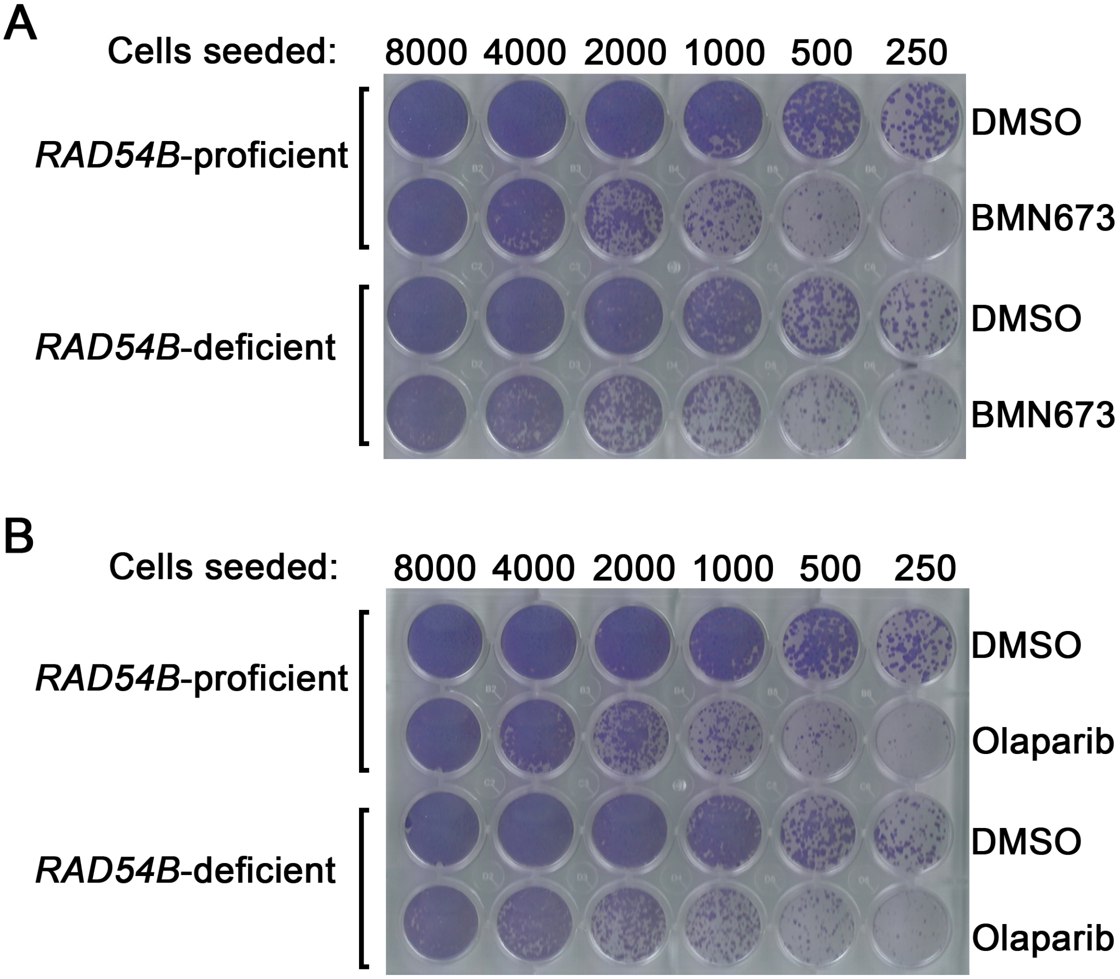

Figure 4.11: Optimization of Cell-Seeding Density for the Modified 2D Colony Forming Assays

Representative images from the optimization of cell-seeding density experiments. A 2-fold serial dilution of *RAD54B*-deficient or control cells were seeded into a 24-well plate and treated with BMN673, Olaparib or DMSO. Cells were stained with crystal violet (purple) to visualize cell confluency. 1000 cells/well was identified as the optimal seeding density as control seeded wells are ~100% confluent.

Having identified the optimal cell seeding density, we now sought to determine whether the hypersensitivity of the *RAD54B*-deficient cells to BMN673 and Olaparib treatments observed in the direct tests detailed above are recapitulated within mCFAs. Accordingly, the percentage of cell confluency relative to DMSO was determined for both the BMN673 and Olaparib treatments and is presented in Figures 4.12 & 4.13, respectively. Following BMN673 and Olaparib treatments a slight decrease in cell confluency was observed within the *RAD54B*-deficient cells compared with controls. The relative cell confluency was 1.88- and 2.56-fold lower in the *RAD54B*-deficient cells treated with BMN673 and Olaparib, respectively (Tables S7 & S8, pgs. 121 & 122). These data are in agreement with those of the direct SL tests performed above and confirm that *RAD54B*-deficient cells are hypersensitive to BMN673 and Olaparib treatments in mCFAs.

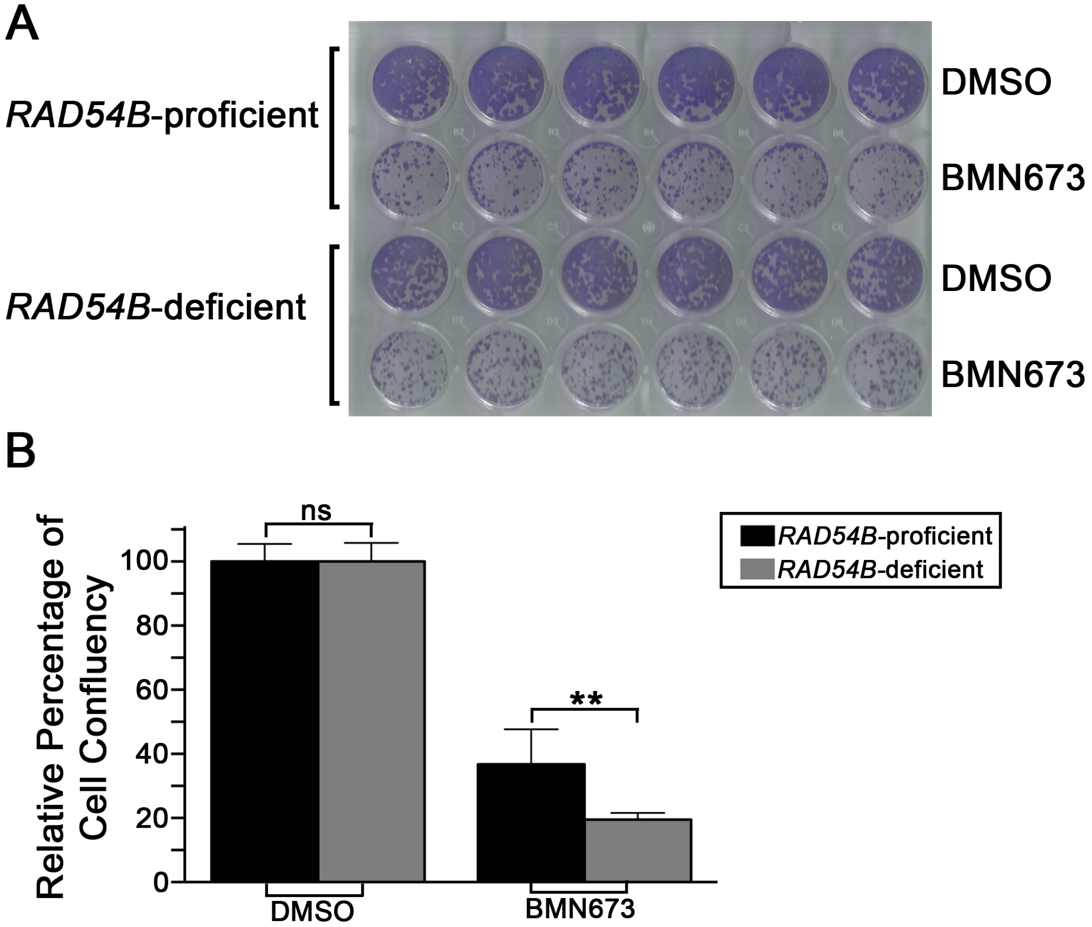

Figure 4.12: BMN673 Treatment Decreases Cell Confluency in *RAD54B*-deficient Cells
(A) Raw image of the modified 2D colony forming assay plate, with *RAD54B*-deficient and control cells treated with DMSO or BMN673. Cells were stained with crystal violet (purple) to visualize confluency. ***(B)*** Bar graph depicting the mean (± SD) relative percentage of cell confluency for *RAD54B*-proficient and *RAD54B*-deficient cells following DMSO (control) or BMN673 treatment. Data are presented normalized to the respective DMSO treated controls. Student's *t*-test reveal statistically significant decreases of *RAD54B*-deficient cell confluency as compared to control cells. (***P*-value <0.01; ns, not significant, n=6). Presented is a single representative example of an experiment performed in sextuplet, with each experiment repeated two additional times with similar findings.

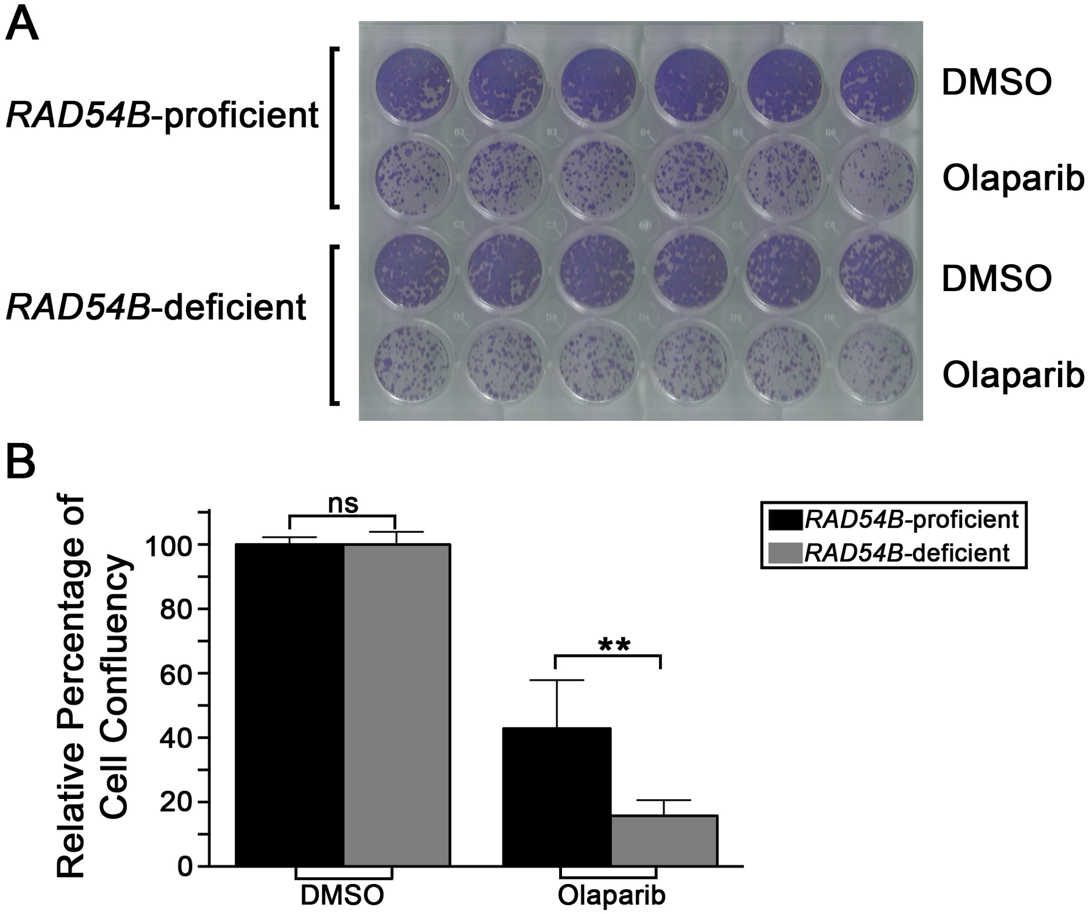

Figure 4.13: Olaparib Treatment Decreases Cell Confluency in *RAD54B*-deficient Cells
(A) Raw image of the modified 2D colony forming assay plate, with *RAD54B*-deficient and control cells treated with DMSO or Olaparib. Cells were stained with crystal violet to visualize confluency. ***(B)*** Bar graph depicting the mean (± SD) relative percentage of cell confluency for *RAD54B*-proficient and *RAD54B*-deficient cells following DMSO (control) or Olaparib treatment. Data are presented normalized to the respective DMSO treated controls. Student's *t*-tests reveal statistically significant decreases in *RAD54B*-deficient cell confluency relative to controls. (***P*-value <0.01; ns, not significant, n=6). Presented is a single representative example of an experiment performed in sextuplet, with each experiment repeated two additional times with similar results.

4.2.5 PARP1 Inhibition Preferentially Induces Increases in γ-H2AX Abundance in *RAD54B*-deficient Cells

Based on the prediction that PARP1 inhibition induces DNA SSBs that are converted into DSBs during replication, we next sought to determine whether there was an increase in DNA DSBs following BMN673 and Olaparib treatments. To accomplish this, we employed semi-quantitative IIF microscopy to evaluate changes in the global abundance (i.e. fluorescence intensity) of γ-H2AX (an established surrogate marker of DNA DSBs[144]) following BMN673 and Olaparib treatments. DNA DSBs induce the phosphorylation of the γ serine residue located within the carboxy-terminal tail of histone H2AX[144], a histone H2A variant. This phosphorylation event occurs rapidly and extensively within H2AX molecules localizing within 2 megabase pairs of either side of the DSB[144]. However, before assessing changes in γ-H2AX abundance, we first confirmed the specificity of the γ-H2AX antibody by evaluating its ability to accurately reflect increases in γ-H2AX abundance that normally occur following IR, which induces DNA DSBs[145]. Semi-quantitative IIF was performed on cells treated with or without IR (Figure 4.14), and as expected, the mean γ-H2AX signal intensities increased ~2.5-times within the IR-treated samples relative to controls. In addition and as expected, the γ-H2AX localization pattern was highly enriched interphase nuclei, and is in agreement with its established localization pattern following IR[144]. Thus, we have confirmed the specificity of the γ-H2AX antibody and established its ability to act as a surrogate maker for DNA DSBs.

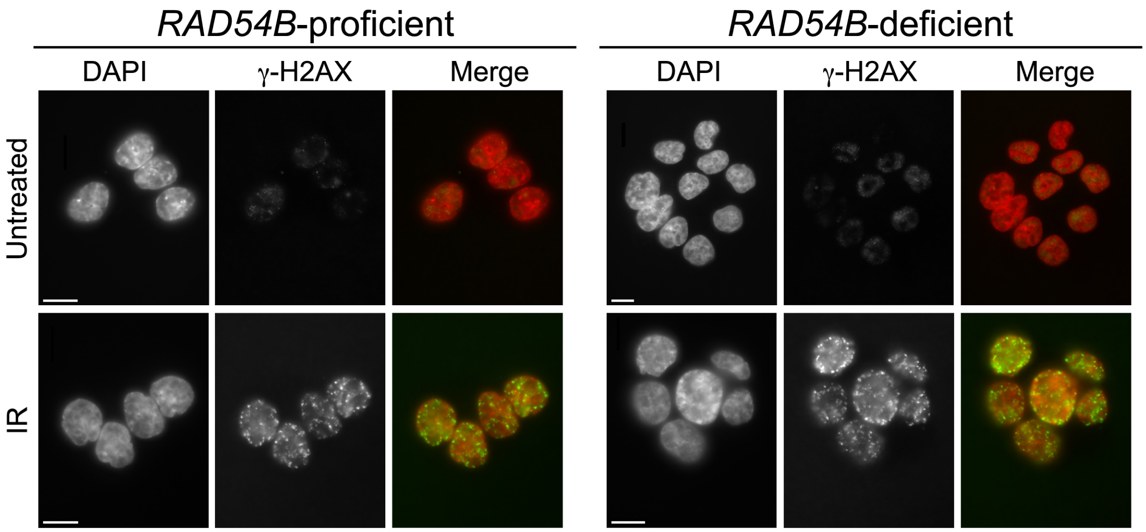

Figure 4.14: Validation of γ-H2AX Antibody to Reflect Increases in DNA Double-Strand Breaks

Representative indirect immunofluorescence images depicting the localization and abundance of γ-H2AX as reflected by increases in intensity within the *RAD54B*-proficient and *RAD54B*-deficient HCT116 cells following IR treatment compared to untreated (non-IR treated) control. Note that identical exposure times were employed for all conditions and thus visual increases in γ-H2AX signal intensities are associated with IR treatment (i.e. DNA DSBs). DAPI and γ-H2AX are pseudo-colored red and green, respectively, within the Merge. (Scale bar = 10μm).

Next, semi-quantitative IIF was performed to determine whether BMN673 and Olaparib treatments induce DNA DSBs preferentially within *RAD54B*-deficient cells that are reflected by increases in the γ-H2AX signal intensities. Figure 4.15 shows the total γ-H2AX signal intensity distributions from a minimum of 175 cells for each condition evaluated. Subsequent Student's *t*-tests show there are statistically significant increases in mean total γ-H2AX signal intensities specifically within the *RAD54B*-deficient cells treated with BMN673 and Olaparib relative to controls that do not occur within either the IR or DMSO treated control conditions (Table S9, pg. 120). In fact, there is a 1.2- and 1.3-fold increase in γ-H2AX signal intensities within the *RAD54B*-deficient cells treated with BMN673 and Olaparib, respectively. Collectively, these data show that the *RAD54B*-deficient cells harbor increases in the global abundance of γ-H2AX following BMN673 and Olaparib treatments suggesting increases in DNA DSBs likely contribute to the hypersensitivity of these cells following PARP1 inhibitor treatments.

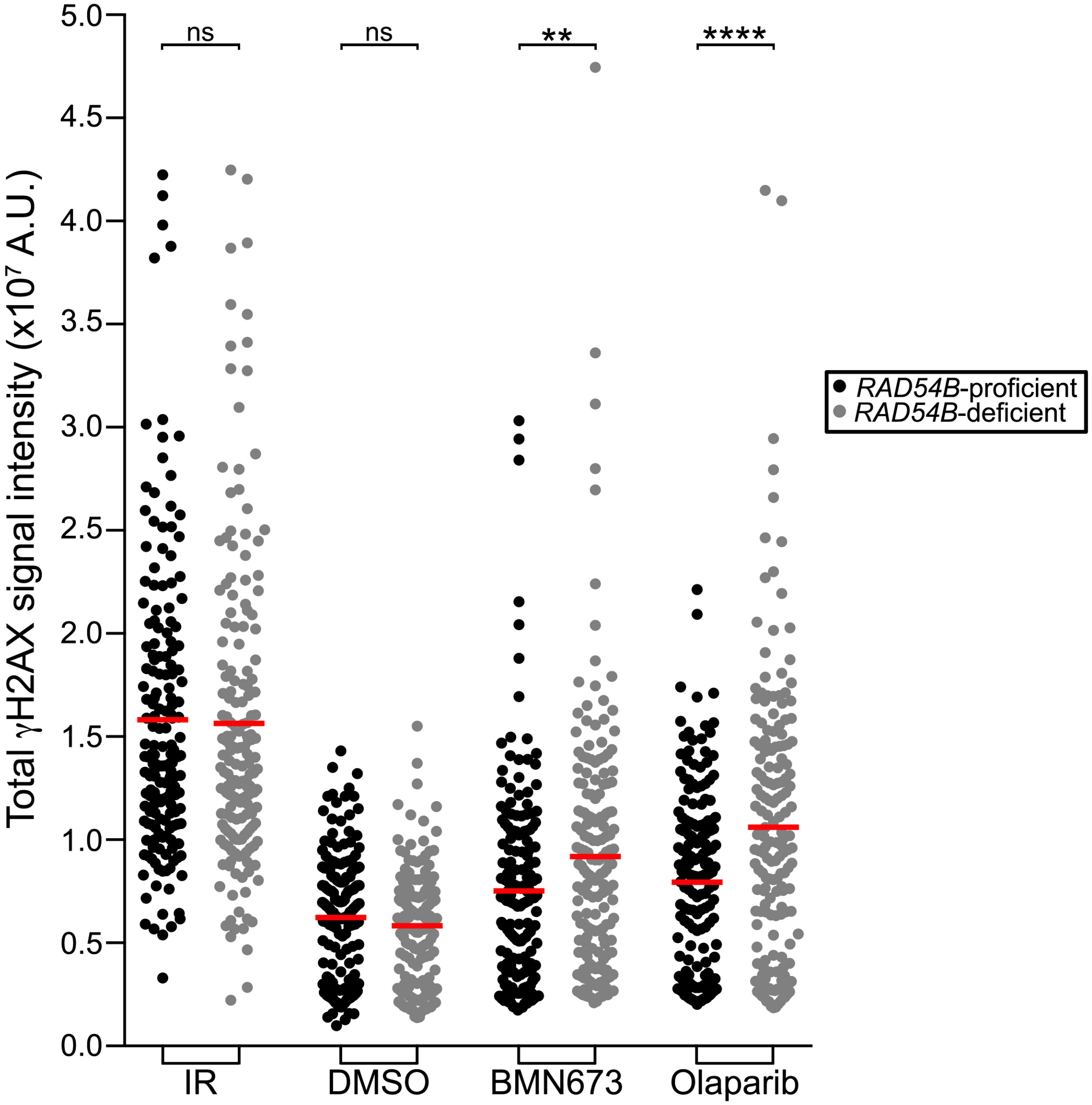

Figure 4.15: γ-H2AX Signal Intensities Increase Preferentially within the *RAD54B*-deficient Cells Following BMN673 and Olaparib Treatments

Scatter plots presenting the total γ-H2AX signal intensities from individual cells treated with IR (positive control), DMSO (negative control), BMN673 or Olaparib as determined by semi-quantitative IIF microscopy. The red bars identify the mean total γ-H2AX signal intensities in each condition. Student's *t*-tests reveal statistically significant increases in γ-H2AX signal intensities in the *RAD54B*-deficient cells treated with BMN673 and Olaparib relative to controls. (*****P*-value <0.0001***P*-value <0.01; ns, not significant, n=175).

4.2.6 PARP1 Inhibition Induces Increases in Apoptosis in *RAD54B*-deficient Cells

Having shown that PARP1 inhibition is associated with a decrease in cell numbers, an increase in proliferation defects, and a corresponding increase in γ-H2AX (i.e. DNA DSBs) within *RAD54B*-deficient cells, we next wished to determine the underlying mechanism accounting for the increase in cell death. As an increase in DNA DSBs is frequently associated with apoptosis[116], so we sought to determine whether BMN673 and Olaparib treatments induce apoptosis preferentially within *RAD54B*-deficient cells. To do so, we employed quantitative IIF microscopy and evaluated the percentage of cells immunofluorescently labeled with an activated/cleaved Caspase-3 antibody, as cleaved Caspase-3 is a well established marker for apoptosis[146].

As with the γ-H2AX antibody, we first wished to validate the specificity of the cleaved Caspase-3 antibody using semi-quantitative IIF in cells treated with Staurosporine (induces apoptosis[147]), or DMSO (vehicle control). Figure 4.16 shows the dramatic increase in cleaved Caspase-3 signal intensity that coincides with staurosporine treatment, which does not occur within the DMSO-treated controls. The cleaved Caspase-3 signal is enriched within the cytoplasm of staurosporine treated cells, which is in agreement with its established cytoplasmic localization pattern[146]. Furthermore, many of the nuclei from the staurosporine treated cells exhibited additional hallmarks of apoptosis including condensed chromatin and nuclear blebbing[148]. Conversely, the DMSO-treated controls failed to show any hallmarks of apoptosis and there was no activated cleaved Caspase-3 signal within the cytoplasm. Collectively, the above data validates the activated cleaved Caspase-3 antibody and the approach to identify apoptotic cells.

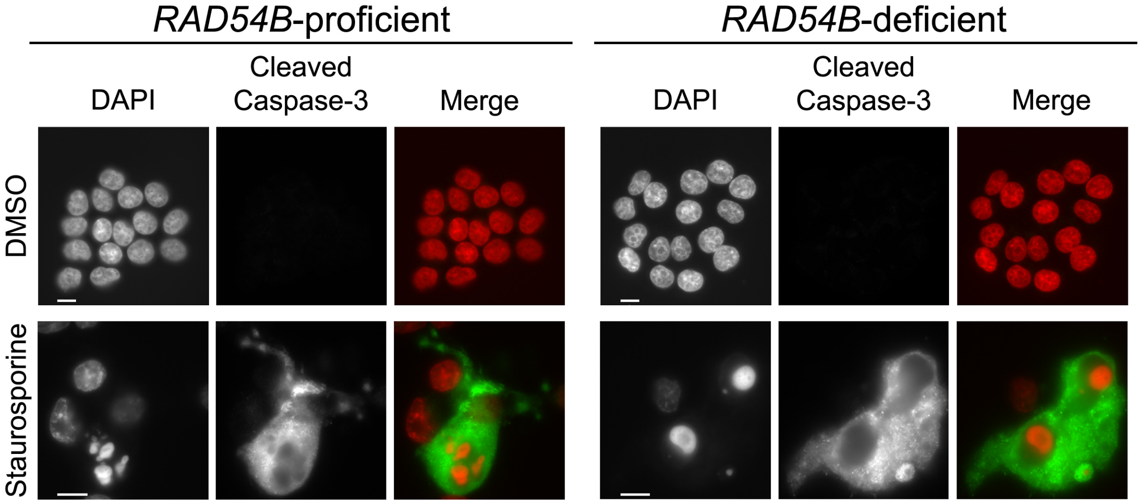

Figure 4.16: Increases in Cleaved Caspase-3 Labeling Following Staurosporine Treatment Representative low-resolution IIF images depicting the localization and relative abundance of cleaved Capase-3 labeling within the *RAD54B*-proficient and *RAD54B*-deficient HCT116 cells treated with staurosporine or DMSO. Note that identical image exposure times were employed for all conditions and that the presence of cleaved Caspase-3 labeling identifies apoptotic cells. DAPI and cleaved Caspase-3 are pseudo-colored red and green, respectively, within the merged image. (Scale bar = 10μm).

To determine whether increases in cleaved Caspase-3 labeling preferentially occur within the *RAD54B*-deficient cells, quantitative IIF microscopy was performed following BMN673, Olaparib or DMSO treatments. A minimum of 500 cells per conditions was evaluated, and the mean number of cells with activated cleaved Caspase-3 (i.e. apoptotic cells) was determined and is presented in Figure 4.17. In general, there was a small increase in the proportion of *RAD54B*-deficient cells labeled with cleaved Caspase-3 following BMN673 and Olaparib treatments relative to controls. More specifically, *RAD54B*-deficient cells exhibited a 1.38- fold (BMN673) and a 3.04-fold (Olaparib) increase in the percentage of apoptotic cells relative to controls that Student's *t*-tests revealed were statistically significant (Table S10, pg. 121). Together, these data show that *RAD54B*-deficient cells treated with BMN673 and Olaparib exhibit increases in the cleaved Caspase-3 labeling relative to controls suggesting apoptosis is preferentially induced within these cells under these conditions.

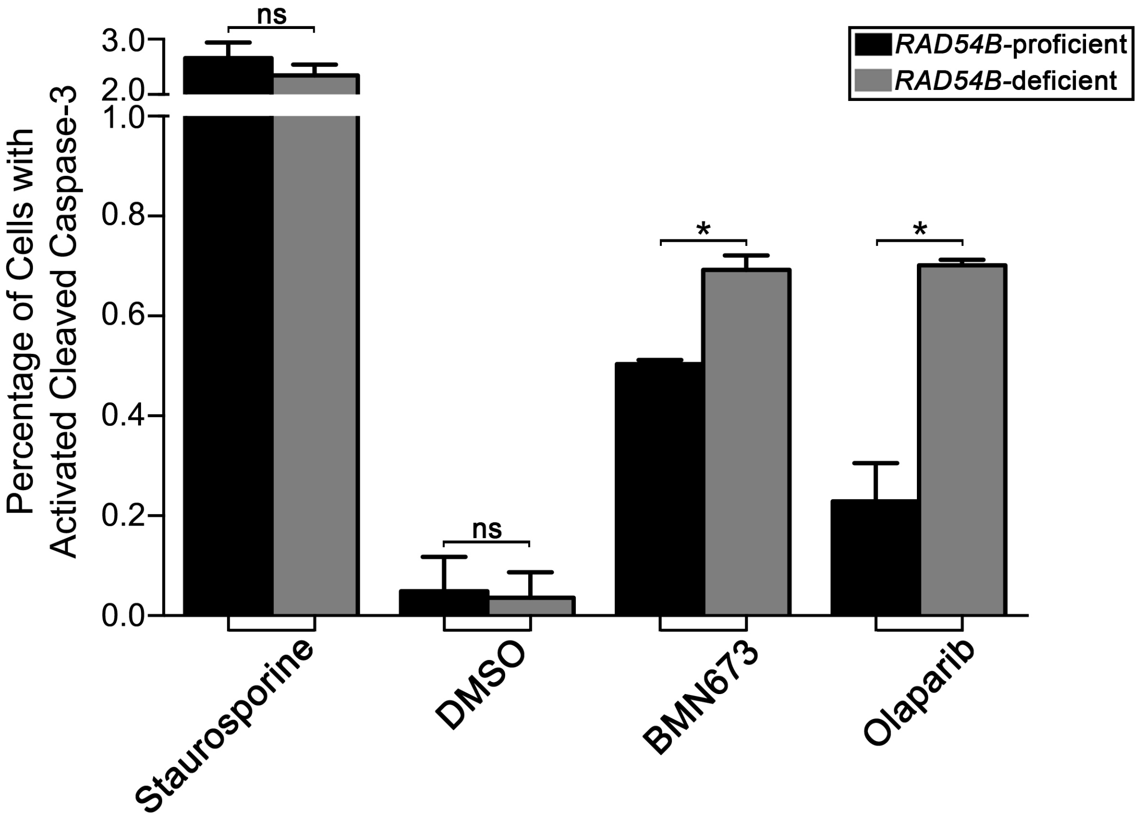

Figure 4.17: BMN673 and Olaparib Treatments Induce Preferential Increases in Cleaved Caspase-3 in *RAD54B*-deficient Cells

Bar graph depicting the mean (±SD) percentage of cells with activated cleaved Caspase-3 as determined by quantitative IIF microscopy. Student's *t*-tests reveal statistically significant increases in the percentage of *RAD54B*-deficient cells labeled with cleaved Caspase-3 when treated with BMN673 or Olaparib compared to controls. (**P*-value <0.05; ns, not significant, N=2).

"

4.2.7 Exploring the Conserved Nature of the *RAD54B PARP1* Synthetic Lethal Interaction

To extend the above findings beyond the HCT116 cellular context employed above, the *RAD54B PARP1* SL interaction was evaluated within a non-malignant hTERT cellular context. hTERT are a karyotypically stable, immortalized (telomerase) fibroblast cell line previously employed in similar SL studies[85,149]. As above, semi-quantitative Western blots (Figures 4.18A & B) were performed and confirmed the silencing efficiency of the pooled siRNAs (si*RAD54B*-Pool and si*PARP1*-Pool) along with the two most efficient individual duplexes for *PARP1* (si*PARP1*-1, -2). Although silencing occurred, it should be noted that it was not to the same extent observed within the HCT116 cells. More specifically, si*RAD54B*-Pool decreased RAD54B expression to ~25% of the control conditions, while si*PARP1*-Pool decreased PARP1 expression to ~26% of controls, with the two most efficient individual duplexes decreasing PARP1 expression to ~17% and 40%, respectively.

Having determined the silencing efficiencies, dual siRNA-based experiments analogous to those presented in Section 4.1.4 (pg. 54) were performed. However, experiments were extended to 4.5 days following silencing to account for the slower hTERT proliferation rate (doubling time of ~36 h for hTERT vs. ~22 h for HCT116) to ensure similar numbers of population doublings. In contrast to the HCT116 findings, the simultaneous silencing of *RAD54B* and *PARP1* within hTERT cells does not appear to induce SL killing (Figure 4.18C). In fact, the percentages of cells remaining following dual silencing were nearly identical to those predicted using the multiplicative model. For example, the observed relative percentage of cells remaining ranged from 89.2-98.2% for the dual silencing conditions (Table S11, pg. 122). These data suggest that the simultaneous silencing of *RAD54B* and *PARP1* does not induce SL killing within hTERT cells under these conditions.

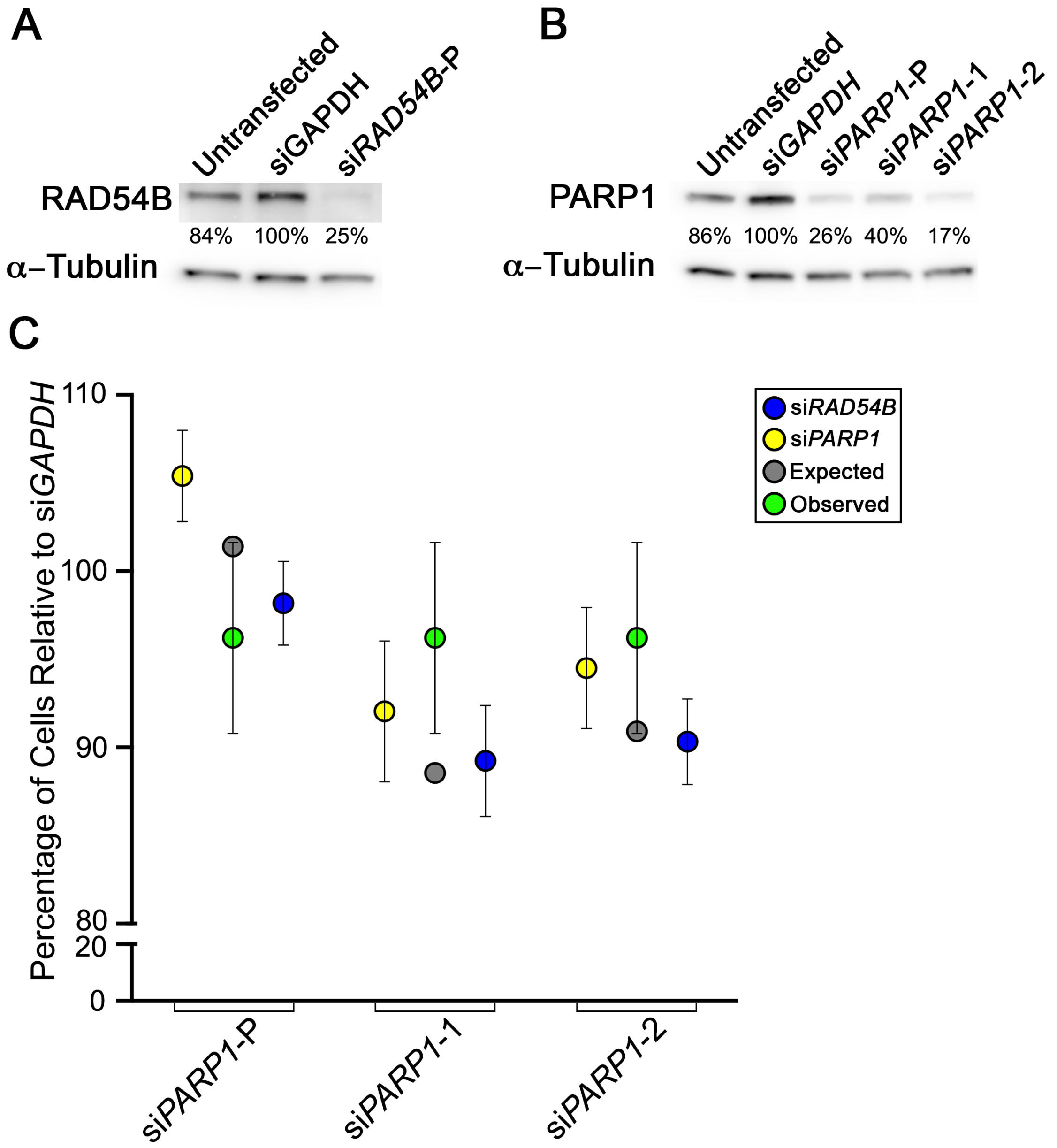

Figure 4.18: Simultaneous Silencing of *RAD54B* and *PARP1* does not Induce SL Killing in hTERT Cells

(A) Western blot depicting diminished RAD54B expression 4.5 days post si*RAD54B*-P transfection relative to controls (Untransfected and si*GAPDH*); α-Tubulin serves as the loading control. The numbers below each lane are the RAD54B expression levels relative to si*GAPDH*. ***(B)*** Western blot depicting diminished PARP1 expression 4.5 days post si*PARP1* transfection relative to controls; α-Tubulin serve as the loading control. The numbers below each lane are the PARP1 expression levels relative to si*GAPDH* ***(C)*** Graphical depiction of the mean normalized percentage of cell remaining (± SD) for the individual silencing of either *RAD54B* (blue circles) or *PARP1* (yellow circles), and the expected value (grey circles) calculated for the dual combined siRNAs using a multiplicative model. Green circles identify the actual observed values for the simultaneous dual silencing (n=6). This experiment was repeated two additional times with similar results.

To explore the *RAD54B PARP1* SL interaction in a second malignant, transformed cellular context, chemogenetic interactions were assessed in HT1080 cells. HT1080 cells are a malignant fibrosarcoma cell line that were purposefully selected as they are karyotypically stable and have a short, ~22 h doubling time (i.e. similar to HCT116). However, rather than performing dual silencing experiments, we sought to determine whether a chemogenetic interaction could be induced by simultaneously silencing *RAD54B* and treatment with PARP1 SMIs. Accordingly, standard dose response curves were generated with slight modifications from those detailed within Section 4.2.1 (pg. 58). Briefly, cells were seeded in 6-well dishes and were transfected 24 h later with si*RAD54B* or si*GAPDH* (control). Following a 24 h incubation period, cells were trypsinized and dispensed into 96-well plates. The following day cells were treated with BMN673, Olaparib or DMSO and permitted to grow for an additional 3 days (Figure 4.19A). As shown in Figure 4.19B, si*RAD54B*-Pool only decreased RAD54B expression to ~68% relative to si*GAPDH* control, 96 h post transfection. Next, dose response curves were performed and produced superimposable curves for both the *RAD54B* silenced and control cells (Figure 4.19C and 4.19D). Collectively, these data suggest that under these conditions, *RAD54B* silenced cells do not appear to be hypersensitive to either BMN673 or Olaparib.

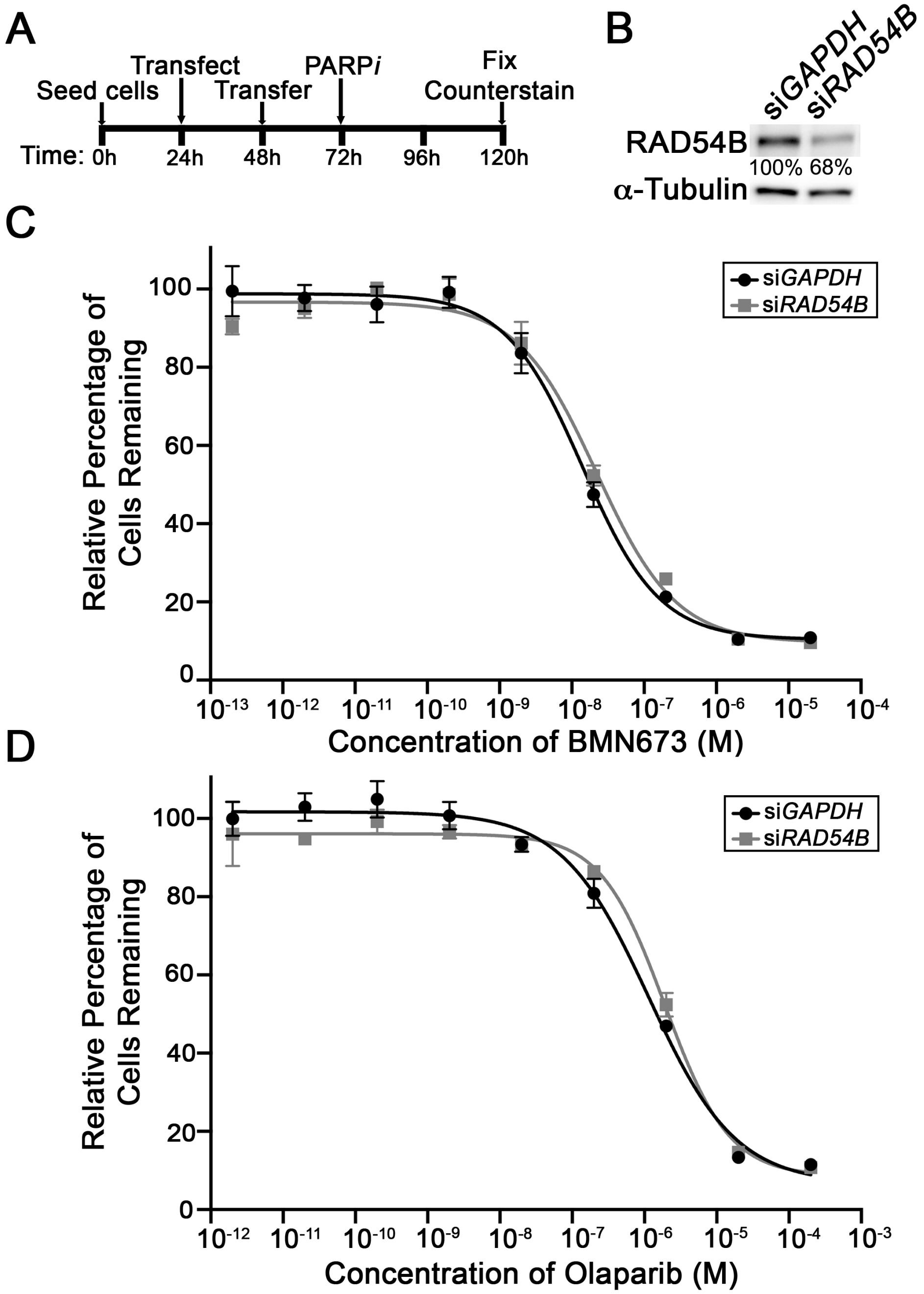

Figure 4.19: PARP1 Inhibition does not Induce SL Killing in *RAD54B*-silenced HT1080 Cells

(A) Timeline employed for experiments in HT1080 cells. (PARP*i* = PARP inhibitor treatment). ***(B)*** Western blot depicting the silencing efficiency of si*RAD54B* in HT1080 cells 4 days post-transfection; α-Tubulin serves as the loading control. Below each lane is the RAD54B expression relative to si*GAPDH*. ***(C)*** Dose response curve for si*GAPDH* (black) and si*RAD54B* (grey) HT1080 cells following BMN673 treatment. Data are normalized to the respective DMSO-treated controls (± SD, n=6). ***(D)*** Dose response curve for si*GAPDH* (black) and si*RAD54B* (grey) HT1080 cells following Olaparib treatment. Data are normalized to the respective DMSO-treated controls (± SD, n=6). These experiments were repeated one additional time with similar results.

CHAPTER 5: CONCLUSIONS AND DISCUSSION

5.1 CONCLUSIONS AND DISCUSSION

To assess the broad-spectrum applicability of PARP1 as candidate drug target we sought to determine the ability of PARP1 silencing and inhibition to exploit *RAD54B* defects in human CRC cells. Using an isogenic *RAD54B* HCT116 model, we demonstrated that PARP1 silencing induces preferential killing within *RAD54B*-deficient cells. We further show that two PARP1 SMIs, BMN673 and Olaparib, also induce preferential killing within *RAD54B*-deficient cells in short- (5 day) and moderate- (8 day) term 2D cell culture assays. We further show that BMN673 and Olaparib treatments induce proliferation defects that are suggestive of increases in cellular cytotoxicity. Finally, we show that BMN673 and Olaparib treatments are associated with increases in the abundance of γ-H2AX and cleaved Caspase 3, strongly suggesting treatments induce increases in DSBs and apoptosis, respectively. Accordingly, data presented within this thesis supports a SL interaction between *RAD54B* and *PARP1* within HCT116 cells, and identifies PARP1 as a novel candidate drug target in CRC cells harboring *RAD54B* defects. As a direct result, these data identify BMN673 and Olaparib as lead candidate SMIs warranting further pre-clinical study (Section 5.3, pg. 93).

The results presented in this thesis show a statistically significant decrease in the number of *RAD54B*-deficient cells following *PARP1* silencing and inhibition. However, the overall strength of the *RAD54B* and *PARP1* SL interaction (i.e. magnitude of killing within the *RAD54B*-deficient cells) was not as robust as other SL interactors identified for either *RAD54B*[4,85] or *PARP1*[113]. For example, *RAD54B*-deficient cells are ~2 or 10-fold more sensitive to FEN1 silencing[4] or SOD1 inhibition[85], respectively compared to controls. Furthermore, *BRCA1/2*-deficient cells are at least ~57-fold more sensitive to PARP1 inhibitors compared to

BRCA1/2-proficient cells[113]. In contrast, this study showed that *RAD54B*-deficient cells were only 1.94- and 1.25-fold more sensitive to BMN673 and Olaparib, respectively, relative to controls. The less pronounced SL interaction observed in this thesis could be due to the peripheral role RAD54B has in HRR, rather than the direct roles associated with BRCA1/2. Recall that RAD54B is a secondary/accessory protein in HRR and thus the loss of *RAD54B* may not be as detrimental to the loss of BRCA1/2. Consequently, *RAD54B*-deficient cells may not be as sensitive to PARP1 inhibitors due to partial or residual HRR activity. In fact, it is possible that the role of RAD54B in HRR may be partially complemented by its closely related paralog, RAD54L. Further studies could be designed to assess this possibility, by determining whether the simultaneous loss of *RAD54B* and *RAD54L* expression enhances the SL killing observed in *RAD54B*-deficient cells alone (detailed in Section 5.3, pg. 93).

5.1.1 The Conserved Nature of *RAD54B PARP1* SL Interaction

The current study identified a small, albeit significant SL interaction between *RAD54B* and *PARP1* within HCT116 cells. However, subsequent direct tests performed in hTERT or HT1080 cells failed to confirm a SL between *RAD54B* and *PARP1* (Section 4.2.7, pg. 79). Although these may be *bona fide* results indicating that *RAD54B* and *PARP1* are not SL in hTERT and HT1080 cells, the possibility exists that certain technical and/or biological issues may have adversely impacted the results. Conceptually, for a SL interaction to occur, the relative expression level of each candidate interactor must be sufficiently silenced, or inhibited below an arbitrary threshold, so that the encoded biological functions are sufficiently impacted so as to induce a SL phenotype. It is possible that within the hTERT and HT1080 cells that RAD54B expression was not sufficiently silenced so as to induce an aberrant phenotype that could be exploited through either PARP1 silencing or BMN673/Olaparib treatment. Indeed, Western blots performed following siRNA silencing show striking differences in the amount of residual protein remaining that are cell line dependent. For example, although *RAD54B* expression was reduced to ~7% of endogenous levels within HCT116 (Figure 4.2, pg. 51), it was only reduced to ~25% and ~68% within hTERT and HT1080 cells, respectively (Figures 4.18A & 4.19B, pgs. 80 & 82). Thus, the limited silencing observed in hTERT and HT1080 may have adversely impacted our ability to detect a SL phenotype. It is also possible that PARP1 silencing or inhibition was not sufficient to induce a SL interaction within the hTERT and HT1080 cells. To formally test this possibility, additional siRNA- or shRNA-based experiments that more efficiently silence RAD54B or PARP1 expression could be employed. Alternatively, a CRISPR-Cas9 based approach could be developed in which either *RAD54B* or *PARP1* is knocked out within hTERT or HT1080 cells. These cells (and proficient controls) could then be employed in similar silencing or inhibition experiments employed within this thesis and the SL interaction would be more efficiently evaluated. Conceptually, the CRISPR-Cas9 approach is the ‘genetically cleanest’ approach to employ as *RAD54B* (or *PARP1*) expression would be completely eliminated and thus only the expression and/or function of PARP1 (or RAD54B) would have to be considered.

A second possibility accounting for the lack of a conserved SL interaction in hTERT and HT1080 cells is the different cellular and genetic contexts of those cells relative to HCT116. Genetic studies performed in model organisms like budding yeast have shown that SL interactions identified in one genetic context are not necessarily conserved in all genetic contexts. More specifically, the different gene expression profiles conferred from different cellular environments may impact or prevent some SL interactions. For example, Harrison *et al*[150] have shown that a subset of SL interactions identified in yeast are dependent on their carbon source (e.g. glucose minimal media vs. glucose rich media [YPD] vs. both media). In fact, only ~14% of SL interactors studied are SL in all media evaluated, while ~50% are SL in one or two carbon sources. Conceptually, the distinct SL interactors identified in the different media are impacted by the altered gene expression profiles that depend on the available carbon source. Undoubtedly, this is a critical concept that will have tremendous implications in treating cancer. Indeed, many groups have shown that the response of cancer cells to certain drug treatments is impacted by genetic context, and alterations in gene expression imparted by somatic gene mutations, copy number variation and epigenetic modifications influence drug efficacies[151]. Accordingly, depending on the genetic context (i.e. gene expression profile), the expression of certain genes may be conducive to SL interactions, while others may act to genetically suppress the interactions. Thus, it is not difficult to envision that certain environmental conditions or biological differences such as tissue type (colon [HCT116] vs. connective tissue [HT1080] vs. fibroblast [hTERT]) or cell type (transformed [HCT116 and HT1080] vs. immortalized [hTERT]) may elicit genetically favorable or unfavorable conditions that would impact our ability to identify a conserved SL interaction between *RAD54B* and *PARP1*.

Finally, it is possible that the HCT116 cells may represent a genetically favorable cellular context that exacerbates or 'primes' the *RAD54B PARP1* SL interaction. Recall that HCT116 are a DNA mismatch repair defective cell line, which stems from an *MLH1*-deficiency. It is conceivable that the *MLH1*-deficiency may synergize with loss of *RAD54B* expression in the context of PARP1 silencing/inhibition to induce a three-way SL phenotype. In contrast, both hTERT and HT1080 are DNA mismatch repair proficient and thus are presumed to be *MLH1*-proficient. For example, hTERT are normal foreskin fibroblasts immortalized through the reintroduction of *TERT* (telomerase), while the Cancer Cell Line Encyclopedia (http://www.broadinstitute.org/ccle/) indicates that HT1080 do not harbor defects in any of the four mismatch repair genes (*MSH2*, *MLH1*, *MSH6* or *PMS2*). Accordingly, to determine whether a DNA mismatch repair defect or *MLH1*-deficiency is required for the *RAD54B PARP1* SL interaction to occur, similar direct tests could be performed in additional CRC cell lines harboring DNA mismatch repair defects, such as HCT-15 (*MSH6*-deficient), SW-48 (*MLH1* promoter methylation), and RKO (*MLH1* promoter methylation)[152].

5.2 EXPANDING THE *PARP1* SL INTERACTION NETWORK

PARP1 inhibition within HRR defective cancers has generated substantial attention since the initial identification of the *BRCA1/2 PARP1* SL interactions[113,114]. Previous studies have shown that members of essential biological pathways, including HRR, frequently share SL interactors[4,85,133]. In fact, several laboratories have identified a number of additional HRR genes that are SL with *PARP1* including *RAD54L*[153], *NBS*[153,154], *RAD51*[153,154], *RAD51C*[153,155], *RAD51D*[153,156], *MRE11A*[157], *XRCC1*[158], *XRCC2*[153], *ATR*[154], *ATM*[154], *DSS1*[154], and *CHEK2*[154], most of which were identified through direct tests[154–157] or high-throughput screens (detailed below)[153,159]. Importantly, the results of this thesis complement these studies, and expand the number of *PARP1* SL interactors to include *RAD54B*.

In 2008, a siRNA screen was employed to determine if knockdown of 233 different DNA repair genes (including *RAD54B*) conferred PARP inhibitor sensitivity, and therefore identify putative SL interactors of *PARP1*[159]. Utilizing a near-diploid breast cancer cell line (CAL51), Lord and colleagues identified five novel genes that following siRNA-based silencing were hypersensitive to KU0058948 (PARP inhibitor), namely *DDB1, LIG1, PCNA, XAB2* and *XRCC1.* Although *RAD54B* was not identified as a candidate SL interactor of KU0058948, it is possible that the screen did not detect it as SL for the reasons presented above (Section 5.1.1, pg.

84). However, because *RAD54B* did not meet the stringent criteria used to identify candidates for subsequent validation experiments, Lord *et al* did not confirm RAD54B knockdown, making it difficult to determine if there was sufficient silencing to induce KU0058948 sensitivity and thus SL killing. An additional possibility accounting for the lack of *RAD54B* being identified as a SL interactor within their study could be accounted for by the different cell lines employed in each study (CAL51 vs. HCT116) or the different PARP1 inhibitor(s) utilized in the studies (KU0058948 vs. BMN673 and Olaparib).

Beyond the chemogenetic (KU0058948) screening results summarized above, additional genome-wide screens have also been conducted to identify further SL interactors of *PARP1*, or more specifically Olaparib[153]. In 2013, Bajrami *et al* performed a genome-wide shRNA library to identify Olaparib sensitivity genes, and thus putative *PARP1* SL interactors[153]. To do so, Bajrami *et al* employed a drop-out screen that requires DNA sequencing and comparison of shRNA barcodes with the population of cells before and after Olaparib treatment. Olaparib sensitivity genes were defined as those that had an underrepresentation of shRNA barcodes following treatment. Conversely, Olaparib resistance genes were defined as those that had an overrepresentation of shRNA barcodes following treatment. Several previously established *PARP1* SL interactors were confirmed in this screen including *BRCA1, RAD51, FANCC*, however two previously identified SL interactors of *PARP1* were not, namely *BRCA2* and *DSS1*[153]. The authors accounted for this obvious discrepancy by indicating inadequate gene silencing occurred, however protein expression was never evaluated. Although *RAD54B* was included in the screen, it was not identified as an Olaparib sensitivity gene. This apparent discrepancy may be due to the factors described above including inefficient RAD54B silencing, differences in the cell lines employed (MCF7 vs. HCT116), or differences in the experimental design and threshold requirement employed to identify the strongest candidate SL interactors. Nevertheless, the complementary silencing and inhibitory data gleaned from this thesis strongly support the existence of a SL interaction between *RAD54B* and *PARP1*, within HCT116 cells.

As the list of *PARP1* SL genes grows, it will become important to curate this data within a comprehensive database with the goal of prioritizing those conserved SL interactions to pursue in subsequent pre-clinical studies, and ultimately in clinical trials. In this regard, the SynLethDB (http://histone.sce.ntu.edu.sg/SynLethDB/) is an online repository that lists SL interactors identified from genetic tests, databases, computational predictions and text mining for humans and various other model systems including yeast, worms, flies and mice[160]. As with any online resource, it will be critical that this database remain accurate, up-to-date, and rapidly integrate the vast amount of SL data published annually.

5.2.1 Clinical Application of *PARP1* SL Interactions in Cancer Treatment

The first clinical application of SL therapeutic approaches utilizing PARP1 inhibitors is now beginning to show promise for breast and ovarian *BRCA1/2* mutated cancers. As discussed within the Introduction (Section 1.4.4, pg. 27), Olaparib is the most clinically advanced PARP1 inhibitor and several clinical trials have demonstrated anti-cancer efficacy within familial breast and ovarian *BRCA1/2* cancers[129,130,161]. Although still early, BMN673 is anticipated to be an even more potent PARP1 inhibitor[127] than Olaparib and is currently in Phase II clinical trials for breast and ovarian cancers with *BRCA1/2* mutations where results are eagerly anticipated.

As the network of *PARP1* SL interactors expands, it will be important to evaluate if cancers harboring HRR defects also respond to PARP1 inhibitors. In fact, there are ongoing and completed clinical trials evaluating PARP1 inhibitors in the context of sporadic cancers with HRR defects outside of *BRCA1/2*. For example, a Phase II trial in patients with metastatic prostate cancer revealed a high response rate (88%) to Olaparib in patients with homozygous deletions or deleterious mutations in DNA repair genes, *ATM, FANCA, CHEK2*[162], supporting the inclusion of patients with these mutations in future studies. However, the sample size of this trial was relatively small (n = 50), and whole exome sequencing did not identify a *RAD54B* mutation in any of the patients. This is not surprising considering only ~0.9% of prostate cancers have a somatic mutation and/or deletion of *RAD54B*[3]. As patient enrollment within clinical trials increases, perhaps those with *RAD54B* mutations and/or deletions can be identified and stratified into PARP1 inhibitor clinical trials. However, this is likely to require much larger sample sizes, as the frequency of *RAD54B* mutations is relatively low in some of these cancer types (Figure 1.4, pg. 16). In any case, and based on the results of this thesis we propose that hypomorphic *RAD54B* expression and/or function may also predict sensitivity to PARP1 inhibitors, though additional pre-clinical studies are needed to further evaluate efficacy of PARP1 inhibitors for *RAD54B*-deficient cancers (Section 5.3, pg. 93).

5.2.2 Therapeutic Considerations of Treatments Involving PARP1 Inhibitors

Along with drug efficacy, drug safety is an important concern when implementing novel compounds for cancer treatment. Clinical trials utilizing Olaparib have reported relatively low side effects such as low to moderate nausea and fatigue[129,130]. However, the consequences of systemic and indiscriminate PARP1 inhibition still remain largely unknown. Identifying and evaluating the potential side-effects of PARP1 inhibition will be critical as PARP1 is a multifunctional protein implicated in a vast array of cellular processes including DNA repair, cell death, transcription, inflammatory response and chromatin remodeling[163].

Since PARP1 modulates BER/SSBR and is now implicated in multiple DNA repair pathways, there is overall concern that new primary cancers may occur following prolonged

PARP1 inhibition as a result of insufficient DNA repair and increased genome instability. Thus far, clinical trials with Olaparib have seen minimal reports of patients developing new primary cancers (<1%)[122]. The new primary cancers developed cannot be confirmed as a consequence of Olaparib treatment, as these patients were heavily pre-treated with other chemotherapies prior to entering the Olaparib clinical trial. In any case, the long-term implications (5+ years) of PARP1 inhibition have yet to be realized as the clinically application of PARP1 inhibitors is relatively new, and long-term follow-up will be important to fully understand the risk of new cancers.

Another concern of systemic PARP1 inhibitor use is the effect(s) inhibitors have on the role PARP1 plays as a modulator of the inflammatory response. Specifically, PARP1 mediates transcriptional activation of the pro-inflammatory factor, NFκB, and the ensuing downstream inflammatory signaling cascade[164,165]. As a direct result, PARP1 inhibition may decrease an inflammatory response that is critical in the body's innate ability to fight off cancer cells, or in more recent targeted approaches that seek to engage the immune response in fighting cancer. This could be especially detrimental for patients who are receiving PARP1 inhibitors as a maintenance therapy over extended periods of time, like in ovarian cancer. Conversely, Swindall and colleagues[166] speculate that PARP1 inhibitors may be useful as a preventative measure for cancers that are linked to chronic inflammation, such as CRC linked to chronic inflammatory bowel disease. In either case, further studies are required to elucidate the impact PARP1 inhibition has on the promotion and prevention of various types of cancer, and it is likely to be cancer-type specific.

Although SL interactions are predicted to be cancer-specific and limit off-target effects, it is likely that the systemic administration of PARP1 SMIs may impact normal cellular functions and tissues. Currently, BMN673 and Olaparib are available in an oral formulation resulting in systemic administration, limited bioavailability, and poor tumour accumulation. To mitigate some of the issues, the generation of superior tumor targeting and delivery modalities would be beneficial. For example, nanoparticle encapsulation and delivery of BMN673 or Olaparib could allow for delivery via injection to provide greater bioavailability and tumour accumulation, while limiting systemic toxicities[167]. PARP1 inhibitors are excellent candidates to develop into nanoparticles to even further restrict the therapeutic effects to the cancer cells.

5.2.3 Combinatorial PARP1 Strategies May Limit Drug Resistance

A major limitation of many cancer therapies is the high risk of disease recurrence following multiple courses with a particular drug that are most often due to primary drug resistance. In this regard, mono-therapies may be initially effective at inhibiting cancer growth, however drug resistance frequently arises after several courses with a particular compound. In general, drug resistance is proposed to arise through two different pathways; 1) acquired resistance, which develops during the course of treatment and in response to therapy employed, or 2) innate resistance, in which a pre-existing drug resistant clone is found within a tumor and is predicted to exist due to the high mutational rate and tumor heterogeneity associated with CIN in cancer cells[168]. Although clinical trials with PARP1 inhibitors are in their still in their infancy, mechanisms of PARP1 inhibitor resistance have been identified. For instance, Olaparib resistance was conferred in *BRCA2*-deficient cancers harboring frame-shift mutations through subsequent mutations that restored the *BRCA2* reading frame to effectively/partially rescue the HRR defect[169]. Thus, a major avenue of scientific inquiry now focuses on identifying and predicting the mechanisms of drug resistance in the hopes of identifying additional drug targets that will prevent the resistance mechanism.

To better combat drug resistance, multi-agent strategies are now being designed and employed as they appear more effective at disease management than mono-therapies[170]. Numerous clinical trials have investigated PARP1 inhibitors in combination with various other agents, including common chemotherapeutics that typically induce DNA damage[122]. For example, a recent Phase II clinical trial involving both Olaparib and carboplatin (an alkylating agent) showed an increase in progression free survival for ovarian cancer patients, particularly within patients harboring *BRCA1/2* mutations[161]. Combinatorial approaches may represent a superior therapeutic strategy for patients with defects in HRR genes that are not as hypersensitive to PARP1 inhibitors as *BRCA1/2* deficient cancers. Accordingly, because limited hypersensitivity to BMN673 and Olaparib occurs in *RAD54B*-deficient cells, combinatorial approaches should be developed to evaluate drug combinations that may produce a synergistic therapeutic effect within those cells. These combinations could include evaluating potential synergy between BMN673/Olaparib and other SL interactors of *RAD54B* including compounds targeting *FEN1, SOD1* and *LIG4*, or those currently employed as front line agents in late state CRC (detailed below).

5.3 FUTURE EXPERIMENTAL DIRECTIONS

The next logical step in the validation of PARP1 as a clinically relevant drug target in *RAD54B*-deficient cancers would be to explore the SL interaction in many additional cellular contexts. However, due to ineffective siRNA-based silencing we observed in hTERT and HT1080 cells, it may be most effective to generate appropriate isogenic *RAD54B* knockout models using a CRISPR-Cas9 approach. Only once the SL interaction has been evaluated in different cellular contexts, will it be possible to discern whether it is a potential and therapeutically relevant SL interaction warranting further investigation.

As indicated above, a combinatorial approach is another avenue that could be pursued in the context of the *RAD54B PARP1* SL interactions. Ideally, optimal drug combinations could be identified that not only enhance the killing observed with either BMN673 or Olaparib alone, but better limit side-effects occurring within normal surrounding cells. Accordingly, it would be informative to evaluate combinations involving previously identified SL interactors of *RAD54B*, such as *FEN1*[4], *SOD1*[85], and *LIG4*[86]. In this regard, combinations involving BMN673/Olaparib with known chemogenetic interactors including RF00974 and NSC645851 (FEN1 inhibitors)[133], LCS-1 or ATTM (SOD1 inhibitors)[171], or SRC7 (LIG4 inhibitor)[172], would be excellent starting points. Alternatively, combining BMN673/Olaparib with conventional CRC chemotherapies, FOLFOX and FOLFIRI, may further exacerbate the inherent vulnerabilities of cancer cells. A major benefit of these combinatorial approaches may be that more cells within a given patient's tumors may be better targeted and eliminated, including the potential pre-existing, drug-resistant clones[173].

As indicated above, an additional possibility accounting for the weak SL interaction observed between *RAD54B* and *PARP1* may be explained by the partial functional redundancy imparted by RAD54L. To test this possibility, additional direct SL tests could be performed within the *RAD54B* isogenic model, where both *RAD54L* and *PARP1* are simultaneously silenced. Furthermore, Streptonigrin, a RAD54L SMI has already been identified[174] and would lend itself nicely to analogous chemogenetic tests involving combinations of Streptonigrin and PARP1 inhibitors within the isogenic *RAD54B* cellular model. In any case, these experiments would help discern whether SL killing of *RAD54B*-deficient cells with PARP1 inhibitors could be exacerbated following *RAD54L* silencing or inhibition.

The development of supplementary and perhaps more physically relevant models over 2D culture systems may help identify strong candidate compounds to pursue in pre-clinical animal model studies. For example, tumor spheroid assays, would be valuable to evaluate BMN673 or Olaparib as single agents within the *RAD54B* isogenic model. Additionally, tumor spheroid assays could be employed to evaluate the combinatorial approaches mentioned above. Eventually, it would be beneficial to migrate the most promising therapeutic approaches identified in cell culture and tumour spheroids assays for *RAD54B*-deficient cells into mouse models. Initially, xenograft mouse models employing subcutaneous injections of the *RAD54B* isogenic cell line could be utilized, particularly because HCT116 cells are known to form tumours in xenograft mice[175]. Bilateral flank injections with either *RAD54B*-proficient or *RAD54B*-deficient cells would allow for easy comparison of tumour regression between cell types after PARP1 inhibitor treatments. However, xenograft flank injection models do no accurately model the microenvironment typically contained within the colon. Thus, the use of a more appropriate model in which the cells are injected/transplanted into the colon of mice would more accurately reflect the physiological microenvironment and inflammatory response of CRC. However, colonic injection mouse models are technically challenging, require special instrumentation and skill to prevent perforation of the colon. Ultimately, patient derived xenograft mouse models would be advantageous and most accurately reflect human CRC as the sample is derived from a patient and not a cell line. If a patient derived sample has an established hypomorphic *RAD54B* mutation, mouse models could be generated using these samples to investigate efficacy of BMN673 or Olaparib. To glean useful information from these models it will be imperative to employ appropriate controls, which are often difficult to obtain in patient-derived studies. Ideally, controls would be derived from normal colon/rectum tissue from the same cancer patient, however it may be difficult to identify truly normal samples. Alternatively, normal tissue could be obtained from the colon/rectum samples from a healthy individual but these tissues would have significant genetic differences.

5.4 PRECISION MEDICINE AND SYNTHETIC LETHALITY – THE FUTURE

In the era of precision medicine, identifying SL interactors may represent superior therapeutic strategies to those currently available. As next generation sequencing costs continue to decrease, it may soon become routine practice to perform whole genome/exome sequencing on patient derived tumors or biopsies to identify genetic susceptibilities that are ideally exploited using a SL paradigm. It may then be possible to identify precision medicine therapies utilizing unique combinations of drugs to selectively kill the cancer cells within the patient. Although a promising therapeutic approach, the clinical application of precision medicine and synthetic lethality are still in their infancy. Expanding the *PARP1* and *RAD54B* SL networks is just one avenue to further advance the SL targeting field. Additional efforts to identify SL interactions within many other biological pathways that are frequently altered in cancer are also needed. For example, identifying SL interactors with *TP53* is of great interest due to its high mutation rate in all cancers[176]. Information detailed in this thesis and multiple pre-clinical and clinical studies strongly suggest that using SL targeting approaches to selectively kill cancer cells may be a highly effective precision medicine therapeutic strategy that may hold tremendous potential.

CHAPTER 6: REFERENCES

1. Canadian Cancer Society. *Canadian Cancer Statistics Special topic: Predictions of the future burden of cancer in Canada*. *Public Health Agency of Canada* (2015).
2. American Cancer Society. *American Cancer Society: Cancer Facts and Figures 2015*. (2015). doi:10.3322/caac.21254
3. Cerami, E. *et al.* The cBio cancer genomics portal: an open platform for exploring multidimensional cancer genomics data. *Cancer Discov.* **2,** 401–4 (2012).
4. McManus, K. J., Barrett, I. J., Nouhi, Y. & Hieter, P. Specific synthetic lethal killing of RAD54B-deficient human colorectal cancer cells by FEN1 silencing. *Proc. Natl. Acad. Sci. U. S. A.* **106,** 3276–3281 (2009).
5. Brenner, H., Kloor, M. & Pox, C. P. Colorectal cancer. *Lancet* **383,** 1490–1502 (2014).
6. Markowitz, S. D. & Bertagnolli, M. M. Molecular Origins of Cancer: Molecular Basis of Colorectal Cancer. *N. Engl. J. Med.* **361,** 2449–2460 (2009).
7. Society, C. C. Canadian Cancer Statistics 2011 Special topic: Colorectal cancer. *Can. Cancer Soc. Toronto,* (2011).
8. Cremolini, C. *et al.* First-line chemotherapy for mCRC—a review and evidence-based algorithm. *Nat. Rev. Clin. Oncol.* **12,** 607–619 (2015).
9. Longley, D., Harkin, D. & Johnston, P. 5-Fluorouracil: Mechanisms of Action and Clinical Strategies. *Nat. Rev. Cancer* **3,** 330–338 (2003).
10. Mini, E., Trave, F., Rustum, Y. M. & Bertino, J. R. Enhancement of the antitumor effects of 5-fluorouracil by folinic acid. *Pharmac. Ther.* **47,** 1–19 (1990).
11. Faivre, S., Chan, D., Salinas, R., Woynarowska, B. & Woynarowski, J. M. DNA strand breaks and apoptosis induced by oxaliplatin in cancer cells. *Biochem. Pharmacol.* **66,** 225–237 (2003).
12. Gilbert, D. C., Chalmers, a. J. & El-Khamisy, S. F. Topoisomerase I inhibition in colorectal cancer: biomarkers and therapeutic targets. *Br. J. Cancer* **106,** 18–24 (2012).
13. Lengauer, C., Kinzler, K. W., Vogelstein, B. Genetic instability in colorectal cancers. 623 – 627 (1997).
14. Rajagopalan, H., Nowak, M. a, Vogelstein, B. & Lengauer, C. The significance of unstable chromosomes in colorectal cancer. *Nat. Rev. Cancer* **3,** 695–701 (2003).
15. Vogelstein, B. *et al.* Cancer Genome Landscapes. *Science (80-.).* **339,** 1546–1558 (2013).
16. Hanahan, D. & Weinberg, R. a. Hallmarks of cancer: the next generation. *Cell* **144,** 646–74 (2011).
17. Wahlberg, S. S. *et al.* Evaluation of microsatellite instability and immunohistochemistry for the prediction of germ-line MSH2 and MLH1 mutations in hereditary nonpolyposis colon cancer families. *Cancer Res.* **62,** 3485–3492 (2002).
18. Loeb, L. a. Mutator phenotype may be required for multistage carcinogenesis. *Cancer Res.* **51,** 3075–3079 (1991).
19. Loeb, L. a. A mutator phenotype in cancer. *Cancer Res.* **61,** 3230–3239 (2001).
20. Loeb, L. a., Bielas, J. H. & Beckman, R. a. Cancers exhibit a mutator phenotype: Clinical implications. *Cancer Res.* **68,** 3551–3557 (2008).
21. Gazzoli, I., Loda, M., Garber, J., Syngal, S. & Kolodner, R. D. A Hereditary Nonpolyposis Colorectal Carcinoma Case Associated with Hypermethylation of the MLH1 Gene in Normal Tissue and Loss of Heterozygosity of the Unmethylated Allele in the Resulting Microsatellite Instability-High Tumor. *Cancer Res.* **62,** 3925–3928 (2002).

22. Boyer, J., Umar, A., Risinger, J. & Lipford, J. Microsatellite Instability, Mismatch Repair Deficiency, and Genetic Defects in Human Cancer Cell Lines. *Cancer Res.* **55,** 6063–6070 (1995).
23. Issa, J.-P. CpG island methylator phenotype in Cancer. *Nat. Rev. Cancer* **4,** 988–993 (2004).
24. Jeong, M. B., Kim, J. H. & Kang, G. H. Epigenetic alterations in colorectal cancer: The CpG island methylator phenotype. *Histol. Histopathol.* **28,** 585–595 (2013).
25. Baylin, S. B. & Jones, P. a. A decade of exploring the cancer epigenome — biological and translational implications. *Nat. Rev. Cancer* **11,** 726–734 (2011).
26. Feinberg, A. P. & Tycko, B. The history of cancer epigenetics. *Nat. Rev. Cancer* **4,** 143–153 (2004).
27. Lengauer, C., Kinzler, K. W. & Vogelstein, B. Genetic instabilities in human cancers. *Nature* **396,** 643–649 (1998).
28. Beheshti, B. *et al.* Evidence of Chromosomal Instability in Prostate Cancer Determined by Spectral Karyotyping (SKY) and Interphase FISH Analysis1. *Neoplasia* **3,** 62–69 (2001).
29. Burrell, R. a *et al.* Replication stress links structural and numerical cancer chromosomal instability. *Nature* **494,** 492–6 (2013).
30. Mai, S. *et al.* Chromosomal and extrachromosomal instability of the cyclin D2 gene is induced by Myc overexpression. *Neoplasia* **1,** 241–252 (1999).
31. Lingle, W. L. *et al.* Centrosome amplification drives chromosomal instability in breast tumor development. *Proc. Natl. Acad. Sci. U. S. A.* **99,** 1978–83 (2002).
32. Sajesh, B. V, Lichtensztejn, Z. & McManus, K. J. Sister chromatid cohesion defects are associated with chromosome instability in Hodgkin lymphoma cells. *BMC Cancer* **13,** 391 (2013).
33. Komarova, N. L., Lengauer, C., Vogelstein, B. & Nowak, M. a. Dynamics of genetic instability in sporadic and familial colorectal cancer. *Cancer Biol. Ther.* **1,** 685–692 (2002).
34. Gordon, D. J., Resio, B. & Pellman, D. Causes and consequences of aneuploidy in cancer. *Nat. Rev. Genet.* **13,** 189–203 (2012).
35. Heilig, C. E. *et al.* Chromosomal instability correlates with poor outcome in patients with myelodysplastic syndromes irrespectively of the cytogenetic risk group. *J. Cell. Mol. Med.* **14,** 895–902 (2010).
36. Lee, A. J. X. *et al.* Chromosomal instability confers intrinsic multidrug resistance. *Cancer Res.* **71,** 1858–1870 (2011).
37. Tanaka, K., Kagawa, W., Kinebuchi, T., Kurumizaka, H. & Miyagawa, K. Human Rad54B is a double-stranded DNA-dependent ATPase and has biochemical properties different from its structural homolog in yeast, Tid1/Rdh54. *Nucleic Acids Res.* **30,** 1346–1353 (2002).
38. Arbel, A., Zenvirth, D. & Simchen, G. Sister chromatid-based DNA repair is mediated by RAD54, not by DMC1 or TID1. *EMBO J.* **18,** 2648–2658 (1999).
39. Klein, H. L. RDH54, a RAD54 Homologue in Saccharomyces cerevisiae, Is Required for Mitotic Diploid-Specific Recombination and Repair and for Meiosis. *Genetics* **147,** 1533–1543 (1997).
40. Shinohara, M. *et al.* Characterization of the Roles of the Saccharomyces cerevisiae RAD54 Gene and a Homologue of RAD54, RDH54/TID1, in Mitosis and Meiosis. *Genetics* **147,** 1545–1556 (1997).

41. Hiramoto, T. *et al.* Mutations of a novel human RAD54 homologue, RAD54B, in primary cancer. *Oncogene* **18,** 3422–3426 (1999).
42. Marchler-Bauer, A. *et al.* CDD: NCBI's conserved domain database. *Nucleic Acids Res.* **43,** D222–D226 (2015).
43. Smith, C. L. & Peterson, C. L. A Conserved Swi2 / Snf2 ATPase Motif Couples ATP Hydrolysis to Chromatin Remodeling. *Mol. Cell. Biol.* **25,** 5880–5892 (2005).
44. Pazin, M. J. & Kadonaga, J. T. SWI2/SNF2 and Related Proteins: ATP-Driven Motors That Disrupt-Protein–DNA Interactions? *Cell* **88,** 737–740 (1997).
45. Heyer, W. D., Li, X., Rolfsmeier, M. & Zhang, X. P. Rad54: The Swiss Army knife of homologous recombination? *Nucleic Acids Res.* **34,** 4115–4125 (2006).
46. Jackson, S. P. Sensing and repairing DNA double-strand breaks. *Carcinogenesis* **23,** 687–696 (2002).
47. Li, X. & Heyer, W.-D. Homologous recombination in DNA repair and DNA damage tolerance. *Cell Res.* **18,** 99–113 (2008).
48. Symington, L. S. Role of RAD52 Epistasis Group Genes in Homologous Recombination and Double-Strand Break Repair. *Microbiol. Mol. Biol. Rev.* **66,** 630–670 (2002).
49. Miyagawa, K. *et al.* A role for RAD54B in homologous recombination in human cells. *EMBO J.* **21,** 175–80 (2002).
50. Murzik, U. *et al.* RAD54B Targeting to DNA Double-Strand Break Repair Sites Requires Complex Formation with S100A11. *Mol. Biol. Cell* **19,** 2926–2935 (2008).
51. Wesoly, J. *et al.* Differential contributions of mammalian Rad54 paralogs to recombination, DNA damage repair, and meiosis. *Mol. Cell. Biol.* **26,** 976–989 (2006).
52. Tanaka, K., Hiramoto, T., Fukuda, T. & Miyagawa, K. A novel human Rad54 homologue, Rad54B, associates with Rad51. *J. Biol. Chem.* **275,** 26316–26321 (2000).
53. Otterlei, M. *et al.* Werner syndrome protein participates in a complex with RAD51, RAD54, RAD54B and ATR in response to ICL-induced replication arrest. *J. Cell Sci.* **119,** 5137–5146 (2006).
54. Su, A. I. *et al.* A gene atlas of the mouse and human protein-encoding transcriptomes. *Proc. Natl. Acad. Sci. U. S. A.* **101,** 6062–7 (2004).
55. Wu, C., Jin, X., Tsueng, G., Afrasiabi, C. & Su, A. I. BioGPS: building your own mash-up of gene annotations and expression profiles. *Nucleic Acids Res* **44,** D313–6 (2016).
56. Yuen, K. W. Y. *et al.* Systematic genome instability screens in yeast and their potential relevance to cancer. *Proc. Natl. Acad. Sci. U. S. A.* **104,** 3925–3930 (2007).
57. Krauthammer, M. *et al.* Exome sequencing identifies recurrent somatic RAC1 mutations in melanoma. *Nat. Genet.* **44,** 1006–1014 (2012).
58. The Cancer Genome Atlas Network. Integrated genomic characterization of endometrial carcinoma. *Nature* **497,** 67–73 (2013).
59. Seshagiri, S. *et al.* Recurrent R-spondin fusions in colon cancer. *Nature* **488,** 660–664 (2012).
60. Eirew, P. *et al.* Dynamics of genomic clones in breast cancer patient xenografts at single-cell resolution. *Nature* **518,** 422–426 (2015).
61. Hodis, E. *et al.* A Landscape of Driver Mutations in Melanoma. 251–263 (2012). doi:10.1016/j.cell.2012.06.024
62. The Cancer Genome Atlas Network. Comprehensive molecular portraits of human breast tumours. *Nature* **490,** 61–70 (2012).
63. Bass, A. J. *et al.* Comprehensive molecular characterization of gastric adenocarcinoma.

Nature **513,** 202–209 (2014).
64. Imielinski, M. *et al.* Mapping the Hallmarks of Lung Adenocarcinoma with Massively Parallel Sequencing. *Cell* **150,** 1107–1120 (2012).
65. The Cancer Genome Atlas Network. Comprehensive molecular characterization of human colon and rectal cancer. *Nature* **487,** 330–337 (2012).
66. The Cancer Genome Atlas Research Network. Comprehensive molecular characterization of urothelial bladder carcinoma. *Nature* **507,** 315–322 (2014).
67. The Cancer Genome Atlas Research Network. Comprehensive molecular profiling of lung adenocarcinoma. *Nature* **511,** 543–550 (2014).
68. Barbieri, C. E. *et al.* Exome sequencing identifies recurrent SPOP, FOXA1 and MED12 mutations in prostate cancer. *Nat. Genet.* **44,** 685–689 (2012).
69. Guo, G. *et al.* Whole-genome and whole-exome sequencing of bladder cancer identifies frequent alterations in genes involved in sister chromatid cohesion and segregation. *Nat. Genet.* **45,** 1459–63 (2013).
70. Dulak, A. M. *et al.* Exome and whole-genome sequencing of esophageal adenocarcinoma identifies recurrent driver events and mutational complexity. *Nat. Genet.* **45,** 478–486 (2013).
71. Brennan, C. W. *et al.* The Somatic Genomic Landscape of Glioblastoma. *Cell* **155,** 462–477 (2013).
72. Ciriello, G. *et al.* Comprehensive Molecular Portraits of Invasive Lobular Breast Cancer. *Cell* **163,** 506–519 (2015).
73. Rhodes, D. R. *et al.* Oncomine 3.0: genes, pathways, and networks in a collection of 18,000 cancer gene expression profiles. *Neoplasia* **9,** 166–180 (2007).
74. Reva, B., Antipin, Y. & Sander, C. Predicting the functional impact of protein mutations: application to cancer genomics. *Nucleic Acids Res.* **39,** e118–e118 (2011).
75. Adzhubei, I. a *et al.* A method and server for predicting damaging missense mutations. *Nat. Methods* **7,** 248–249 (2010).
76. Kumar, P., Henikoff, S. & Ng, P. C. Predicting the effects of coding non-synonymous variants on protein function using the SIFT algorithm. *Nat. Protoc.* **4,** 1073–1081 (2009).
77. Pearl, L. H., Schierz, A. C., Ward, S. E., Al-lazikani, B. & Pearl, F. M. G. Therapeutic opportunities within the DNA damage response. *Nat. Rev. Cancer* **15,** 166–180 (2015).
78. Vogelstein, B. *et al.* Cancer Genome Lanscapes. *Science (80-.).* **339,** 1546–1558 (2013).
79. Bhuvanagiri, M., Schlitter, A. M., Hentze, M. W. & Kulozik, A. E. NMD: RNA biology meets human genetic medicine. *Biochem. J.* **430,** 365–77 (2010).
80. Naidu, M. U. R. *et al.* Chemotherapy-induced and/or radiation therapy-induced oral mucositis--complicating the treatment of cancer. *Neoplasia* **6,** 423–431 (2004).
81. Sajesh, B. V, Guppy, B. J. & McManus, K. J. Synthetic genetic targeting of genome instability in cancer. *Cancers (Basel).* **5,** 739–61 (2013).
82. Sajesh, B. V., Cisyk, A. L. & McManus, K. J. in *Genomic Instability and Cancer Metastasis* 179–204 (2015).
83. Dobzhansky, T. Genetics of Natural Populations. Xiii. Recombination and Variability in Populations of Drosophila Pseudoobscura. *Genetics* **31,** 269–290 (1946).
84. Hartwell, L. H., Szankasi, P., Roberts, C. J., Murray, A. W. & Friend, S. H. Integrating Genetic Approaches into the Discovery of Anticancer Drugs. *Science (80-.).* **278,** 1064–1068 (1997).
85. Sajesh, B. V., Bailey, M., Lichtensztejn, Z., Hieter, P. & McManus, K. J. Synthetic lethal

targeting of superoxide dismutase 1 selectively kills RAD54B-deficient colorectal cancer cells. *Genetics* **195,** 757–767 (2013).

86. Oh, S., Wang, Y., Zimbric, J. & Hendrickson, E. a. Human LIGIV is synthetically lethal with the loss of Rad54B-dependent recombination and is required for certain chromosome fusion events induced by telomere dysfunction. *Nucleic Acids Res.* **41,** 1734–1749 (2013).
87. Liu, Y., Kao, H.-I. & Bambara, R. a. Flap endonuclease 1: a central component of DNA metabolism. *Annu. Rev. Biochem.* **73,** 589–615 (2004).
88. Waris, G. & Ahsan, H. Reactive oxygen species: role in the development of cancer and various chronic conditions. *J. Carcinog.* **5,** 14 (2006).
89. Abreu, I. a. & Cabelli, D. E. Superoxide dismutases-a review of the metal-associated mechanistic variations. *Biochim. Biophys. Acta - Proteins Proteomics* **1804,** 263–274 (2010).
90. Chambon, P., Weill, J. D. & Mandel, P. Nicotinamide mononucleotide activation of a new DNA-dependent polyadenylic acid synthesizing nuclear enzyme. *Biochem. Biophys. Res. Commun.* **11,** 39–43 (1963).
91. Chambon, P., Weill, J. D., Doly, J., Strosser, M. T. & Mandel, P. On the formation of a novel adenylic compound by enzymatic extracts of liver nuclei. *Biochem. Biophys. Res. Commun.* **25,** 638–643 (1966).
92. Okayama, H., Edson, C. M., Fukushima, M., Ueda, K. & Hayaishi, O. Purification and properties of Poly(Adenosine disphosphate ribose) synthetase. *J. Biol. Chem.* **252,** 7000–7005 (1977).
93. Uchida, K. *et al.* Nucleotide sequence of a full-length cDNA for human fibroblast poly(ADP-ribose) polymerase. *Biochem. Biophys. Res. Commun.* **148,** 617–622 (1987).
94. Schreiber, V., Dantzer, F., Ame, J.-C. & de Murcia, G. Poly(ADP-ribose): novel functions for an old molecule. *Nat. Rev. Mol. Cell Biol.* **7,** 517–528 (2006).
95. Rouleau, M., Patel, A., Hendzel, M. J., Kaufmann, S. H. & Poirier, G. G. PARP inhibition: PARP1 and beyond. *Nat. Rev. Cancer* **10,** 293–301 (2010).
96. Amé, J. C., Spenlehauer, C. & De Murcia, G. The PARP superfamily. *BioEssays* **26,** 882–893 (2004).
97. Kraus, W. L. PARPs and ADP-Ribosylation: 50 Years . . . and Counting. *Mol. Cell* **58,** 902–910 (2015).
98. Bai, P. & Cantó, C. The role of PARP-1 and PARP-2 enzymes in metabolic regulation and disease. *Cell Metab.* **16,** 290–295 (2012).
99. Durkacz, B. W., Omidiji, O., Gray, D. A. & Shall, S. (ADP-ribose)n participates in DNA excision repair. *Nature* **283,** 593–596 (1980).
100. Dantzer, F. *et al.* Base excision repair is impaired in mammalian cells lacking Poly (ADP-ribose) polymerase-1. *Biochemistry* **39,** 7559–7569 (2000).
101. De Vos, M., Schreiber, V. & Dantzer, F. The diverse roles and clinical relevance of PARPs in DNA damage repair: current state of the art. *Biochem. Pharmacol.* **84,** 137–46 (2012).
102. Schreiber, R. I. E., Muller, S., Masson, M. & Niedergang, C. XRCC1 Is Specifically Associated with Poly (ADP-Ribose) Polymerase and Negatively Regulates Its Activity following DNA Damage. **18,** 3563–3571 (1998).
103. Eustermann, S. *et al.* Structural Basis of Detection and Signaling of DNA Single-Strand Breaks by Human PARP-1. *Mol. Cell* **60,** 742–754 (2015).
104. Bryant, H. E. *et al.* PARP is activated at stalled forks to mediate Mre11-dependent

replication restart and recombination. *EMBO J.* **28,** 2601–2615 (2009).

105. Haince, J. F. *et al.* Ataxia telangiectasia mutated (ATM) signaling network is modulated by a novel poly(ADP-ribose)-dependent pathway in the early response to DNA-damaging agents. *J. Biol. Chem.* **282,** 16441–16453 (2007).
106. Ruscetti, T. *et al.* Stimulation of the DNA-dependent Protein Kinase by Poly (ADP-Ribose) Polymerase *. **273,** 14461–14467 (1998).
107. Wang, M. *et al.* PARP-1 and Ku compete for repair of DNA double strand breaks by distinct NHEJ pathways. *Nucleic Acids Res.* **34,** 6170–6182 (2006).
108. Robu, M. *et al.* Role of poly (ADP-ribose) polymerase-1 in the removal of UV-induced DNA lesions by nucleotide excision repair. 1–6 (2013). doi:10.1073/pnas.1209507110/-/DCSupplemental.www.pnas.org/cgi/doi/10.1073/pnas.1209507110
109. Ali, A. a E. *et al.* The zinc-finger domains of PARP1 cooperate to recognize DNA strand breaks. *Nat. Struct. Mol. Biol.* **19,** 685–692 (2012).
110. de Murcia, G. & de Murcia, J. Poly(ADP-ribose) polymerase: a molecular nick-sensor. *Trends Biochem. Sci.* **19,** 172–176 (1994).
111. D'Amours, D., Desnoyers, S., D'Silva, I. & Poirier, G. G. Poly(ADP-ribosyl)ation reactions in the regulation of nuclear functions. *Biochem. J.* **342 (Pt 2,** 249–268 (1999).
112. David, K. K., Andrabi, S. A., Dawson, T. M. & Dawson, V. L. Parthanatos, a messenger of death. *Front. Biosci.* **14,** 1116–1128 (2009).
113. Farmer, H. *et al.* Targeting the DNA repair defect in BRCA mutant cells as a therapeutic strategy. *Nature* **434,** 917–921 (2005).
114. Bryant, H. E. *et al.* Specific killing of BRCA2-deficient tumours with inhibitors of poly (ADP-ribose) polymerase. *Nature* **434,** 913–918 (2005).
115. Turner, N., Tutt, A. & Ashworth, A. Hallmarks of 'BRCAness' in sporadic cancers. *Nat. Rev. Cancer* **4,** 1–6 (2004).
116. Ciccia, A. & Elledge, S. J. The DNA Damage Response: Making It Safe to Play with Knives. *Mol. Cell* **40,** 179–204 (2010).
117. Roy, R., Chun, J. & Powell, S. N. BRCA1 and BRCA2 : different roles in a common pathway of genome protection. *Nat. Rev. Cancer* **12,** 68–78 (2012).
118. Kuzminov, A. Single-strand interruptions in replicating chromosomes cause double-strand breaks. *Proc. Natl. Acad. Sci. U. S. A.* **98,** 8241–8246 (2001).
119. Menear, K. a. *et al.* 4-[3-(4-Cyclopropanecarbonylpiperazine-1-carbonyl)-4-fluorobenzyl] -2H-phthalazin-1-one: A novel bioavailable inhibitor of poly(ADP-ribose) polymerase-1. *J. Med. Chem.* **51,** 6581–6591 (2008).
120. Zhu, G., Gong, J., Gandhi, V., Penning, T. & Giranda, V. 1H-Benzimidazole-4-carboxamides substituted with a quaternary carbon at the 2-position are potent PARP inhibitors. (2006).
121. Shen, Y. *et al.* BMN 673, a novel and highly potent PARP1/2 inhibitor for the treatment of human cancers with DNA repair deficiency. *Clin. Cancer Res.* **19,** 5003–15 (2013).
122. Sonnenblick, A., de Azambuja, E., Azim, H. A. & Piccart, M. An update on PARP inhibitors—moving to the adjuvant setting. *Nat. Publ. Gr.* **12,** 27–41 (2014).
123. Ekblad, T., Camaioni, E., Schüler, H. & Macchiarulo, A. PARP inhibitors: Polypharmacology versus selective inhibition. *FEBS J.* **280,** 3563–3575 (2013).
124. Wahlberg, E. *et al.* Family-wide chemical profiling and structural analysis of PARP and tankyrase inhibitors. *Nat. Biotechnol.* **30,** 283–288 (2012).
125. Shen, Y. *et al.* BMN 673, a novel and highly potent PARP1/2 inhibitor for the treatment

of human cancers with DNA repair deficiency. *Clin. Cancer Res.* **19,** 5003–15 (2013).

126. Murai, J. *et al.* Rationale for poly(ADP-ribose) polymerase (PARP) inhibitors in combination therapy with camptothecins or temozolomide based on PARP trapping versus catalytic inhibition. *J. Pharmacol. Exp. Ther.* **349,** 408–16 (2014).
127. Murai, J. *et al.* Stereospecific PARP trapping by BMN 673 and comparison with olaparib and rucaparib. *Mol. Cancer Ther.* **13,** 433–43 (2014).
128. Murai, J. *et al.* Trapping of PARP1 and PARP2 by clinical PARP inhibitors. *Cancer Res.* **72,** 5588–5599 (2012).
129. Audeh, M. W. *et al.* Oral poly(ADP-ribose) polymerase inhibitor olaparib in patients with BRCA1 or BRCA2 mutations and advanced breast cancer: a proof-of-concept trial. *Lancet* **376,** 245–251 (2010).
130. Audeh, M. W. *et al.* Oral poly(ADP-ribose) polymerase inhibitor olaparib in patients with BRCA1 or BRCA2 mutations and recurrent ovarian cancer: a proof-of-concept trial. *Lancet* **376,** 245–251 (2010).
131. Ledermann, J. *et al.* Olaparib Maintenance Therapy in Platinum-Sensitive Relapsed Ovarian Cancer. *N. Engl. J. Med.* **366,** 1382–1392 (2012).
132. Kim, G. *et al.* FDA approval summary: Olaparib monotherapy in patients with deleterious germline BRCA-mutated advanced ovarian cancer treated with three or more lines of chemotherapy. *Clin. Cancer Res.* **21,** 4257–4261 (2015).
133. van Pel, D. M. *et al.* An Evolutionarily Conserved Synthetic Lethal Interaction Network Identifies FEN1 as a Broad-Spectrum Target for Anticancer Therapeutic Development. *PLoS Genet.* **9,** e1003254 (2013).
134. The Cancer Genome Atlas Network. Comprehensive Molecular Characterization of Human Colon and Rectal Cancer. *Nature* **487,** 330–337 (2013).
135. The Cancer Genome Atlas Network. Comprehensive genomic characterization defines human glioblastoma genes and core pathways. *Nature* **455,** 1061–1068 (2008).
136. The Cancer Genome Atlas Network. Integrated Genomic Analyses of Ovarian Carcinoma. *Nature* **474,** 609–615 (2011).
137. The Cancer Genome Atlas Network. Comprehensive genomic characterization of squamous cell lung cancers. *Nature* **489,** 519–525 (2013).
138. Taylor, B. S. *et al.* Integrative genomic profiling of human prostate cancer. *Cancer Cell* **18,** 11–22 (2011).
139. Barretina, J. *et al.* Subtype-specific genomic alterations define new targets for soft tissue sarcoma therapy. *Nat. Genet.* **42,** 715–721 (2011).
140. Cogan, N. *et al.* DNA damaging bystander signalling from stem cells, cancer cells and fibroblasts after Cr(VI) exposure and its dependence on telomerase. *Mutat. Res. - Fundam. Mol. Mech. Mutagen.* **683,** 1–8 (2010).
141. Finlan, L. E. *et al.* Recruitment to the nuclear periphery can alter expression of genes in human cells. *PLoS Genet.* **4,** (2008).
142. Liu, X. & Erikson, R. L. Polo-like kinase (Plk)1 depletion induces apoptosis in cancer cells. *Proc. Natl. Acad. Sci. U. S. A.* **100,** 5789–94 (2003).
143. Spankuch-Schmitt, B., Bereiter-Hahn, J., Kaufmann, M. & Strebhardt, K. Effect of RNA Silencing of Polo-Like Kinase-1 (PLK1) on Apoptosis and Spindle Formation in Human Cancer Cells. *J. Natl. Cancer Inst.* **94,** 1863–1877 (2002).
144. Rogakou, E. P., Pilch, D. R., Orr, A. H., Ivanova, V. S. & Bonner, W. M. DNA Double-stranded Breaks Induce Histone H2AX Phosphorylation on Serine 139. *J. Biol. Chem.*

273, 5858–5868 (1998).

145. Vignard, J., Mirey, G. & Salles, B. Ionizing-radiation induced DNA double-strand breaks: A direct and indirect lighting up. *Radiother. Oncol.* **108,** 362–369 (2013).
146. Zhivotovsky, B., Samali, A., Gahm, A. & Orrenius, S. Caspases: their intracellular localization and translocation during apoptosis. *Cell Death Differ.* **6,** 644–651 (1999).
147. Bertrand, R., Solary, E., O'Connor, P., Kohn, K. W. & Pommier, Y. Induction of a Common Pathway of Apoptosis by Staurosporine. *Exp. Cell Res.* **221,** 314–321 (1994).
148. Saraste, A. & Pulkki, K. Morphologic and biochemical hallmarks of apoptosis. *Cardiovasc. Res.* **45,** 528–537 (2000).
149. Sajesh, B. V & Mcmanus, K. J. Targeting SOD1 induces synthetic lethal killing in BLM- and CHEK2 -deficient colorectal cancer cells. *Oncotarget* (2015).
150. Harrison, R., Papp, B., Pál, C., Oliver, S. G. & Delneri, D. Plasticity of genetic interactions in metabolic networks of yeast. *Proc. Natl. Acad. Sci.* **104,** 2307–2312 (2007).
151. Burrell, R. a, McGranahan, N., Bartek, J. & Swanton, C. The causes and consequences of genetic heterogeneity in cancer evolution. *Nature* **501,** 338–45 (2013).
152. Vilar, E. *et al.* Microsatellite instability due to hMLH1 deficiency is associated with increased cytotoxicity to irinotecan in human colorectal cancer cell lines. *Br. J. Cancer* **99,** 1607–1612 (2008).
153. Bajrami, I. *et al.* Genome-wide profiling of genetic synthetic lethality identifies CDK12 as a novel determinant of PARP1/2 inhibitor sensitivity. *Cancer Res.* **74,** 287–297 (2014).
154. McCabe, N. *et al.* Deficiency in the repair of DNA damage by homologous recombination and sensitivity to poly(ADP-ribose) polymerase inhibition. *Cancer Res.* **66,** 8109–8115 (2006).
155. Min, A. *et al.* RAD51C-deficient cancer cells are highly sensitive to the PARP inhibitor olaparib. *Mol. Cancer Ther.* **12,** 865–77 (2013).
156. Loveday, C. *et al.* Germline mutations in RAD51D confer susceptibility to ovarian cancer. *Nat. Genet.* **43,** 879–882 (2011).
157. Koppensteiner, R. *et al.* Effect of MRE11 loss on PARP-inhibitor sensitivity in endometrial cancer in vitro. *PLoS One* **9,** e100041 (2014).
158. Turner, N. C. *et al.* A synthetic lethal siRNA screen identifying genes mediating sensitivity to a PARP inhibitor. *EMBO J.* **27,** 1368–1377 (2008).
159. Lord, C. J., McDonald, S., Swift, S., Turner, N. C. & Ashworth, A. A high-throughput RNA interference screen for DNA repair determinants of PARP inhibitor sensitivity. *DNA Repair (Amst).* **7,** 2010–2019 (2008).
160. Guo, J., Liu, H. & Zheng, J. SynLethDB: synthetic lethality database toward discovery of selective and sensitive anticancer drug targets. *Nucleic Acids Res.* **44,** D1011–1017 (2015).
161. Oza, A. M. *et al.* Olaparib combined with chemotherapy for recurrent platinum-sensitive ovarian cancer: A randomised phase 2 trial. *Lancet Oncol.* **16,** 87–97 (2015).
162. J. Mateo, S. Carreira, S. Sandhu, S. Miranda, H. Mossop, R. Perez-Lopez, D. Nava Rodrigues, D. Robinson, A. Omlin, N. Tunariu, G. Boysen, N. Porta, P. Flohr, A. Gillman, I. Figueiredo, C. Paulding, G. Seed, S. Jain, C. Ralph, A. Protheroe, S. Hussain, R., Z. Z. & C.T. Williamson, R. Ferraldeschi, R. Riisnaes, B. Ebbs, G. Fowler, D. Roda, W. Yuan, Y.-M. Wu, X. Cao, R. Brough, H. Pemberton, R. A'Hern, A. Swain, L.P. Kunju, R. Eeles, G. Attard, C.J. Lord, A. Ashworth, M.A. Rubin, K.E. Knudsen, F.Y. Feng, A.M. Chinnai, and J. S. de B. DNA-Repair Defects and Olaparib in Metastatic

Prostate Cancer. *N. Engl. J. Med.* **368,** 2255–2265 (2015).

163. Shah, G. M. *et al.* PARP Inhibitors in Cancer Therapy: Magic Bullets but Moving Targets. *Front. Oncol.* **3,** 279 (2013).
164. Kauppinen, T. M. Multiple roles for poly(ADP-ribose)polymerase-1 in neurological disease. *Neurochem. Int.* **50,** 954–958 (2007).
165. Vuong, B. *et al.* NF-κB transcriptional activation by TNFα requires phospholipase C, extracellular signal-regulated kinase 2 and poly(ADP-ribose) polymerase-1. *J. Neuroinflammation* **12,** 229 (2015).
166. Swindall, A. F., Stanley, J. a & Yang, E. S. PARP-1: Friend or Foe of DNA Damage and Repair in Tumorigenesis? *Cancers (Basel).* **5,** 943–58 (2013).
167. Wilczewska, A., Niemirowicz, K., Markiewicz, K. & Car, H. Nanoparticles as drug delivery systems. *Pharmacol. Reports* **64,** pp. 1864–1882. (2012).
168. Holohan, C., Van Schaeybroeck, S., Longley, D. B. & Johnston, P. G. Cancer drug resistance: an evolving paradigm. *Nat. Rev. Cancer* **13,** 714–26 (2013).
169. Edwards, S. L. *et al.* Resistance to therapy caused by intragenic deletion in BRCA2. *Nature* **451,** 1111–1115 (2008).
170. Jia, J. *et al.* Mechanisms of drug combinations: interaction and network perspectives. *Nat. Rev. Drug Discov.* **8,** 111–128 (2009).
171. Somwar, R. *et al.* Superoxide dismutase 1 (SOD1) is a target for a small molecule identified in a screen for inhibitors of the growth of lung adenocarcinoma cell lines. *Proc. Natl. Acad. Sci. U. S. A.* **108,** 16375–80 (2011).
172. Srivastava, M. *et al.* An inhibitor of nonhomologous end-joining abrogates double-strand break repair and impedes cancer progression. *Cell* **151,** 1474–1487 (2012).
173. Housman, G. *et al.* Drug resistance in cancer: an overview. *Cancers (Basel).* **6,** 1769–1792 (2014).
174. Deakyne, J. S. *et al.* Analysis of the activities of RAD54, a SWI2/SNF2 protein, using a specific small-molecule inhibitor. *J. Biol. Chem.* **288,** 31567–31580 (2013).
175. Yasuhara, T., Suzuki, T., Katsura, M. & Miyagawa, K. Rad54B serves as a scaffold in the DNA damage response that limits checkpoint strength. *Nat. Commun.* **5,** 5426 (2014).
176. Farnebo, M., Bykov, V. J. N. & Wiman, K. G. The p53 tumor suppressor: A master regulator of diverse cellular processes and therapeutic target in cancer. *Biochem. Biophys. Res. Commun.* **396,** 85–89 (2010).

APPENDIX A: LIST OF SOLUTIONS

CELL CULUTRE

10× PBS (Stock Solution)

Name	Amount
NaCl	80.0 g
KCl	2.0 g
Na_2HPO_4	14.4 g
KH_2PO_4	2.4 g
ddH_2O	800 mL
Titrate	
ddH_2O	up to 1.0 L total volume
Total Volume	1.0 L

-titrate to pH 7.4

1× PBS

Name	Amount
10x PBS (Stock)	100.0 mL
ddH_2O	900.0 mL
Total Volume	1.0 L

WESTERN BLOT

RIPA Buffer

Name	Amount
Tris 50mM (pH 8.0)	5.0 mL
NaCl 150 mM	7.5 mL
SDS 0.1%	500 µL
Sodium Deoxycholate 0.5%	0.5 g
NP40 1%	1 mL
Milli-Q water	Up to 100.0 mL total volume
Total Volume	100.0 mL

-store at 4°C protected from light

Protease Inhibitor

Name	Amount
25x Protease Inhibitor cOmplete EDTA-free (Roche)	1 capsule
Milli-Q water	2.0 mL
Total Volume	2.0 mL

-vortex till dissolved, store at -20°C

Lysis Buffer

Name	Amount
RIPA Buffer	955.0 µL
Protease Inhibitor	45.0 µL
Total Volume	1.0 L

5× SDS/DTT Sample Buffer

Name	Amount
Glycerol	12.0 mL
Dithiothreitol	1.54 g
SDS	2.0 g
2M Tris-HCl – pH 6.8	2.5 mL
Bromophenol Blue	Until desired colour is reached
Milli-Q water	Up to 20.0 mL total volume
Total Volume	20.0 mL

10× Running Buffer

Name	Amount
Tris Base	30.0 g
Glycine	144.0 g
SDS	10.0 g
Milli-Q water	up to 1.0 L total volume
Total Volume	1.0 L

1× Running Buffer

Name	Amount
10x Running Buffer	100.0 mL
Milli-Q water	900.0 mL
Total Volume	1.0 L

Transfer Buffer

Name	Amount
10x Running Buffer	100.0 mL
Methanol	200.0 mL
Milli-Q water	700.0 mL
Total Volume	1.0 L

10× Tris Buffered Saline (TBS)

Name	Amount
NaCl	80.0 g
KCl	2.0 g
1 M Tris pH 7.5	250.0 mL
Milli-Q water	Up to 1.0 L total volume
Total Volume	1.0 L

TBS-Tween20 (TBST)

Name	Amount
10× TBS	100.0 mL
Tween-20	1.0 mL
Milli-Q water	900.0 mL
Total Volume	1.0 L

5% Skim Milk (w/v)

Name	Amount
Skim milk	5.0 g
1× TBST	100.0 mL
Total Volume	100.0 mL

Copper phthalocyanine 3, 4’, 4’’, 4’’’-tetrasulfonic acid tetrasodium salt (CPTS)

Name	Amount
CPTS	100.0 mL
HCl (concentrated)	1.0 mL
Milli-Q water	1.0 mL
Total Volume	1.0 L

INDIRECT IMMUNOFLUORESCENCE

4% Paraformaldehyde (w/v)

Name	Amount
Paraformaldehyde (supplier)	0.4 g
1× PBS	up to 10.0 mL total volume
Total Volume	10.0 mL

-bring to boil with mixing
-allow to cool prior to use

PBS 0.5% Triton X-100(v/v)

Name	Amount
Triton X-100	5.0 mL
1× PBS	995.0 mL
Total Volume	1.0 L

PBS 0.1% Triton X-100(v/v)

Name	Amount
Triton X-100	1.0 mL
1× PBS	999.0 mL
Total Volume	1.0 L

4’,6-Diamidino-2-phenylindole (DAPI) 50 µg/mL

Name	Amount
DAPI 5 mg/mL (Sigma-Aldrich)	10.0 µL
1× PBS	10.0 µL
Total Volume	20.0 µL

-store at 4°C protected from light

DAPI in Mounting Media

Name	Amount
DAPI (50 µg/mL)	10.0 µL
Vecta Shield Mounting Media (Vector Laboratories)	1.0 mL
Total Volume	110.0 mL

-vortex well
-store at 4°C protected from light

APPENDIX B: SUPPLEMENTARY TABLES

Table S1: *In silico* Analyses Predict Functional Consequences of Amino Acid Substitutions in RAD54B

Amino Acid substitution	Cancer Type	Mutation Assessor[74]	PolyPhen2[76]	SIFT[76]
F20C[58]	Uterine	Low	Probably Damaging	Not tolerated
E33D[59]	Colorectal	Neutral	Benign	Not tolerated
E75*[58]	Uterine			
S104L[62]	Breast	Low	Benign	Not tolerated
S104L[58]	Uterine	Low	Benign	Not tolerated
K157N[58]	Uterine	Medium	Probably Damaging	Tolerated
G213E[64]	Lung	Low	Benign	Not tolerated
K233N[63]	Stomach	Low	Probably Damaging	Not tolerated
R297Q[58]	Uterine	Medium	Probably Damaging	Not tolerated
G303E[67]	Lung	High	Probably Damaging	Not tolerated
G351D[71]	Glioblastoma	Medium	Probably Damaging	Tolerated
W370*[67]	Lung			
E373*[65]	Colorectal			
R415H[65]	Colorectal	Medium	Probably damaging	Tolerated
D418Y[41]	Colorectal	Medium	Probably damaging	Not tolerated
E432*[65]	Colorectal			
R435H[58]	Uterine	Medium	Probably Damaging	Not tolerated
E469*[58]	Uterine			
E469D[65]	Colorectal	Medium	Probably Damaging	Not tolerated
E469Q[67]	Lung	High	Probably Damaging	Not tolerated
R530I[58]	Uterine	High	Probably Damaging	Not tolerated
R573*[69]	Bladder			
G574W[67]	Lung	High	Probably Damaging	Not tolerated
I585L[71]	Glioblastoma	Low	Probably Damaging	Not tolerated
N593S[41]	Lymphoma	Medium	Probably Damaging	Tolerated
L634F[57]	Melanoma	Neutral	Benign	Not tolerated
E656K[65]	Colorectal	Neutral	Possibly Damaging	Tolerated
R658*[72]	Breast			
R658Q[69]	Bladder	Neutral	Possibly Damaging	Tolerated
Q671*[58]	Uterine			
K681T[58]	Uterine	Low	Benign	Not tolerated
D691N[66]	Bladder	Medium	Probably Damaging	Not tolerated
S720*[66]	Bladder			
G726V[62]	Breast	High	Probably Damaging	Not tolerated
Y738C[65]	Colorectal	Medium	Probably damaging	Not tolerated
D739A[67]	Lung	High	Probably Damaging	Not tolerated
R756I[58]	Uterine	High	Probably Damaging	Not tolerated

I778M[70]	Esophagus	Medium	Probably Damaging	Not tolerated
G787C[67]	Lung	Medium	Probably Damaging	Not tolerated
L788V[70]	Esophagus	Medium	Probably Damaging	Not tolerated
K810T[58]	Uterine	Medium	Probably Damaging	Not tolerated
S841*[62,72]	Breast			
L884V[64]	Lung	Low	Benign	Not tolerated
T904A[63]	Stomach	Low	Probably Damaging	Not tolerated

* Nonsense mutation

Table S2: Student's *t*-tests Identifying Statistical Differences in Relative Percentage of Cells Remaining Following PARP1 Silencing Between *RAD54B*-proficieint and *RAD54B*-deficient Cells

		Mean cell number ± SD[B]		**Mean normalized relative percentage[C]**		
siRNA treatment	**n[A]**	***RAD54B*-proficient**	***RAD54B*-deficient**	***RAD54B*-proficient**	***RAD54B*-deficient**	***p*-value**
si*GAPDH*	6	14903 ± 303.1	15870 ± 332.7	100 ± 2.034	100 ± 2.097	> 0.9999
si*PARP1*-P	6	14355 ± 296.9	14571 ± 523.0	96.32 ± 1.992	91.81 ± 3.296	0.0167
si*PARP1*-1	6	13568 ± 267.4	13884 ± 363.8	91.04 ± 1.794	87.48 ± 2.292	0.0135
si*PARP1*-2	6	14504 ± 551.7	14462 ± 335.6	97.32 ± 3.702	91.13 ± 2.114	0.0052
si*PLK1*	6	1074 ± 405.8	925 ± 579.9	7.206 ± 2.723	5.831 ± 3.654	0.4766

[A] n; number of wells analyzed
[B] SD; standard deviation
[C] All values are normalized to si*GAPDH* control for respective cell line

Table S3: Dual siRNA-based Synthetic Lethal Testing in HCT116 Cells

siRNA treatment	**n**^{A}	**Mean cell number ± SD**^{B}	**Normalized relative percentage**^{C}	**Expected percentage**^{D}	**Percent difference**^{E}
si*GAPDH*	6	15356 ± 721.4	100 ± 4.698	N/A	N/A
si*RAD54B*	6	14130 ± 914.3	92.02 ± 5.955	N/A	N/A
si*PARP1*-P	6	13006 ± 967.0	84.70 ± 6.297	N/A	N/A
si*PARP1*-1	6	12791 ± 746.7	83.30 ± 4.863	N/A	N/A
si*PARP1*-2	6	12693 ± 354.1	82.66 ± 2.306	N/A	N/A
si*RAD54B* + si*PARP1*-P	6	8908 ± 1120	58.01 ± 7.293	77.938	26
si*RAD54B* + si*PARP1*-1	6	9515 ± 892.2	61.97 ± 5.811	76.654	19
si*RAD54B* + si*PARP1*-2	5	10220 ± 1440	66.56 ± 9.377	76.067	18
si*PLK1*	6	859 ± 45.11	5.596 ± 0.2938	N/A	N/A

[A] n; number of wells analyzed
[B] SD; standard deviation
[C] All values are normalized to si*GAPDH* control for respective cell line
[D] Calculated by multiplying the normalized percentage of the two individual siRNAs
[E] Calculated as 1 – (Normalized relative percentage/expected percentage) × 100 (N/A; not applicable)

Table S4: Student's *t*-tests Reveal Statistical Differences of Relative Percentage of Cells Remaining Following BMN673 Treatment within *RAD54B*-deficient Cells Compared to Controls

		Mean cell number ± SD[B]		**Mean normalized relative percentage**[C] **± SD**		
Drug Treatment	**n**[A]	***RAD54B*-proficient**	***RAD54B*-deficient**	***RAD54B*-proficient**	***RAD54B*-deficient**	***p*-value**
DMSO	6	12791 ± 759.5	11743 ± 859.9	100 ± 5.938	100 ± 7.322	> 0.9999
2 nM BMN673	6	12509 ± 409.1	10306 ± 601.5	97.79 ± 3.198	87.76 ± 5.122	0.0022
20 nM BMN672	6	6911 ± 701.1	4933 ± 230.5	54.03 ± 5.481	42.01 ± 1.963	0.0005

[A] n; number of wells analyzed
[B] SD; standard deviation
[C] All values are normalized to vehicle control (DMSO) for respective cell line

Table S5: Student's *t*-tests Identify Statistical Differences of Relative Percentage of Cells Remaining Following Olaparib Treatment within *RAD54B*-deficient Cells Compared to Controls

		Mean cell number ± SD[B]		**Mean normalized relative percentage[C] ± SD**		
Drug Treatment	**n[A]**	***RAD54B*-proficient**	***RAD54B*-deficient**	***RAD54B*-proficient**	***RAD54B*-deficient**	***p*-value**
DMSO	6	14567± 506.5	15330 ± 525.4	100 ± 3.477	100 ± 3.427	> 0.9999
0.2 μM Olaparib	6	13032 ± 373.8	12982 ± 506.5	89.46 ± 2.566	84.68 ± 3.304	0.0386
2.0 μM Olaparib	6	10202 ± 386.8	9293 ± 449.4	70.03 ± 2.655	60.62 ± 2.931	0.0016

[A] n; number of wells analyzed

[B] SD; standard deviation

[C] All values are normalized to vehicle control (DMSO) for respective cell line

Table S6: Proliferation Defect (PD[A]) Values Calculated from RTCA Growth Curves

Inhibitor	***RAD54B*-proficient PD**	***RAD54B*-deficient PD**	**Fold Increase[B]**
BMN673	0.55	51.80	94.18
Olaparib	1.71	17.83	10.43

[A]PD; Proliferation defect as calculated by

$$\text{PD} = \left\{ 1\text{-} \left(\frac{\text{Cell Index}_{\text{Drug}}}{\text{Cell Index}_{\text{DMSO}}} \right) \right\} \times 100$$

[B]Fold increase; *RAD54B*-deficient PD/*RAD54B*-proficient PD

Table S7: Student's *t*-tests Reveal Statistical Differences of Relative Percentage of Cell Confluency Following BMN673 Treatment within *RAD54B*-deficient Cells Compared to Controls in Modified 2D Colony Forming Assays

		Mean normalized relative percentage[B] ± SD[C]		
Drug Treatment	n[A]	*RAD54B*-proficient	*RAD54B*-deficient	*p*-value
DMSO	6	100 ± 5.47	100 ± 5.81	> 0.9999
BMN673	6	36.76 ± 10.91	19.48 ± 2.09	0.0034

[A] n; number of wells analyzed
[B] All values are normalized to vehicle control (DMSO) for respective cell line
[C] SD; standard deviation

Table S8: Student's *t*-tests Identify Statistical Differences of Relative Percentage of Cell Confluency Following Olaparib Treatment within *RAD54B*-deficient Cells Compared to Controls in Modified 2D Colony Forming Assays

		Mean normalized relative percentage[B] ± SD[C]		
Drug Treatment	n[A]	*RAD54B*-proficient	*RAD54B*-deficient	*p*-value
DMSO	6	100 ± 2.28	100 ± 3.95	> 0.9999
Olaparib	6	42.86 ± 15.04	15.73 ± 4.89	0.0018

[A] n; number of wells analyzed

[B] All values are normalized to vehicle control (DMSO) for respective cell line

[C] SD; standard deviation

Table S9: Student's *t*-tests Identifying Statistical Differences of Total γ-H2AX Signal Intensity Following BMN673 and Olaparib Treatment

		Mean total γ-H2AX signal intensity ± SD[B] ($\times10^6$ A.U.)		
Treatment	**n[A]**	***RAD54B*-proficient**	***RAD54B*-deficient**	***p*-value**
IR	175	15.8 ±7.05	15.6 ± 7.59	0.8202
DMSO	175	6.23 ± 3.06	5.83 ± 2.7	0.1928
BMN673	175	7.52 ± 4.94	9.19 ± 6.23	0.0058
Olaparib	175	7.99 ± 4.40	10.6 ± 6.88	<0.0001

[A] n; number of cells evaluated
[B] SD; standard deviation

Table S10: Student's *t*-tests Identifying Statistical Differences of Percent of Cells with Activated Cleaved Caspase-3 Signal within *RAD54B*-deficient Cells Following BMN673 and Olaparib Treatment

		Percentage of cells with activated cleaved Caspase-3 ± SD[B]		
Drug Treatment	N[A]	*RAD54B*-proficient	*RAD54B*-deficient	*p*-value
Staurosporine	2	2.66 ± 0.28	2.35 ± 0.19	0.3285
DMSO	2	0.05 ± 0.07	0.04 ± 0.05	0.8531
BMN673	2	0.50 ± 0.01	0.69 ± 0.03	0.0132
Olaparib	2	0.23 ± 0.08	0.70 ± 0.01	0.0125

[A] N; number of experimental replicates

[B] SD; standard deviation

Table S11: Dual siRNA-based Synthetic Lethal Testing in hTERT Cells

siRNA treatment	n[A]	Mean cell number ± SD[B]	Normalized relative percentage[C]	Expected percentage[D]	Percent difference[E]
si*GAPDH*	6	5531 ± 343.7	100 ± 6.214	N/A	N/A
si*RAD54B*	6	5322 ± 299.6	96.21 ± 5.416	N/A	N/A
si*PARP1*-P	6	5829 ± 143.2	105.4 ± 2.589	N/A	N/A
si*PARP1*-1	6	5146 ± 220.8	93.04 ± 3.993	N/A	N/A
si*PARP1*-2	6	5227 ± 190.0	94.50 ± 3.434	N/A	N/A
si*RAD54B* + si*PARP1*-P	6	4936 ± 174.1	98.18 ± 2.372	101.4	3.176
si*RAD54B* + si*PARP1*-1	6	5431± 131.2	89.23 ± 3.148	88.55	-0.768
si*RAD54B* + si*PARP1*-2	6	4996 ± 134.1	90.32 ± 2.424	90.91	0.649
si*PLK1*	6	1959 ± 178.6	35.42 ± 3.229	N/A	N/A

[A] n; number of wells analyzed
[B] SD; standard deviation
[C] All values are normalized to si*GAPDH* control for respective cell line
[D] Calculated by multiplying the normalized percentage of the two individual siRNAs
[E] Calculated as 1 – (Normalized relative percentage/expected percentage) × 100 (N/A; not applicable)